TU Wien

Dissertation

Oxygen exchange kinetics of mixed conducting oxides and its relation to defect chemistry

Author:
Dipl. Ing. Alexander Schmid

Supervisor:
Univ.-Prof. Dipl.-Phys. Dr.
Jürgen Fleig

A thesis submitted in fulfilment of the requirements for the degree of PhD at the

Institute of Chemical Technologies and Analytics

Alexander Schmid

01 2020, Vienna

Hanauskagasse 2/4/2, 1120 Wien

Abstract

Solid oxide fuel cells (SOFCs) and solid oxide electrolysis cells (SOECs) are promising devices for energy conversion, due to their high efficiency and power density as well as fuel flexibility. The limiting factor for the performance of SOFCs is often the oxygen reduction at the cathode, and current research aims at finding materials that exhibit sufficiently fast oxygen reduction kinetics even at intermediate temperatures (400 to 600 °C) while also exhibiting long term stability. Mixed ionic and electronic conducting (MIEC) perovskite-type oxides are among the most promising candidates for high performance electrode materials in SOFCs and SOECs. Various compositions, for example $La_xSr_{1-x}Co_yFe_{1-y}O_{3-\delta}$ (LSCF), $Ba_xSr_{1-x}Co_yFe_{1-y}O_{3-\delta}$ (BSCF) and $La_xSr_{1-x}Ti_yFe_{1-y}O_{3-\delta}$ (LSTF) are investigated. Understanding the oxygen reduction mechanism on such materials may give valuable insights into the limiting factors for oxygen reduction and thus aids in the search for catalytically highly active materials for oxygen reduction electrodes.

In this study the oxygen exchange kinetics on mixed conducting perovskite electrode surfaces is investigated, and the role of perovskite point defects for the oxygen exchange reaction is elucidated. $La_{0.6}Sr_{0.4}FeO_{3-\delta}$ (LSF) thin film electrodes are chosen as model system, as they offer well defined surface morphology and area as well as reduced complexity, e.g. by eliminating gas diffusion into pores. Electrochemical impedance spectroscopy and DC-measurements on three-electrode configuration samples allow isolating the impedance response of a single electrode, and this gives access to the kinetic (i.e. oxygen exchange reaction rates) and thermodynamic (i.e. defect concentrations) properties of this electrode.

First, electrochemical impedance spectroscopy with varying DC polarization and oxygen partial pressure is employed to investigate the defect chemistry of LSF thin films over a wide range of oxygen chemical potentials. Analysis of the chemical capacitance reveals an equivalency of p_{O_2} and electrode polarization with regards to their effects on defect concentrations. Defect concentrations depend solely on the oxygen chemical potential, regardless of it being driven by p_{O_2} or by an overpotential. Fitting a defect model to those chemical capacitance data yielded thermodynamic parameters, i.e. enthalpies and entropies of the LSF defect equilibria. Data on macroscopic samples and thin films agree very well for the oxygen exchange reaction, however, higher concentration of electronic charge carriers were found in thin films.

In a second step, DC current-voltage measurements are used to obtain the oxygen exchange kinetics as a function of p_{O_2} and electrode polarization and the resulting oxygen chemical potential. A novel approach of analysing such current-voltage data is presented, which allows separating phenomenologically observed dependencies into reaction orders of defects and adsorbates. By counterbalancing p_{O_2} induced defect concentration changes through applied voltages it is possible to isolate the direct effect of p_{O_2} due to adsorbates from its indirect effect via defect concentration changes. Likewise, variation of defect concentrations by the voltage at constant p_{O_2} reveals the direct effect of defect concentrations. This experimental approach is demonstrated for LSF thin film electrodes.

Third, a broadly applicable model is derived, that describes the oxygen exchange kinetics as a result of defect concentrations and their relation to p_{O_2} and electrode polarization. Based on two exemplary reaction mechanisms and a known defect chemical data set of LSF, current voltage curves are simulated for a wide range of parameters. These curves reveal a variety of features such as exponential Tafel like curves as well as essentially flat current limited regimes. However, it is shown that despite curve shapes often resembling those of classical aqueous electrochemistry, the physical reasons are quite different, i.e. they lie in the relationship between defect concentrations and p_{O_2} or overpotential. General expressions for p_{O_2} and overpotential dependencies are derived and these demonstrate that an empirical analysis of observed dependencies with established models may often lead to erroneous conclusions.

Finally, in-situ impedance spectroscopy inside the pulsed laser deposition chamber was utilized to study the resistance of pristine LSF films and its degradation behaviour. Freshly deposited LSF films were found to have extremely low polarization resistance compared to ex-situ measured samples, even in very low oxygen atmospheres. Controlled exposure to potentially degrading environments revealed this low resistive state to be surprisingly robust. Time dependent measurements suggest a second fast degradation mechanism upon transfer to ex-situ setups, in addition to the known slower degradation due to Sr segregation. Correlation with surface chemistry analysis by X-ray photoelectron spectroscopy gave evidence that this fast degradation is caused by minute traces of sulphur, and the formation of $SrSO_4$ on the LSF surface.

Kurzfassung

Festoxid-Brennstoff- und -Elektrolysezellen sind vielversprechende Technologien für elektrochemische Energieumwandlung und zeichnen sich durch hohe Effizienz und Energiedichte sowie durch flexible Treibstoffanforderungen aus. Der limitierende Faktor für den Betrieb von Brennstoffzellen ist oftmals die Sauerstoffreduktion an der Kathode. Gegenwärtig wird an Materialien mit genügend hoher katalytischer Aktivität für die Sauerstoffreduktion bei moderaten Temperaturen (400 bis 600 °C) gesucht, welche zudem über eine ausreichende Langzeitstabilität verfügen. Gemischt-ionisch-elektronisch leitende Oxide vom Perowskit-Typ gehören zu den vielversprechendsten Hochleistungsmaterialien für Brennstoffzellenelektroden. Eine Vielzahl solcher Materialien verschiedener Zusammensetzung wie etwa $La_xSr_{1-x}Co_yFe_{1-y}O_{3-\delta}$ (LSCF), $Ba_xSr_{1-x}Co_yFe_{1-y}O_{3-\delta}$ (BSCF) und $La_xSr_{1-x}Ti_yFe_{1-y}O_{3-\delta}$ (LSTF) wird untersucht. Ein mechanistisches Verständnis der Sauerstoffreduktion an solchen Materialien könnte wertvolle Hinweise auf die limitierenden Faktoren der entsprechenden Elektroden geben und damit die Suche nach katalytisch hochaktiven Materialien unterstützen.

Ziel dieser Arbeit ist es, die Kinetik der Sauerstoffreduktion an gemischt leitenden Perowskitelektroden zu untersuchen und die Rolle von Punktdefekten im Perowskit bei dieser Reaktion näher zu beleuchten. $La_{0.6}Sr_{0.4}FeO_{3-\delta}$ (LSF) Dünnfilmelektroden dienen dabei als Modellsystem, da sie über eine wohldefinierten Oberfläche und Morphologie verfügen und zudem die Komplexität gegenüber realen Elektroden reduzieren, etwa durch Umgehung von Gasdiffusion in Poren. Elektrochemische Impedanzspektroskopie und DC-Messungen von 3-Elektroden-Zellen erlauben es, die Impedanz einer einzelnen Elektrode zu isolieren, und damit die kinetischen (Sauerstoffaustauschrate) und thermodynamischen (Defektkonzentration) Daten dieser Elektrode zu bestimmen.

Zunächst wurde mittels elektrochemischer Impedanzspektroskopie bei variierenden DC-Spannungen und Sauerstoffpartialdrücken die Defektchemie von LSF Dünnfilmen über einen weiten Bereich des chemischen Sauerstoffpotentials bestimmt. Eine Analyse der chemischen Kapazität zeigt die Äquivalenz von Sauerstoffpartialdruck und Elektrodenpolarisation hinsichtlich deren Wirkung auf Defektkonzentrationen. Diese hängen nur vom chemischen Sauerstoffpotential ab, unabhängig davon ob dieses durch p_{O_2} oder durch Überspannung bestimmt wird. Durch Anpassung eines Defektmodells für LSF an die gemessenen chemischen Kapazitäten

können thermodynamische Parameter (i.e. Enthalpien und Entropien) der LSF Defektgleichgewichte gewonnen werden. Diese zeigen gute Übereinstimmung mit Daten makroskopischer LSF Proben hinsichtlich der Sauerstoffaustauschreaktion, jedoch zeigt sich eine höhere Konzentration elektronischer Ladungsträger im Dünnfilm.

In einem zweiten Schritt wurden DC Strom-Spannungsmessungen genutzt, um die Sauerstoffaustauschkinetik und deren Abhängigkeit von Elektrodenüberspannung, Sauerstoffpartialdruck und dem daraus resultierenden chemischen Sauerstoffpotential zu bestimmen. Eine neue Methode zur Analyse solcher Strom-Spannungskennlinien, die es erlaubt die experimentell beobachteten, phänomenologischen Abhängigkeiten in Reaktionsordnungen von Defekten und Adsorbaten zu zerlegen wird vorgestellt. Durch Anlegen einer Spannung, welche die p_{O_2}-verursachten Defektkonzentrationsänderungen exakt kompensiert, ist es möglich, den direkten Effekt des p_{O_2} durch Adsorbate von dessen indirektem Effekt durch Defektkonzentrationsänderungen zu trennen. Gleichermaßen lässt sich durch Änderung von Defektkonzentrationen mittels Anlegen von Spannung bei konstantem p_{O_2} der Einfluss der Defektkonzentrationen bestimmen. Dieser experimentelle Ansatz wird anhand von LSF Dünnfilmen demonstriert.

Drittens wird ein allgemeines mechanistisches Modell entwickelt, dass den Zusammenhang der Sauerstoffaustauschkinetik mit den Defektkonzentrationen und deren Abhängigkeit von p_{O_2} und Überspannung beschreibt. Basierend auf den bekannten defektchemischen Daten von LSF werden Strom-Spannungskennlinien für zwei exemplarische Mechanismen über einen weiten p_{O_2}-Bereich simuliert. Diese zeigen eine Vielfalt an Kurvenformen, etwa exponentielle Tafel-artige als auch stromlimitierte Zusammenhänge. Obwohl diese oftmals ähnlich zu Kurven aus klassischen flüssig-elektrochemischen Modellen erscheinen, liegen ihnen andere physikalische Ursachen zugrunde, namentlich das Zusammenspiel zwischen Defektkonzentrationen und p_{O_2} oder Überspannung. Allgemeine Beschreibungen der p_{O_2}- und Überspannungsabhängigkeiten werden formuliert, und diese zeigen dass eine empirische Analyse anhand etablierter Modelle oftmals zu falschen Ergebnissen führen kann.

Schließlich wurde die Sauerstoffaustauschkinetik dünner LSF Schichten in ihrem ursprünglichen Zustand sowie deren Degradation mittels in-situ Impedanzspektroskopie in der Abscheidekammer untersucht. Frisch abgeschiedene Dünnfilme zeigten dabei deutlich niedrigere Widerstände verglichen mit ex-situ Messungen. Kontrollierte Einwirkung von potentiell degradationsverursachenden Bedingungen zeigte eine erstaunliche Robustheit dieses hochaktiven Zustands. Zeitabhängige Messungen wiesen auf einen zweiten, schnellen Degradationsmechanismus während des Transfers in ex-situ Messaufbauten hin, zusätzlich zur bekannten langsameren Degradation durch Sr-Segregation. In Zusammenhang mit einer Oberflächenanaly-

se durch Röntgen-Photoelektronenspektroskopie zeigte sich, dass diese schnelle Degradation durch Spuren von Schwefel und die damit verbundene Bildung von $SrSO_4$ an der LSF Oberfläche verursacht wird.

Contents

1 Motivation and theoretical background

1.1 Motivation

Developing sustainable, CO_2 neutral power production is one of the most severe and arguably the most urgent technological challenge of the 21st century. Drastic reduction and ultimately complete cessation of carbon dioxide emission is necessary to reduce climate change and limit the increase in global average temperature to "well below 2 °C". To achieve the transition from a mainly fossil fuel based economy to a CO_2 free, sustainable one, a combination of improved energy conversion efficiency and higher share of renewable energy sources is required.

Many renewable energy sources suffer from an inability to match supply and demand, as their energy output depends on the availability of environmental energy sources e.g. wind or solar radiation. Efficient storage and conversion of electrical energy is thus required to make renewable energy sources a feasible alternative to fossil fuels.

Solid oxide fuel cells (SOFCs) offer highly efficient direct conversion of chemical to electrical energy. Unlike fossil fuel fired power plants SOFCs do not employ heat engine cycles and thus are not limited by the Carnot efficiency. The waste heat of the electrochemical reaction can be utilized in combined power and heating (CPH) systems, further increasing the total efficiency. Moreover, SOFCs offer high fuel flexibility allowing usage of hydrogen, hydrocarbons or methanol as fuel. Other advantages include excellent scalability, little to no moving parts, noiseless operation and the ability to quickly adapt their power output. These factors make SOFCs an attractive solution for a wide range of applications such as decentralized electricity and heat production, power sources for electrical vehicles or auxiliary power units (APU) in conventional combustion engine vehicles.

Operated in reverse direction as solid oxide electrolysis cells (SOECs) they enable efficient conversion of electrical energy to chemical energy by splitting water into H_2 and O_2. Excess electrical energy from regenerative sources can thus be utilized for CO_2 neutral hydrogen production. Combined utilisation of SOFCs and SOECs allows for efficient energy storage by using electric energy during low demand times to electrolyse water in an SOEC and convert the produced hydrogen back to electrical energy by an SOFC at peak hours.

1.2 Working principle

Solid oxide fuel cells are composed of of three essential parts, namely anode, cathode and electrolyte, as depicted in figure 1.1a for the case of mixed conducting electrodes. The cathode

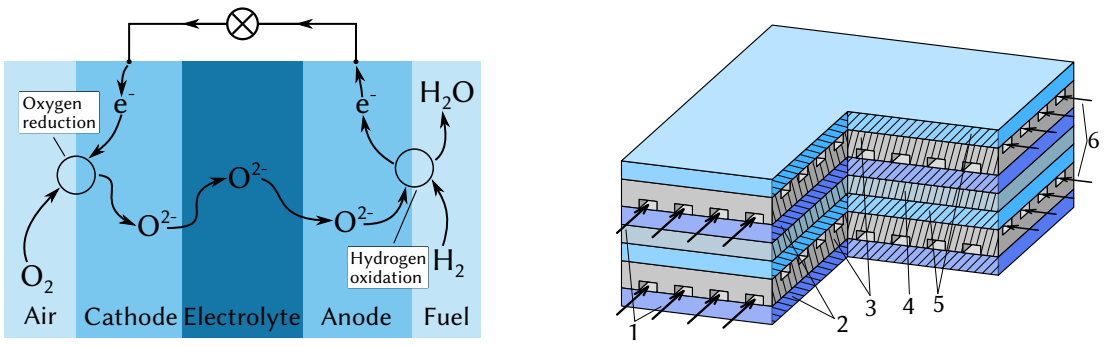

(a) SOFC working principle

(b) SOFC stack

Figure 1.1: (a) Working principle of an SOFC. (b) Schematic of an SOFC stack consisting of: fuel feed (1), anode (2), interconnect (3), electrolyte (4), cathode (5) and air feed (6).

is continuously supplied with an oxidizer (air, O_2) which gets reduced and incorporated into the solid electrode:

$$O_2 + 4\,e^- \longrightarrow 2\,O^{2-}. \tag{1.1}$$

At the anode fuel is oxidized and together with oxide ions from the anode water (and CO_2 when using hydrocarbon fuels) is formed:

$$2\,H_2 + 2\,O^{2-} \longrightarrow 2\,H_2O + 4\,e^-. \tag{1.2}$$

Anode and cathode are separated by an oxide ion conducting electronically insulating electrolyte. Due to the spatial separation of the two electrodes an oxygen chemical potential gradient is formed across the electrolyte and this acts as driving force for cell operation.

For practical applications several such cells are connected in series as a single cell produces less than 1 V. The individual cells are connected by interconnects which have to fulfil several requirements such as good electronic conductivity, ionic insulation, gas tightness, stability to oxidizing and reducing atmospheres and similar thermal expansion coefficients to the other cell compartments. Most commercial SOFCs operate at 700 to 1000 °C and utilize similar materials: Yttria stabilized zirconia (YSZ) or gadolinium doped ceria are used as electrolyte. Porous Ni-YSZ cermets are used for anodes and strontium doped lanthanum manganate (LSM) is used

for cathodes. Currently, the limiting factor for cell performance is often the oxygen reduction reaction at the cathode and great effort is taken to develop cathode materials that facilitate high oxygen reduction rates even at intermediate temperatures (400 to 600 °C).

1.3 State of research

Mixed ionic electronic conducting (MIEC) perovskite oxides are attractive cathode materials due to their high oxygen reduction activity, and various materials are investigated, e.g. $La_xSr_{1-x}CoO_{3-\delta}$ (LSC),[1–8] $La_xSr_{1-x}FeO_{3-\delta}$ (LSF),[8–16] $La_xSr_{1-x}Co_yFe_{1-y}O_{3-\delta}$ (LSCF),[10,11,17–23] $Ba_xSr_{1-x}Co_yFe_{1-y}O_{3-\delta}$ (BSCF)[10,11,24–29] or $La_xSr_{1-x}Ti_yFe_{1-y}O_{3-\delta}$ (LSTF).[30–32] Moreover, their high oxygen ion conductivity allows for oxide transport through the electrode bulk and thus the whole MIEC|air interface becomes available for oxygen reduction. Understanding the oxygen reduction mechanism may give valuable insights into the limiting factors for oxygen reduction and thus aid in the search for catalytically highly active materials for oxygen reduction electrodes.

Point defects in the electrode play an essential role for oxygen reduction, not only because they facilitate mass and charge transport, but they also are reacting species in the oxygen reduction reaction according to

$$O_2 + 2\,V_O^{\bullet\bullet} + 4\,e' \longrightarrow 2\,O_O^{\times}. \tag{1.3}$$

Detailed knowledge about electrode defect concentrations in equilibrium and also under polarization is thus highly desirable. Equilibrium defect concentrations of bulk mixed conducting oxides are frequently investigated by e.g. coulometric titration or thermogravimetry.[2,14,19,33–38] Much less data exist on the defect chemical relations upon electrochemical polarization, that is under voltage bias.[2,15,16] Moreover, the exact defect chemistry of perovskite thin films was hardly investigated so far; thin film defect chemistry is not necessarily the same as for bulk materials, e.g. due to possible strain or interfacial effects.

Studies aiming at mechanistic information often investigate the exchange current density by means of tracer exchange,[2,39] conductivity relaxation[40] or impedance spectroscopy.[6,41–44] While the determination of oxygen exchange rates via such close-to-equilibrium methods is well established and frequently employed, it is nevertheless often challenging to extract mechanistic details from such experiments, also because experimental data frequently include effects of both cathodic and anodic reactions.[43,45,46] In contrast, experiments far from equilibrium, i.e. at sufficiently high electrode polarization, enhance the reaction rate in one direction while suppressing the reaction in reverse direction, and thus may offer a better view, for example

on the dependencies of reaction rates on concentrations. Nevertheless, measurements and mechanistic interpretations of oxygen reduction/evolution current-voltage curves are rather scarce,[16,47,48] and the concepts for a theoretical description of such current-voltage curves are still under development.[49,50] So far, experimental evidence was found that oxygen vacancies can play an important role in the rate limiting step of the oxygen reduction.[51] For example, from investigations of $Ba_xSr_{1-x}Co_yFe_{1-y}O_{3-\delta}$ it was concluded that the oxygen vacancy concentration and mobility are rate limiting for the oxygen reduction.[43] Also, DFT calculations for $La_xSr_{1-x}MnO_{3-\delta}$ suggest oxygen vacancy mobility and concentration as limiting factors.[52] On the other hand, studies on $SrTi_{1-x}Fe_xO_{3-\delta}$ suggest that the availability of conduction band electrons is the relevant factor for oxygen reduction kinetics. Clearly, more research is needed to determine the role of point defects for the oxygen reduction kinetics and ultimately reveal the reaction mechanism.

Moreover, many of these perovskite materials suffer from limited long term stability, i.e. resistance degradation which prevents industrial applications and also hampers experimental research of electrode kinetics as it convolutes the material inherent kinetic properties with the influence of thermal and chemical history. This may also be the reason for the often significant variation in reported values for kinetic parameters (i.e. oxygen exchange coefficients), despite extensive research by various methods, e.g. impedance spectroscopy,[13,20,53] conductivity relaxation[1] and isotope exchange experiments.[3] Several studies have linked the resistance degradation to segregation of Sr to the MIEC surface,[4,5,54] and recent studies could directly observe the adverse effect of Sr decoration on MIEC surfaces.[7] Different contaminants such as Si, SO_2 or Cr were found to cause increased degradation of the surface resistance, especially in the presence of humidity.[1,22,55,56] However, Sr segregation also occurs under nominally high purity conditions.[5]

In this thesis, dense $La_{0.6}Sr_{0.4}FeO_{3-\delta}$ thin film electrodes were grown by pulsed laser deposition to investigate their point defect chemistry and their oxygen exchange kinetics and to reveal the interrelationship between them. In chapter 2 an electrochemical method of determining point defect concentrations of thin $La_{0.6}Sr_{0.4}FeO_{3-\delta}$ films is discussed. Voltage and partial pressure dependent chemical capacitance measurements are used to reveal thin film defect concentrations under equilibrium and under polarisation. A bulk defect chemical model[35] is adapted to those data to extract thin film defect equilibrium enthalpies and entropies and reveal their deviation from bulk parameters.

Chapter 3 discusses a novel approach to obtain mechanistic information (i.e. reaction orders) from measured current voltage curves, and demonstrates this approach for LSF thin film electrodes. Making use of the equivalence of p_{O_2} and overpotential (η) with respect to their effect on defect concentrations discussed in chapter 2, the electrode overpotential can be adjusted

in such a way that it exactly counteracts the p_{O_2} induced μ_{O_2} changes, thus keeping oxygen chemical potential μ_{O_2} (and thereby defect concentrations) constant. The remaining p_{O_2} dependence then reflects only the "true" reaction order of p_{O_2} and reveals the nature of adsorbed oxygen species relevant for the oxygen reduction rate.

Chapter 4 expands on the approach shown in chapter 3 and presents a generalized framework for describing the kinetics of the oxygen exchange reactions on MIEC surfaces as a result of defect concentration and adsorbate changes. A rate equation is derived for the oxygen incorporation and release currents and exemplarily applied to two hypothetical mechanisms. The resulting p_{O_2} and η dependencies are explained as a consequence of the interplay between gas phase determined adsorbates as well as gas phase and overpotential dependent defect concentrations. Furthermore, generalized expressions for these dependencies are derived and those show that a simple interpretation of empirical dependencies is not always appropriate. Rather, the involved point defects and their dependencies on p_{O_2} and η need to be taken into account as well.

Lastly, in chapter 5 the resistance degradation of $La_{0.6}Sr_{0.4}FeO_{3-\delta}$ thin films is investigated. "In-situ" impedance spectroscopy inside the pulsed laser deposition chamber is employed to study the kinetics of freshly deposited films in their most pristine state and reveals a striking difference to conventional and "ex-situ" measurements. Controlled exposure to different potentially degrading environments and surface characterization by X-ray photoelectron spectroscopy are utilized to elucidate different driving forces and mechanisms for resistance degradation.

2 Determination of defect chemistry by chemical capacitance measurements

The study presented in this chapter has also been published as a scientific paper in "Physical Chemistry - Chemical Physics".[57]

2.1 Introduction

In this chapter, the use of electrochemical impedance spectroscopy to investigate the defect chemistry of $La_{0.6}Sr_{0.4}FeO_{3-\delta}$ thin films via their chemical capacitance is discussed. A three-electrode approach allows variation of the electrode polarization (overpotential) and, together with a variation of the oxygen partial pressure, defect chemical data become accessible over an oxygen chemical potential range spanning the equivalent of 15 orders of magnitude of oxygen partial pressure.

On bulk samples, the equilibrium defect chemistry of LSCF has already been investigated by different methods, for example coulometric titration, thermogravimetry, statistical thermodynamics calculations, carrier gas titration and electronic conductivity measurements.[2,14,19,33–38] Much less data exist on the defect chemical relations upon electrochemical polarization, that is under voltage bias.[2,15,16] Moreover, the exact defect chemistry of LSCF thin films was hardly investigated so far; thin film defect chemistry is not necessarily the same as for bulk materials, e.g. due to possible strain or interfacial effects. One experimental method particularly suited for investigating the defect chemistry of thin films is the measurement of the chemical capacitance, a capacitive property of mixed ionic and electronic conductors (MIECs) which depends on the charge carrier concentrations. This chemical capacitance reflects an oxides ability to change its stoichiometry in response to a change in oxygen chemical potential in the material.[58] In the case of dilute defects, and only one relevant electronic defect (eon) the chemical capacitance is given by[59]

$$C_{\mathrm{chem}} = \frac{e^2}{kT} n_{\mathrm{uc}} \left(\frac{1}{4c_{\mathrm{V}}} + \frac{1}{c_{\mathrm{eon}}} \right)^{-1}, \tag{2.1}$$

where c_V and c_{eon} denote concentration (in defects per unit cell) of vacancies and electronic defects, respectively; n_{uc} is the concentration of unit cells and e, k and T have their usual meanings of elementary charge, Boltzmann constant and temperature.

This equation already shows the direct relation between charge carrier (i.e. defect) concentrations and chemical capacitance. Detailed studies of chemical capacitances were performed on ceria thin films under reducing conditions.[60–63] Some data exist on LSF in air and humidified hydrogen,[10,13] for LSCF in air,[10,20] and for $La_{0.6}Sr_{0.4}CoO_{3-\delta}$ in the range between 0.25 mbar and 1 bar oxygen and under polarization.[2,6,10] However, chemical capacitance measurements of LSCF with in-depth quantitative analysis are still missing. More general, chemical capacitance measurements are not yet an established routine tool for defect chemical investigations of thin films.

2.2 Experimental

2.2.1 Three-electrode samples

Double side polished yttria stabilized zirconia (YSZ) (100) single crystals (Crystec, Germany) ($5 \times 5 \times 1\,mm^3$) were used as electrolyte substrates. A reference electrode was prepared by brushing a LSF/Pt-paste mixture into a notch around the substrate circumference and sintering for 2 h at 850 °C. Platinum current collector grids with 30/5 µm mesh/strip width and 100 nm thickness were prepared on both substrate sides by lift-off lithography and magnetron sputter deposition to ensure complete and homogeneous polarization of the entire oxide electrodes. Dense LSF thin film working electrodes were produced by pulsed laser deposition (PLD). The target was prepared from $La_{0.6}Sr_{0.4}FeO_{3-\delta}$ powder (Sigma Aldrich) by cold isostatic pressing (150 MPa) and sintering in air (12 h, 1200 °C). Phase purity of the target was checked by X-ray diffraction. Ablation was done at 600 °C substrate temperature and 0.04 mbar oxygen pressure using a KrF excimer laser (Complex Pro 201F, 248 nm) with 400 mJ laser pulses at 5 Hz. The target to substrate distance was 6 cm. Samples with LSF film thicknesses from 28 ± 5 to 116 ± 5 nm were produced; the film thickness was determined by profilometer measurements. Additionally, samples with platinum covered working electrodes were prepared by sputtering 300 nm platinum onto LSF films of 28 ± 5 to 116 ± 5 nm thickness. Similar LSF films (using the same deposition parameters) were already described in Ref. [13] and revealed columnar grain growth with column sizes of about 50 nm. Porous $La_{0.6}Sr_{0.4}CoO_{3-\delta}$ counter electrodes with low polarization resistance were also prepared by PLD (400 mJ, 5 Hz) at 450 °C and 0.4 mbar oxygen.[4] A sketch of the prepared three-electrode samples is shown in figure 2.1a.

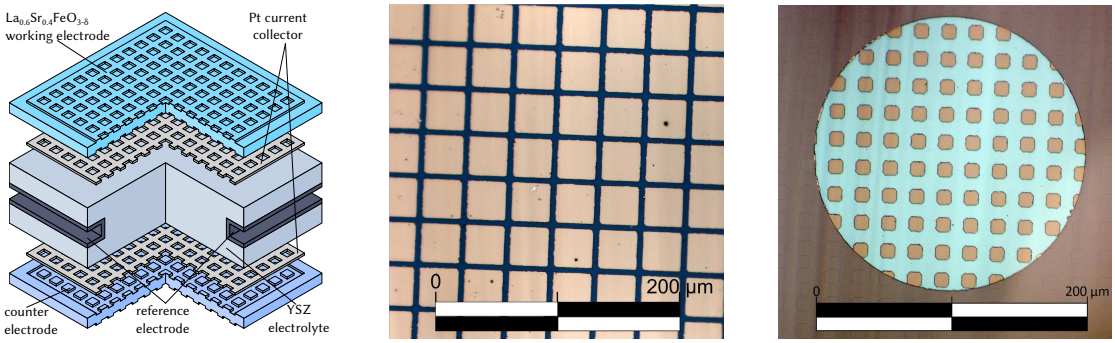

(a) 3 electrode sample **(b)** macroelectrode **(c)** microelectrode

Figure 2.1: Schematic of a three-electrode sample with platinum current collectors beneath the LSF working electrode and the counter electrode (a) and bright field microscope images of the macroelectrode surface (b) and a microelectrode (c) with visible current collectors. The active LSF surface area (directly above the electrolyte) is 25 % (microelectrode) or 73.5 % (macroelectrode) of the total electrode area.

2.2.2 Microelectrodes

Further samples were fabricated with circular LSF microelectrodes of 200 µm diameter and 40 nm thickness. In this case, counter electrodes of porous LSF/Pt were brushed on the non-polished side of single side polished YSZ (100) single crystals and sintered for 2 h at 850 °C. Platinum current collector grids of 10/10 µm mesh/strip width were prepared by magnetron sputtering on the polished side, as described above. LSF thin films were again deposited on top by PLD. Microstructuring of the electrode films including current collector grids was done by argon ion beam etching (tectra GmbH, ionEtch Sputter Gun) at 1.1×10^{-4} mbar Ar, with a beam current of 2 mA for 25 min.

2.2.3 Impedance spectroscopy

Impedance spectra were measured with a Novocontrol PotGal electrochemical test station and a Novocontrol Alpha A impedance analyser in potentiostat mode, with applied DC voltages between working and reference electrode from 0 to −600 mV. An AC voltage of 10 mV rms and a frequency range of 1 MHz to 10 mHz were used. Each frequency point was measured for at least one second and one period. Measurements were performed between 500 °C and 650 °C with different oxygen/nitrogen mixtures (0.25 mbar to 1 bar O_2) (Alphagaz, 99.995 %) in a closed apparatus of fused silica. For the three-electrode samples, working and counter electrodes were contacted between two platinum sheets, the reference electrode was contacted with platinum thread. Microelectrode samples were contacted by a platinum sheet (counter electrode) and a platinum needle (microelectrode).

2.3 Results and discussion

2.3.1 Impedance spectra and determination of the chemical capacitance

Figure 2.2 displays representative impedance spectra for different oxygen partial pressures (figure 2.2a) and DC bias voltages (figure 2.2b). Spectra exhibit a high frequency resistive offset and a dominant low frequency semicircle. The high frequency offset shows no dependence on oxygen partial pressure or applied DC voltage. The value of this high frequency offset (34 Ω at 600 °C) agrees very well with the ionic transport resistance in the YSZ electrolyte substrate between working and reference electrode.

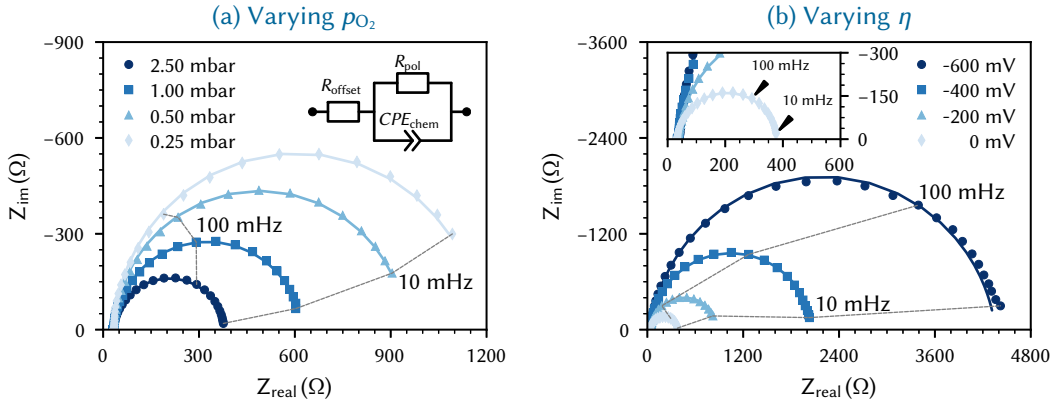

Figure 2.2: Typical impedance spectra of three-electrode samples measured at 600 °C in various oxygen partial pressures without bias (a), and under different cathodic polarization in 2.5 mbar oxygen (b). The spectra were determined on a 116 nm thick LSF film. Symbols are measured data, lines represent fits of the low frequency data to the equivalent circuit model (see inset in figure 2.2a). The inset in figure 2.2b shows a zoom on the high frequency region.

The low frequency semicircle shows a clear dependence on oxygen pressure and DC voltage. It can be fitted to a parallel R-CPE element and a serial resistance, where the constant phase element (CPE) was used to model an imperfect capacitor with impedance $Z_{\mathrm{CPE}} = Q^{-1}(i\omega)^{-P}$, see circuit in figure 2.2.[64] Experimental P-values close to one (typically between 0.91 and 1) indicate nearly ideal capacitive behaviour. For certain measurement parameters, especially at low oxygen partial pressure, only part of the low frequency semicircle was accessible by the frequency range employed here. However, the capacitive contribution could always be determined from the measured data points with small fit errors (typically <1 %).

From the fit results (R_{pol}, Q, P) the area-specific capacitance C was calculated by

$$C = \frac{\left({R_{pol}}^{1-P}Q\right)^{\frac{1}{P}}}{A}, \tag{2.2}$$

with the electrode area A.[64] The resulting values in the range of 1 to 15 mF cm^{-2} are much higher than any double layer capacitances of an electrode, but are very common for chemical capacitances found in LSCF electrodes.[13,15,20,24]

Hence, the dominating semicircle feature of the spectrum is interpreted in accordance with similar spectra found in literature for LSCF electrodes[10,13,18,20] or similar mixed conducting electrodes.[2,43,60] This means that the resistance of the large semicircle is caused by the oxygen surface exchange reaction and the capacitance reflects the chemical capacitance of the film. The ionic and electronic across-plane transport resistances, as well as the in-plane electronic transport resistance are negligible compared to the surface exchange resistance. Contributions from the LSF|YSZ interface can also be neglected, as measured impedance spectra do not show any distinct interfacial (intermediate frequency) features. Moreover, from literature and our own previous experiments with different current collector geometries, we can conclude that the electrode volume above the current collector grid is inactive towards oxygen exchange and does not contribute to the chemical capacitance due to the large in-plane ionic sheet resistance.[13] Therefore, the chemical capacitance was normalized to the free thin film volume (73.5 % of the total film volume for three-electrode samples, and 25 % for microelectrode samples), i.e. it was calculated according to

$$C_{chem} = \frac{C}{df}, \tag{2.3}$$

where C is the area specific capacitance, d is the film thickness and f the active electrode fraction. It is noteworthy, that while a continuous increase of the surface exchange resistance over the course of the experiment was observed, the chemical capacitance was very stable, with typically less than 1 % change within 12 h measuring time.

2.3.2 Oxygen partial pressure and voltage dependency of the chemical capacitance

Figure 2.3 shows the equilibrium chemical capacitance (i.e. without applied DC voltage) as function of the oxygen partial pressure. With increasing oxygen partial pressure, the chemical capacitance decreases, see also the more detailed interpretation below. In the high p_{O_2} region the decrease of the chemical capacitance levels off.

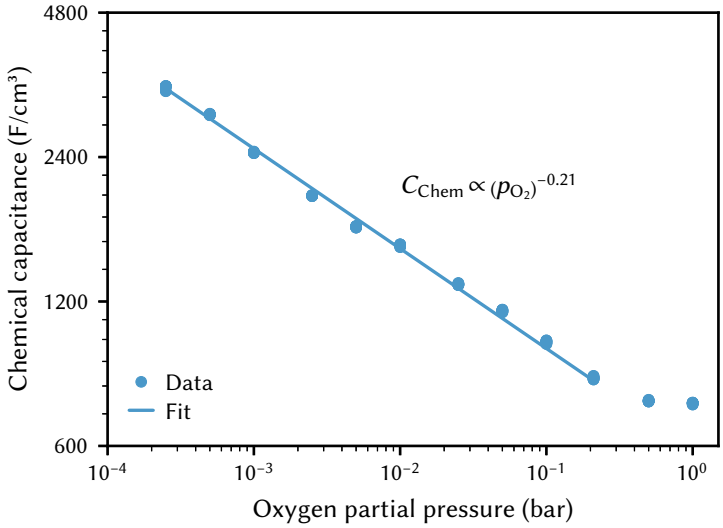

Figure 2.3: Equilibrium chemical capacitance at 600 °C (circles) as a function of p_{O_2}, measured on a 40 nm thin LSF film, and fit to a power law (solid line).

Figure 2.4 displays the chemical capacitances under DC polarization, where the electrode overpotential η was calculated from the voltage between working and reference electrode U_{DC} by correcting for ohmic losses in the electrolyte ($R_{offset} I_{DC}$), i.e.

$$\eta = U_{DC} - R_{offset} I_{DC} \,. \tag{2.4}$$

The ohmic resistance R_{offset} was determined by impedance spectroscopy, and I_{DC} is the measured current through the cell.

The C_{chem} vs. η curves measured in different atmospheres are very similar except for a shift on the overpotential axis. This voltage shift $\Delta\eta$ between curves for different partial pressures (p_1 and p_2) equals the Nernst voltage calculated from these partial pressures according to

$$\Delta\eta = \frac{kT}{4e} \ln\left(\frac{p_1}{p_2}\right). \tag{2.5}$$

To further quantify and compare the impacts of oxygen partial pressure and electrode polarization, we have to consider the distribution of the oxygen chemical potential in a three-electrode system. We define an oxygen chemical potential of the surrounding atmosphere ($\mu^{at}_{O_2}$), which is assumed to be constant in the entire apparatus, i.e. at all electrodes. Pure oxygen at 1 bar is used as a reference for the oxygen chemical potential, i.e. $\mu_{O_2} = 0$ for $p_{O_2} = 1\,\mathrm{bar}O_2$. Without applied DC bias, all electrodes (working electrode WE, counter electrode CE and ref-

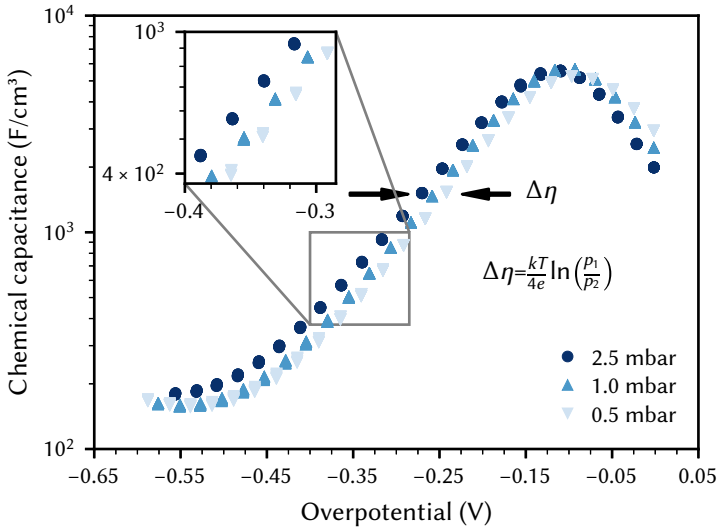

FIGURE 2.4: Chemical capacitance of a 40 nm thin LSF film, measured at 600 °C as a function of electrode overpotential (η) and oxygen partial pressure. The shift on the potential axis is equal to the Nernst voltage between the atmospheres with oxygen partial pressures p_1 and p_2, respectively.

erence electrode RE) are in equilibrium with the atmosphere, thus their oxygen chemical potentials ($\mu_{O_2}^{WE}$, $\mu_{O_2}^{CE}$ and $\mu_{O_2}^{RE}$) are equal to $\mu_{O_2}^{at}$. The oxygen chemical potential in any electrode relative to 1 bar oxygen is thus given by

$$\mu_{O_2}^{at} = kT \ln\left(\frac{p_{O_2}}{1\,\text{bar}}\right). \tag{2.6}$$

When applying a DC voltage between working and counter electrode, the resulting chemical potential distribution strongly depends on the spatial position of the rate limiting step. In our case (dense thin film electrodes with current collector grids) we assume the following conditions, in agreement with literature:[10,13,18,20]

- The electron transport in the electrode film is fast. Thus, electronic transport resistances can be neglected and the electrochemical potential of electrons is constant in the entire electrode film. This is reasonable as LSF has high electronic conductivity, the across-plane transport length is short (40 nm) and the lateral electron transport is augmented by the current collector.

- The across-plane oxygen transport is fast compared to the surface exchange reaction. Therefore, the entire electrode reaction is surface limited, and the electrochemical potential of oxide ions is constant in the electrode film.
- The YSZ|LSF interface does not contribute any significant transport resistance, therefore no electrochemical potential discontinuity occurs at the interface.

Under these assumptions, the oxygen chemical potential and the electrochemical potentials of oxide ions and electrons are distributed as depicted in figure 2.5.

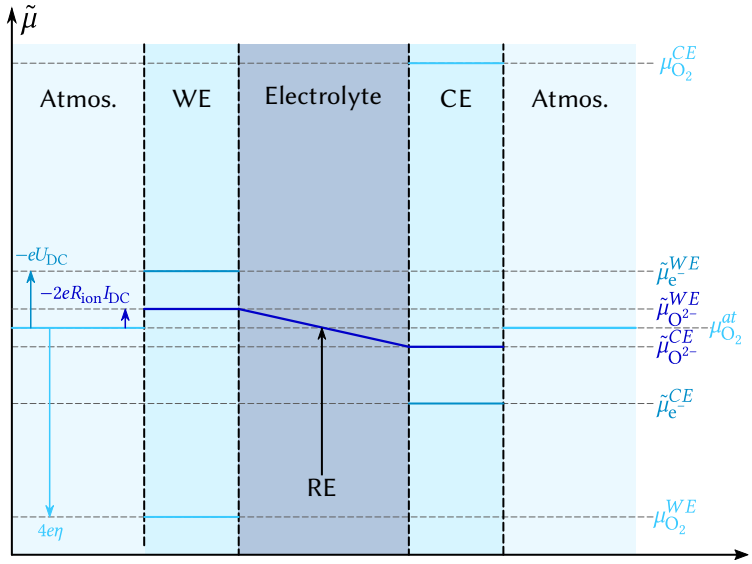

Figure 2.5: Electrochemical potential distribution of oxygen (μ_{O_2}), oxide ions ($\tilde{\mu}_{O^{2-}}$) and electrons ($\tilde{\mu}_{e^-}$) in a three-electrode sample, during cathodic polarization of the working electrode (WE). Within the electrodes, potentials are constant due to high ionic/electronic conductivity. Potential drops occur at surfaces due to the rate limiting surface exchange reaction. A potential gradient exists in the electrolyte because of finite ionic conductivity. RE and CE denote reference and counter electrode, respectively.

A current flow I_{DC} is imposed between working and counter electrode, causing a voltage U_{DC}, i.e. an electron electrochemical potential difference between working and reference electrode. No current flows through the reference electrode, thus it remains in equilibrium with the gas phase, i.e. at $\mu_{O_2}^{RE} = \mu_{O_2}^{at}$. The DC voltage drop

$$\tilde{\mu}_{e^-}^{WE} - \tilde{\mu}_{e^-}^{RE} = -eU_{DC} \tag{2.7}$$

is partially reflected by the oxide electrochemical potential ($\tilde{\mu}_{O^{2-}}$) gradient in the electrolyte caused by the ionic transport resistance R_{ion}. In accordance with figure 2.5, this leads to

$$\tilde{\mu}_{O^{2-}}^{\text{WE}} - \tilde{\mu}_{O^{2-}}^{\text{RE}} = -2eI_{\text{DC}}R_{\text{ion}}\,. \tag{2.8}$$

The resulting oxygen chemical potential in the working electrode $\mu_{O_2}^{\text{WE}}$, relative to $\mu_{O_2}^{\text{RE}}$ (and thus to $\mu_{O_2}^{\text{at}}$), follows from $\mu_{O_2} = 2\tilde{\mu}_{O^{2-}} - 4\tilde{\mu}_{e^-}$. It is given by

$$\mu_{O_2}^{\text{WE}} - \mu_{O_2}^{\text{RE}} = 2\left(\tilde{\mu}_{O^{2-}}^{\text{WE}} - \tilde{\mu}_{O^{2-}}^{\text{RE}}\right) - 4\left(\tilde{\mu}_{e^-}^{\text{WE}} - \tilde{\mu}_{e^-}^{\text{RE}}\right), \tag{2.9}$$

and thus from equations (2.7) to (2.9) we find

$$\mu_{O_2}^{\text{WE}} - \mu_{O_2}^{\text{RE}} = 4e\left(U_{\text{DC}} - I_{\text{DC}}R_{\text{ion}}\right) = 4e\eta\,, \tag{2.10}$$

where η is the overpotential of the working electrode. The definition of the electrode overpotential introduced above, in equation (2.4) is in accordance with equation (2.10) when neglecting all contributions to R_{offset} other than R_{ion}. Relative to the reference chemical potential of 1 bar oxygen, the oxygen chemical potential inside the working electrode follows from equations (2.6) and (2.10) as

$$\mu_{O_2}^{\text{WE}} = 4e\eta + kT\ln\left(\frac{p_{O_2}}{1\,\text{bar}}\right). \tag{2.11}$$

This equation shows that under the given assumptions, the oxygen chemical potential, and thus the defect chemical state of the working electrode, is unambiguously defined by the oxygen partial pressure in the gas and the electrode overpotential. This equivalence was also used by Kawada et al. when analysing the oxygen vacancy concentration in LSC.[2] Another point of view on the oxygen chemical potential can be introduced by defining an equivalent oxygen pressure of the working electrode $\acute{p}_{O_2}^{\text{WE}}$.[2] It is related to the oxygen chemical potential in the working electrode by

$$\mu_{O_2}^{\text{WE}} = kT\ln\left(\frac{\acute{p}_{O_2}^{\text{WE}}}{1\,\text{bar}}\right) \tag{2.12}$$

and according to equation (2.11) it is thus defined by

$$\acute{p}_{O_2}^{\text{WE}} = p_{O_2}\exp\left(\frac{4e\eta}{kT}\right). \tag{2.13}$$

We may now plot the chemical capacitance versus the electrode oxygen chemical potential (relative to 1 bar oxygen), i.e. versus the equivalent oxygen pressure. This leads to a perfect match of all curves measured in different atmospheres, as shown in figure 2.6. We can thus

conclude that the measured capacitance of the LSF films is defined by the chemical potential of oxygen within the thin film solely, regardless of the actual atmospheric oxygen partial pressure or electrode overpotential. This also strongly supports the assumptions made above, particularly the absence of a chemical potential gradient across the LSF film. The interpretation of the CPE in the impedance analysis in terms of a chemical capacitance is thus reasonable and reflects the defect chemical state of LSF. In the regimes between 2.5×10^{-4} bar and 2.0×10^{-1} bar oxygen (figure 2.3) and from 10^{-7} to 10^{-12} bar equivalent oxygen pressure (figure 2.6) the C_{chem} curves can be fitted to a power law, with exponents of -0.21 (figure 2.3) and 0.20 (figure 2.6), respectively.

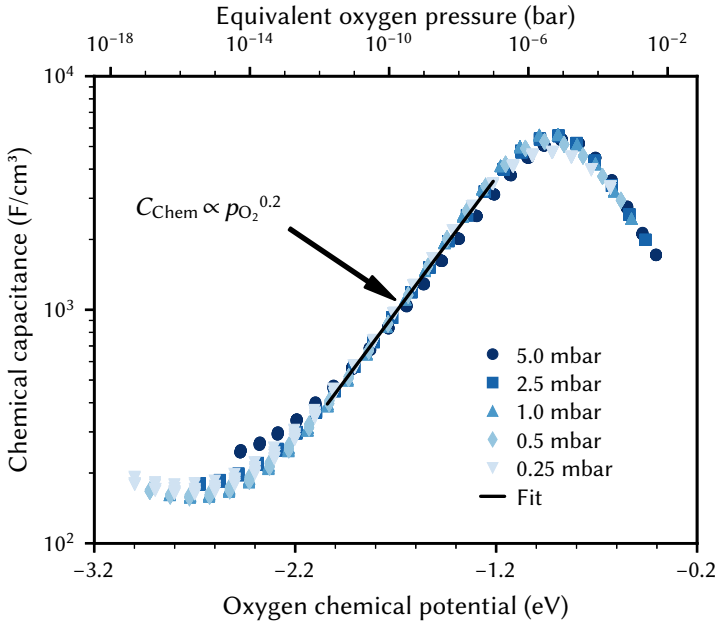

Figure 2.6: Chemical capacitance of a 40 nm thin LSF film at 600 °C (symbols) as a function of the oxygen chemical potential (or equivalent oxygen pressure) of LSF and fit of the values between −2.0 eV and −1.2 eV to a power law (line).

2.3.3 Influence of film thickness

Figure 2.7 shows chemical capacitances measured on LSF films of different thickness, normalized to the LSF film volume. In the regime between −0.2 eV and −1.6 eV oxygen chemical potential, these curves exhibit almost no difference. This means that the area specific capacitances scale linearly with the thin film thickness. This is consistent with the interpretation

of this capacitance as the chemical capacitance of the LSF electrode bulk. However, below −1.6 eV the volume-specific capacitance is higher for the thinner films. These deviations are most prominent around the capacitance minimum at −2.8 eV.

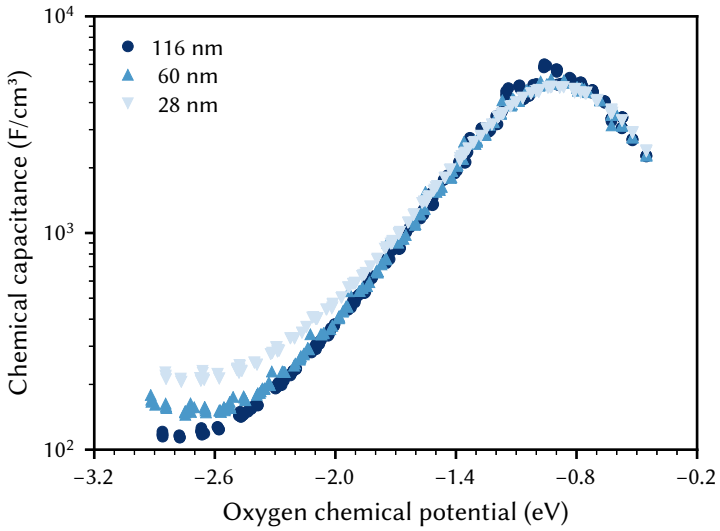

FIGURE 2.7: Chemical capacitance at 600 °C as a function of the oxygen chemical potential and film thickness. Each curve consists of measurements in different oxygen partial pressures between 2.5×10^{-4} bar and 2.5×10^{-3} bar oxygen.

Figure 2.8a displays the measured chemical capacitance, normalized to the active electrode area, as a function of film thickness at different oxygen chemical potentials. The measured capacitances show a linear dependence on the film thickness, as expected for a bulk chemical capacitance. However, fitting these data to a linear function and extrapolating to zero film thickness yields an intercept on the capacitance axis of 0.3 to 0.45 mF cm^{-2}. Thus, the measured capacitance can be separated into a volume-specific chemical capacitance and a volume independent contribution, most likely due to an interface, either LSF|YSZ, LSF|Pt or LSF|Air. Grain boundaries as origin can be excluded because their contribution should again scale with thickness. Similar volume independent contributions to the measured chemical capacitance have also been found on ceria.[60] At high oxygen chemical potentials, the volume related chemical capacitance is large, and masks the volume independent interfacial capacitance. Close to the capacitance minimum, however, the interface-related capacitance contributes 60 % (for 28 nm LSF) to 25 % (for 116 nm LSF) to the entire electrode capacitance. The interfacial capacitance depends only weakly on the oxygen chemical potential, see figure 2.8b, and the measured dependence might easily be an artefact due to the extrapolation for only a few thickness values.

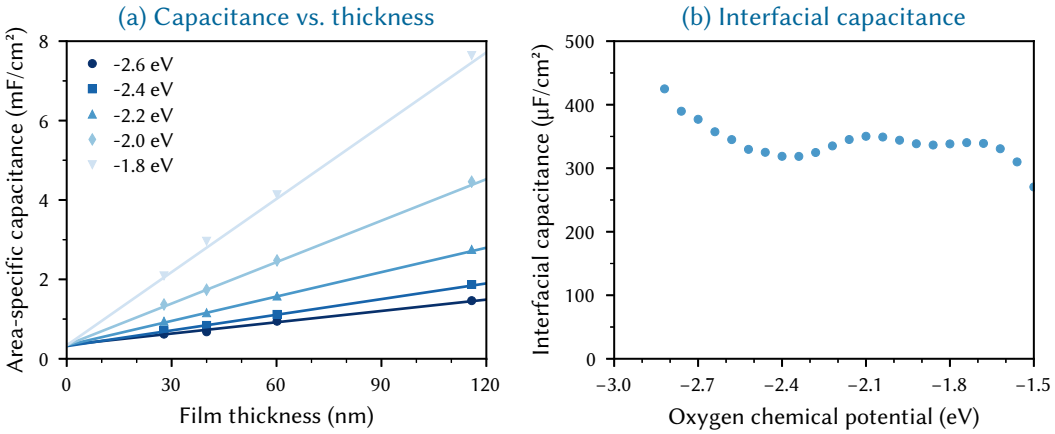

Figure 2.8: (a) Area-specific capacitance of LSF as a function of film thickness for various oxygen chemical potentials (μ_{O_2}), measured at 600 °C. Only the area of LSF above YSZ is considered. Symbols are measured data, lines represent linear fits. (b) Interface capacitance obtained from extrapolating the linear fits to zero thickness as a function of oxygen chemical potential.

To investigate the origin of this capacitance, samples with platinum covered working electrodes were measured. Covering the LSF surface with platinum increases the LSF|Pt interfacial area and eliminates the LSF|air interface. Figure 2.9 shows the capacitance measured on samples with and without platinum on top of LSF as a function of oxygen chemical potential for different film thicknesses. There is almost no difference between samples with and without Pt cover, which strongly suggests that the interfacial capacitance is located at the LSF|YSZ interface rather than at the LSF|Pt interface. This conclusion is further supported by a comparison of capacitance measurements on samples with different fractions of the YSZ surface covered by a current collector grid (25 % for the three-electrode samples and 75 % for the microelectrodes), see figure 2.10. When normalized to the active LSF volume on YSZ, see equation (2.3), very good agreement is found. However, it remains an open question, which atomistic mechanism at the LSF|YSZ interface causes the corresponding almost p_{O_2} independent interfacial capacitance of about 400 µF cm^{-2}.

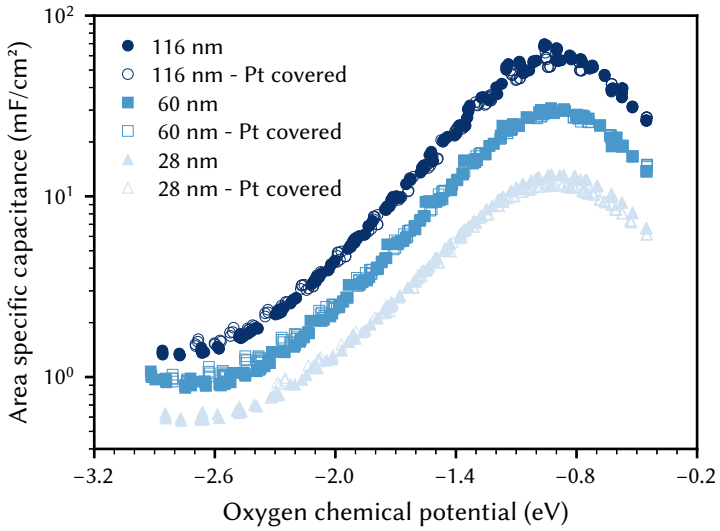

Figure 2.9: Area-specific capacitance of LSF versus oxygen chemical potential for three different film thicknesses, measured at 600 °C, all normalized to the LSF|YSZ interface area. The filled symbols are data from LSF samples without a platinum cover layer, the open symbols are data from LSF samples with a 300 nm platinum layer sputtered onto the LSF surface, eliminating the LSF|air interface.

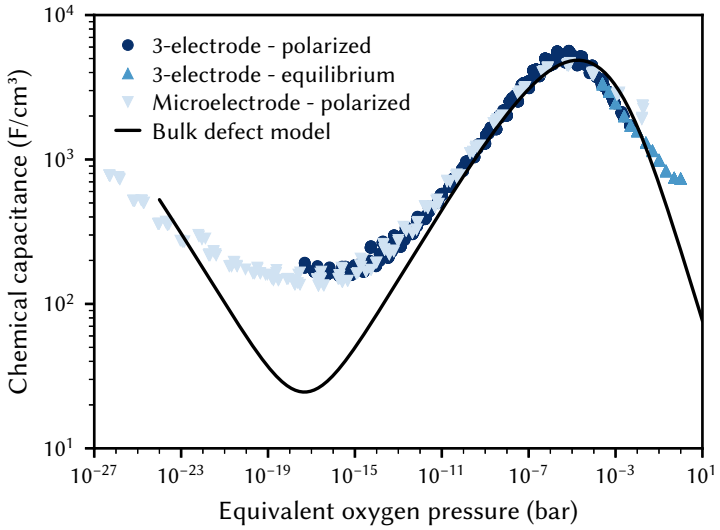

Figure 2.10: Chemical capacitance at 600 °C as a function of equivalent oxygen partial pressure, measured on macroscopic three-electrode samples (40 nm) under cathodic bias in 0.25 to 5 mbar oxygen as well as in equilibrium with the gas phase in 0.25 mbar to 1 bar oxygen, and 2-point microelectrode samples (40 nm) in 10 mbar to 1 bar oxygen.

2.3.4 Defect chemical analysis of the chemical capacitance measurements

Bulk defect model

For bulk LSF, a defect model is provided by Mizusaki et al.[8,35] In this model the main defect chemical charge carriers are oxygen vacancies $V_O^{\bullet\bullet}$, electrons Fe'_{Fe} and electron holes $Fe^{\bullet}_{Fe}$. Enthalpies and entropies for the oxygen incorporation ($V_O^{\bullet\bullet} + 1/2\ O_2 + 2\ Fe^{\times}_{Fe} \rightleftharpoons O^{\times}_O + 2\ Fe^{\bullet}_{Fe}$) and the electron/hole pair formation ($2\ Fe^{\times}_{Fe} \rightleftharpoons Fe^{\bullet}_{Fe} + Fe'_{Fe}$) were determined for bulk LSF by Kuhn et al. via thermogravimetry and coulometric titration, see table 2.1.[14] From these data, the defect concentrations can be calculated as a function of the oxygen partial pressure; figure 2.11 shows the resulting Brouwer diagram at 600 °C.

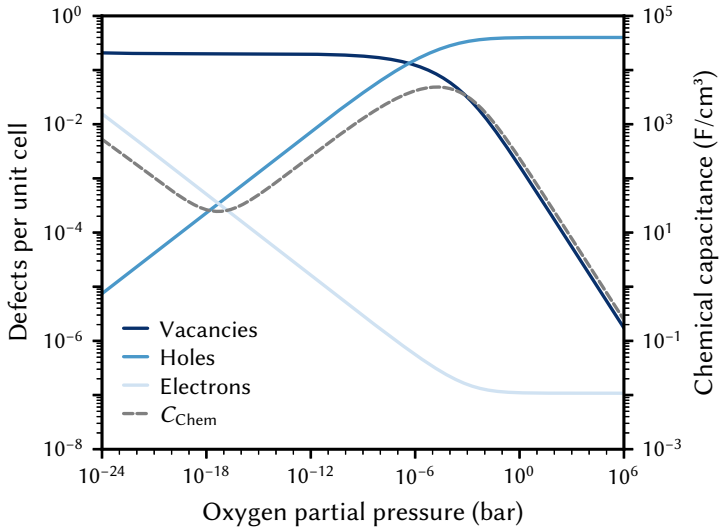

Figure 2.11: Brouwer diagram for bulk LSF at 600 °C, based on literature data, with chemical capacitance calculated according to equation (2.21).[14]

For mixed conducting oxides, the chemical capacitance is defined in Ref. [59] as

$$C_{\text{chem}} = 8e^2 n_{\text{uc}} \frac{\partial c_O}{\partial \mu_{O_2}}, \tag{2.14}$$

where c_O denotes the concentration of formally neutral oxygen, i.e. the combination of an oxide ion and two electron holes, and μ_{O_2} is the chemical potential of oxygen in the film. The concentration is with respect to one unit cell and n_{uc} is the concentration of unit cells. Since

for every neutral oxygen atom added, one vacancy is annihilated ($\partial c_O = -\partial c_V$), we can write

$$C_{chem} = -8e^2 n_{uc} \left(\frac{\partial \mu_{O_2}}{\partial c_V} \right)^{-1} \tag{2.15}$$

where c_V is the concentration of oxygen vacancies. The chemical potential of oxygen is

$$\mu_{O_2} = 2\tilde{\mu}_{O^{2-}} + 4\tilde{\mu}_{h^\bullet} = -2\tilde{\mu}_{V_O^{\bullet\bullet}} + 4\tilde{\mu}_{h^\bullet}\,, \tag{2.16}$$

with $\tilde{\mu}_{O^{2-}}$, $\tilde{\mu}_{V_O^{\bullet\bullet}}$ and $\tilde{\mu}_{h^\bullet}$ denoting the electrochemical potentials of oxide ions, oxygen vacancies and electron holes, respectively. Combining equations (2.15) and (2.16) yields

$$\begin{aligned} C_{chem} &= -4e^2 n_{uc} \left(-\frac{\partial \tilde{\mu}_{V_O^{\bullet\bullet}}}{\partial c_V} + 2\frac{\partial \tilde{\mu}_{h^\bullet}}{\partial c_V} \right)^{-1} \\ &= -4e^2 n_{uc} \left(-\frac{\partial \tilde{\mu}_{V_O^{\bullet\bullet}}}{\partial c_V} + 2\frac{\partial \tilde{\mu}_{h^\bullet}}{\partial c_h}\frac{\partial c_h}{\partial c_V} \right)^{-1}, \end{aligned} \tag{2.17}$$

where c_h is the concentration of electron holes. If the electron concentration is negligibly small, i.e. under oxidizing conditions, electroneutrality requires $\partial c_h = -2\partial c_V$ and therefore

$$C_{chem} = 4e^2 n_{uc} \left(\frac{\partial \tilde{\mu}_{V_O^{\bullet\bullet}}}{\partial c_V} + 4\frac{\partial \tilde{\mu}_{h^\bullet}}{\partial c_h} \right)^{-1}. \tag{2.18}$$

If all defects i are sufficiently dilute, their chemical potentials can be described by Boltzmann's statistics with

$$\mu_i = \mu_i^0 + kT \ln c_i\,, \tag{2.19}$$

where μ_i^0 is the standard chemical potential. We thus obtain

$$C_{chem} = \frac{e^2}{kT} n_{uc} \left(\frac{1}{4c_V} + \frac{1}{c_h} \right)^{-1} \tag{2.20}$$

for dilute defects and oxidizing conditions.[58,59,65] The same equation with electron concentration instead of hole concentration is valid if electron holes are negligible. For more than two relevant defect species the equations become more complicated, cf. Ref. [66]. In case of similar concentrations of dilute electrons and electron holes we get, for example:

$$C_{chem} = \frac{e^2}{kT} n_{uc} \left(\frac{1}{4c_V} - \frac{1}{2c_h}\frac{\partial c_h}{\partial c_V} \right)^{-1}, \tag{2.21}$$

where $\partial c_h = -2\partial c_V + \partial c_e$.

Based on these defect chemical considerations and the thermodynamic data of Ref. [14] the volume-specific chemical capacitance of bulk LSF can be calculated and the corresponding curve is given in figure 2.11. At high oxygen partial pressures the calculated chemical capacitance is determined by the oxygen vacancy concentrations and thus shows a slope of -0.5. Towards lower oxygen partial pressures it passes a maximum with equally important oxygen vacancies and electron holes. Then it decreases with decreasing hole concentration (slope 0.25) and reaches a minimum for the electronically intrinsic point ($c_h = c_e$). Finally, C_{chem} again increases towards even more reducing conditions, in accordance with the increasing electron concentration.

This dilute defect model qualitatively explains the shape of the measured chemical capacitance curve, and in the low μ_{O_2} regime the exponent of the chemical capacitance versus equivalent oxygen partial pressure curve (0.2) is indeed close to the expected value of 0.25. However, two serious deviations become obvious when quantitatively comparing the calculated and the measured chemical capacitances, see figure 2.10. At high oxygen partial pressures (above 10 mbar) the measured chemical capacitance decreases much shallower (-0.21) than predicted by the dilute model (-0.5), and the capacitance value at the minimum is much larger than expected.

The deviation from the ideal behaviour for high oxygen partial pressures may be due to hole/hole interactions, since the expected electron hole concentration in this regime is very high (0.4 per unit cell). An excess energy of hole formation due to this interaction might make further oxygen incorporation less favourable, leading to less decrease in oxygen vacancy concentration, and thus less decrease in chemical capacitance when increasing the oxygen partial pressure. Similar hole/hole interactions were also found for other perovskite materials, $Ba_{1-x}La_xFeO_{3-\delta}$ and $La_{1-x}Sr_xCoO_{3-\delta}$.[67,68] One reason for the increased capacitance around the expected minimum was already identified above and attributed to the LSF|YSZ interface. This interfacial contribution can be subtracted and in the following the remaining volume-specific chemical capacitance is used to derive thermodynamic data for oxygen incorporation and electron/hole pair formation.

Thermodynamic defect data of LSF films

The capacitances of a 116 nm LSF film were measured at four temperatures between 500 °C and 650 °C, see figure 2.12. Lower temperatures lead to very low relaxation frequencies in the impedance spectra and thus might cause some fit errors, cf. the slightly step-like curve at 500 °C. For the sake of simplicity, curves of all temperatures were corrected by the interfacial capacitance determined at 600 °C, see figure 2.8. Figure 2.12 shows this corrected chemical capacitance at different temperatures as a function of oxygen chemical potential.

These data were fitted based on the dilute bulk defect model and equation (2.21) to extract equilibrium constants for the oxygen incorporation reaction

$$K_{ox} = \frac{(3 - c_V)\, {c_h}^2}{c_V (1 - c_h - c_e)^2 \sqrt{p_{O_2}}} \tag{2.22}$$

and the electron/hole pair formation

$$K_i = \frac{c_h c_e}{(1 - c_h - c_e)^2}\,. \tag{2.23}$$

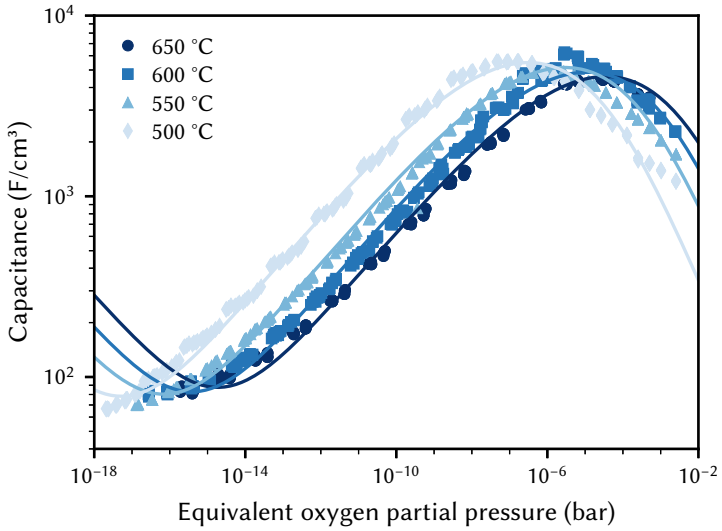

Figure 2.12: Corrected chemical capacitance of LSF (116 nm thin film) at different temperatures as a function of equivalent oxygen partial pressure. The interface capacitance obtained from film thickness variation at 600 °C (see figure 2.8b) has been subtracted. (Outside the μ_{O_2} range of figure 2.8 the averaged value of C_{int} was subtracted.) Symbols are measured data, lines are fits to the bulk defect model according to equation (2.21).

These fits agree very well with our data, with slight deviations in the higher oxygen partial pressure range, probably due to the neglected defect interactions, see above. The equilibrium constants obtained from these fits are shown in the Van 't-Hoff plot in figure 2.13. Fitting these to

$$\ln K = \frac{\Delta H}{RT} - \frac{\Delta S}{R} \tag{2.24}$$

yields enthalpies and entropies for oxygen incorporation and electron/hole pair formation, see table 2.1.

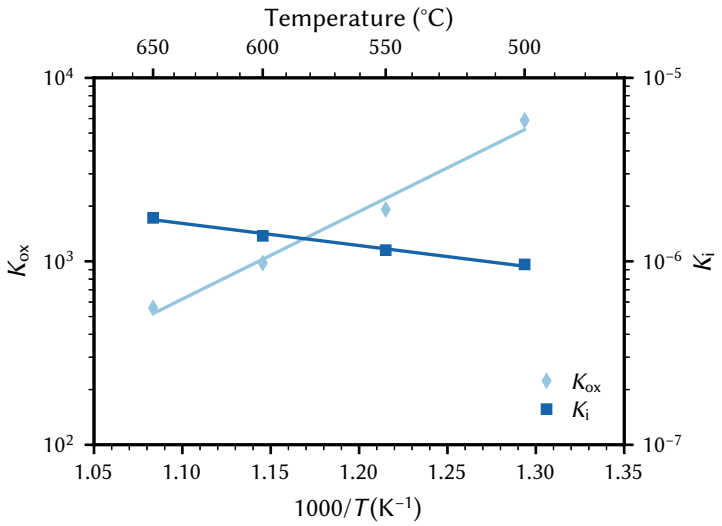

Figure 2.13: Equilibrium constants for the oxygen incorporation reaction (K_{ox}) and for the electron/hole pair formation (K_i) obtained from figure 2.12 versus inverse temperature and fits according to equation (2.24).

The resulting oxygen incorporation entropy and enthalpy agree very well with thermodynamic data of bulk LSF.[14] However, the deduced electron/hole pair formation enthalpy and entropy are both lower than for bulk LSF.[8,14,35] Possible reasons include effects of film strain and its changes with changing oxygen chemical potential, some differences in the exact stoichiometry (cation vacancies) or different pressure ranges used to deduce data, see below. Additionally, grain boundaries in our nanocrystalline thin films may cause deviations from literature bulk data. Since the oxidation state in the grain boundaries is probably different than in the grains, a shifted C_{chem} vs. p_{O_2} curve results, which adds to the grain chemical capacitance. A more detailed analysis however, would require further data points in the very low p_{O_2} beyond the capacitance minimum.

Table 2.1: Reaction enthalpies and entropies for oxygen incorporation (ΔH_{ox}, ΔS_{ox}) and electron/hole formation (ΔH_i, ΔS_i) in LSF extracted from chemical capacitance measurements on thin films, and bulk data from literature.[14]

		This study	Literature (bulk)
ΔH_{ox}	(kJ mol^{-1})	−94	−95.62 ± 4.18
ΔS_{ox}	(J mol^{-1} K^{-1})	−50	−54.27 ± 4.43
ΔH_i	(kJ mol^{-1})	26	95.75 ± 2.05
ΔS_i	(J mol^{-1} K^{-1})	−81	−21.63 ± 2.13

These experiments demonstrate that chemical capacitance measurements are a powerful alternative method for analysing the defect concentrations and defect thermodynamics of oxide materials, particular for thin films. Such an approach to the defect chemistry by C_{chem} measurements has even some advantages compared to common gravimetric studies: Since the chemical capacitance probes primarily minority charge carriers, it might be more sensitive to defect interactions causing vacancy changes in the hole conducting regime (see above). Moreover, compared to gravimetric studies a less broad p_{O_2} regime is already sufficient to obtain thermodynamic data. This is detailed in figure 2.14 for different equilibrium constants. In gravimetric studies both steps indicating weight loss for increasing vacancies have to be observed. In C_{chem} studies, however, only the regime between the capacitance maximum and minimum is required.

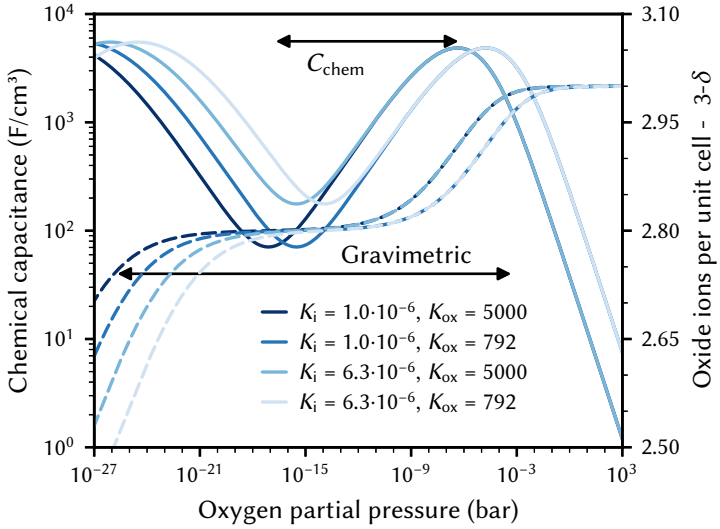

Figure 2.14: Calculated chemical capacitance for LSF (solid lines) for different equilibrium constants and corresponding oxygen stoichiometry (dashed lines), both based on the dilute defect model, see equation (2.21). A much narrower p_{O_2} span (only from capacitance maximum to capacitance minimum) is sufficient to obtain both equilibrium constants by chemical capacitance measurements, compared to thermogravimetric measurements (both steps in the oxide concentration are required). Arrows indicate typical ranges required for a fit analysis of C_{chem} or weight analysis.

2.4 Conclusion

Dense LSF thin film electrodes were prepared on YSZ electrolyte substrates and their chemical capacitance was measured by impedance spectroscopy in different atmospheres and with varying DC polarizations. These measurements revealed:

- The chemical capacitance solely depends on the oxygen chemical potential in the electrode film, independent of the source affecting this potential (atmospheric oxygen pressure or external DC voltage)
- The shape of the chemical capacitance versus oxygen chemical potential curve is in qualitative agreement with expectations from bulk defect chemical models and already indicates the relevant minority defects determining the chemical capacitance.
- For very small chemical capacitances, i.e. for moderately reducing conditions, an additional interfacial contribution to the capacitance in the range of 400 $\mu F\,cm^{-2}$ comes into play and can be attributed to the LSF|YSZ interface.
- The corrected volume-specific chemical capacitance of the thin films can be reasonably well approximated by a defect chemical model with dilute defects and thus mass action constants for the oxygen exchange reaction and the electron/hole formation can be determined.
- The temperature dependence of the determined defect chemical data revealed the enthalpy and entropy of the oxygen incorporation reaction and of the electron-hole formation.
- Oxygen incorporation enthalpies and entropies of the LSF films agree very well with literature data obtained on macroscopic samples. Electronic defect formation enthalpies and entropies, however, differ, leading to higher electronic defect concentrations in the thin films. Moreover, defect interactions between electron holes may play a role at high oxygen partial pressures, leading to deviations from C_{chem} values predicted by the dilute defect model.
- The measurements showed that bias and oxygen partial pressure dependent chemical capacitance measurements can be a powerful tool for analysis of the defect chemistry of thin films, and particularly to reveal details of the minority defects.

3 Experimental determination of reaction orders

The study presented in this chapter has been published as a scientific paper in "Chemistry of Materials".[69]

3.1 Introduction

Understanding the factors that limit the oxygen reduction or evolution is essential for the improvement of SOFC/SOEC electrode performance and the development of new electrode materials. Studying reaction rates of oxygen exchange and their dependence on the atmospheric oxygen pressure and electrode polarization can give valuable insights into the fundamental processes and the key parameters governing the corresponding electrode reaction and thus help in determining the rate limiting reaction step.[45,46,49,50,53,70,71]

In principle, studies varying the oxygen partial pressure as well as the electrode overpotential are thus highly attractive when aiming at mechanistic conclusions, e.g. at the rate limiting step or the involved ionic and electronic defects, see sketch in figure 3.1a. However, it complicates data analysis and interpretation that both measurement parameters influence the reaction rates in multiple ways. Firstly, the oxygen partial pressure affects the adsorbate species and—via the oxygen chemical potential in the electrode—the defect concentrations. Secondly, the electrode polarization does not simply translate to an electrostatic driving force at the decisive interface, as in the Butler-Volmer model of aqueous electrochemistry, but instead acts primarily upon the oxygen chemical potential in the electrode and thus on the defect concentrations.[2,50,60,72] Furthermore, oxygen partial pressure as well as overpotential may also affect the surface potential step. Hence, both experimentally accessible measurement parameters modify the reaction rates in multiple ways, and this convolution of several effects complicates the interpretation of oxygen partial pressure dependent current voltage curves. This is also discussed by Chueh et al., who approached the problem by simulating the reaction rates for different reaction mechanisms and comparing the partial derivatives with respect to oxygen partial pressure and overpotential.[49]

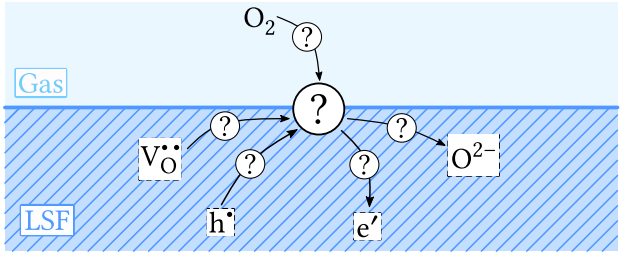

(a) Oxygen reduction

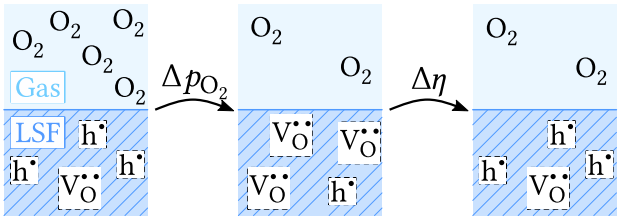

(b) Counterbalancing p_{O_2} by voltage

FIGURE 3.1: (a): Sketch of the oxygen reduction reaction on LSF. Gas phase oxygen (O_2) reacts to oxide ions (O^{2-}) by filling oxygen vacancies ($V_O^{\bullet\bullet}$). Whether electrons are supplied from the valence band (thus forming electron holes ($h^{\bullet}$)) or the conduction band (defect electrons (e')) is not known. (b): Changing the oxygen partial pressure p_{O_2} modifies the defect concentrations in the electrode. By counterbalancing these p_{O_2} induced changes with a different overpotential η, the oxygen partial pressure can be varied while keeping defect concentrations constant.

In this chapter, we introduce a simple but broadly applicable approach for analysing and interpreting partial pressure dependent current voltage data of the oxygen exchange reaction on a mixed conducting thin film electrode. The analysis is based on the rate equation model suggested in Ref. [72]. By properly combining overpotential and oxygen partial pressure changes, reaction rates can be studied for fixed defect chemistry in the electrode, despite varying oxygen partial pressure, see figure 3.1b. This procedure gives access to the true reaction orders of the oxygen release and incorporation reactions with respect to the relevant adsorbate species (determined by the gas phase), and the defect species in the solid phase. The novel approach is exemplified for LSF thin film electrodes on an yttria stabilized zirconia electrolyte and reveals important mechanistic information on the decisive defect species for oxygen evolution and oxygen incorporation.

3.2 Experimental

Double side polished yttria stabilized zirconia (100) single crystals (Crystec) ($5 \times 5 \times 1\,mm^3$) were used as electrolyte substrates. A reference electrode was produced by brushing a LSF/Pt-paste mixture into a notch around the circumference of the substrate and sintering in air for 2 h at 850 °C. Platinum current collector grids of 30/5 µm mesh/strip width and 100 nm thickness were prepared on both sides of the substrates by lift-off lithography and magnetron sputter deposition (BAL-TEC MED 020) to ensure complete and homogeneous electrode polarization. Dense $La_{0.6}Sr_{0.4}FeO_{3-\delta}$ (LSF) thin film working electrodes were fabricated by pulsed laser deposition (PLD) on top of these current collectors. The PLD target was made from LSF powder (Sigma Aldrich) by cold isostatic pressing (150 MPa) and sintering in air (12 h, 1200 °C). Ablation was done at 600 °C substrate temperature and 0.04 mbar oxygen (Alphagaz, 99.995 %) using a KrF excimer laser (Complex Pro 201F, 248 nm) with laser pulses of 400 mJ at 5 Hz. The target to substrate distance was 6 cm. Porous $La_{0.6}Sr_{0.4}CoO_{3-\delta}$ (LSC) counter electrodes were made by PLD (400 mJ, 5 Hz, 6 cm) at 450 °C and 0.4 mbar oxygen.

Working and counter electrodes were contacted by clamping the sample between two platinum sheets, the reference electrode was contacted with platinum thread around the sample circumference. DC measurements were performed at 600 °C in different oxygen/nitrogen mixtures (2.5×10^{-4} to 1 bar oxygen), using a Novocontrol PotGal electrochemical test station and a Novocontrol Alpha frequency analyser in potentiostat mode. At each oxygen partial pressure, one cathodic bias sweep (0 mV to −600 mV to 0 mV) followed by one anodic bias sweep (0 mV to 600 mV to 0 mV) was performed in steps of 50 mV. Additionally, impedance spectra were measured in all O_2/N_2 mixtures (10^6 to 10^{-1} Hz, 10 mV rms without DC voltage). The total measurement time was about 30 min per atmosphere. Within these short time spans degradation of the LSF surface resistance was very small, in accordance with the almost identical currents found for the two branches of a bias sweep.

3.3 Results

First, impedance spectra without DC voltage were measured at oxygen partial pressures between 2.5×10^{-5} bar and 1 bar oxygen. The spectra show one dominant low frequency semicircle feature, and parts of an additional arc in the high frequency domain. These impedance spectra were fitted to an equivalent circuit consisting of a parallel R-CPE element in series with a resistance R_{Offset}. The constant phase element (CPE) was used to model an imperfect capacitor.[64] The measured spectra and the corresponding fit results are shown in section 3.A (table 3.2 and figure 3.11). Earlier studies revealed that the main arc of such spectra reflects the

oxygen exchange resistance at the electrode surface and that the across plane oxygen transport resistance in these or similar mixed conducting thin film electrodes is negligible.[11,13,20,24] Moreover, the electrode area above the Pt current collector grid was shown to be inactive for oxygen exchange.[13] The values obtained for resistances and capacitances were thus normalized to the active area (approx. 73 % of the total LSF area), yielding an oxygen exchange resistance of 13 $\Omega\,cm^2$ and a capacitance of 3.3 $mF\,cm^{-2}$ at 600 °C in 210 mbar oxygen. These values are comparable to data for oxygen surface exchange and chemical capacitance of similar LSF films reported in literature.[13] The resistive high frequency offset, R_{Offset}, of 60 to 70 Ω is attributed to the ionic resistance of the electrolyte and minor contributions from the wiring, i.e. the sum of all voltage losses not caused by the surface exchange reaction.

The resistance R_{Offset} is used to calculate the electrode overpotential η according to

$$\eta = U_{DC} - I_{DC} R_{Offset}\,, \tag{3.1}$$

where U_{DC} is the measured voltage between working and reference electrode and I_{DC} is the measured current through working and counter electrode. This overpotential acts as the driving force for the net oxygen incorporation or oxygen evolution at the LSF surface. After this first impedance characterization the partial pressure dependent DC polarization sweeps were performed.

Figure 3.2 shows a 3D plot of the entire experimental data set, i.e. the measured net current density j (normalized to the active electrode area, approx. 73 %) as a function of electrode overpotential and oxygen partial pressures from 0.25 mbar to 1 bar O_2, for an LSF thin film electrode at 600 °C. Projections of this data set to the j-η plane for selected oxygen partial pressures (i.e. current density vs. overpotential curves) are displayed in figure 3.3.

The highest overpotential values could be experimentally achieved in the cathodic regime and at low oxygen partial pressure, due to the high working electrode resistance and thus small relative electrolyte losses. At high oxygen partial pressure and in the anodic regime the working electrode resistance becomes low and thus the relative voltage drop in the electrolyte increases, leading to a smaller attainable overpotential range. A first obvious result is the absence of any strong p_{O_2} dependence of the j-η curves for oxygen partial pressures above 25 mbar, see figure 3.3b.

From the measured current density vs. overpotential and oxygen partial pressure data, projections to the j-p_{O_2} plane, i.e. current density vs. oxygen partial pressure curves at constant overpotentials, are accessible. However, since during these experiments only the DC voltage between working and reference electrode U_{DC} is controlled, the specific electrode overpotentials η differ for different oxygen partial pressures despite the same nominal DC voltage.

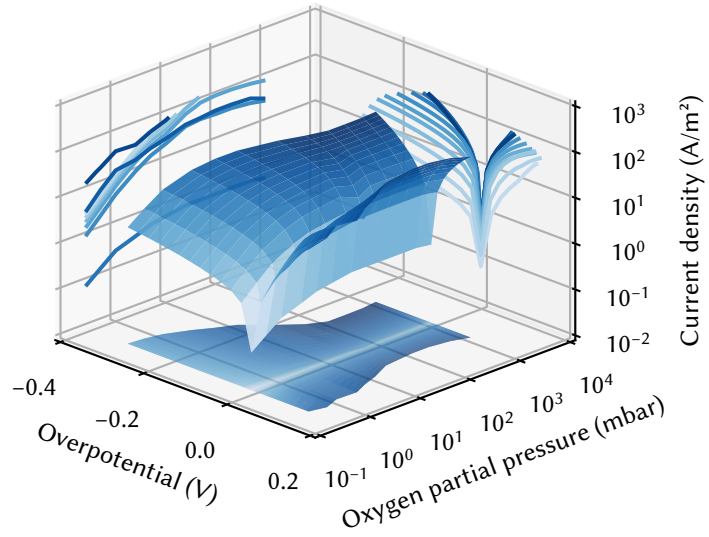

Figure 3.2: Measured net current density at 600 °C as a function of oxygen partial pressure and overpotential. Projections of this dataset to the j-p_{O_2} plane (i.e. current density vs. oxygen partial pressure at fixed overpotentials) and the j-η plane (i.e. current density vs. overpotential curves at p_{O_2}) are indicated on the vertical sides of the figure. The bottom shows a projection of the dataset to the η-pO_2 plane.

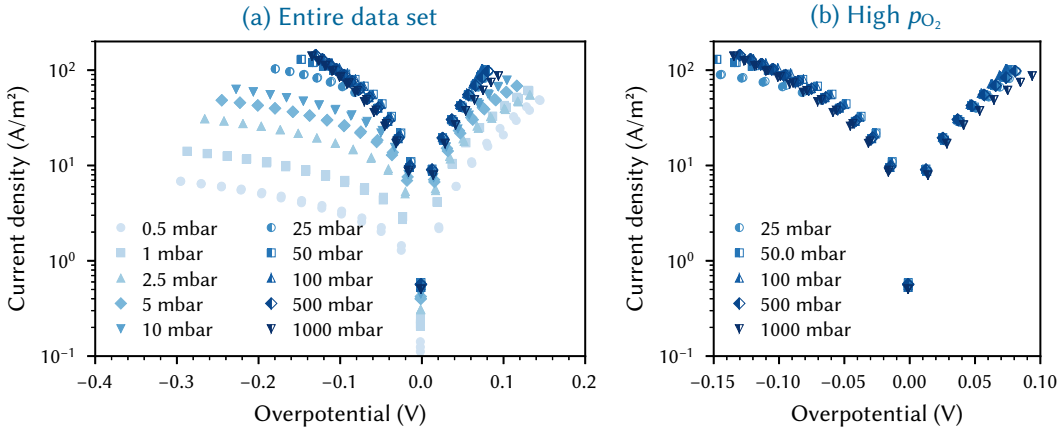

Figure 3.3: Current density versus overpotential curves of LSF thin film electrodes at 600 °C over the entire investigated p_{O_2} range (a) and in selected high partial pressures (b). Each η-j curve consists of one cathodic bias sweep (0 mV to −600 mV to 0 mV set voltage) and one anodic bias sweep (0 mV to 600 mV to 0 mV set voltage) measured consecutively.

Hence, these curves were obtained by linear interpolation of the current density vs. overpotential curves between the two closest measured data points. This point by point interpolation was necessary since simple analytical functions such as exponentials cannot describe the experimental data sufficiently. The resulting plots are shown in figure 3.4. Separating these data into high oxygen partial pressure (>10 mbar) and low oxygen partial pressure (<10 mbar), and into cathodic and anodic polarization yielded four different regimes:

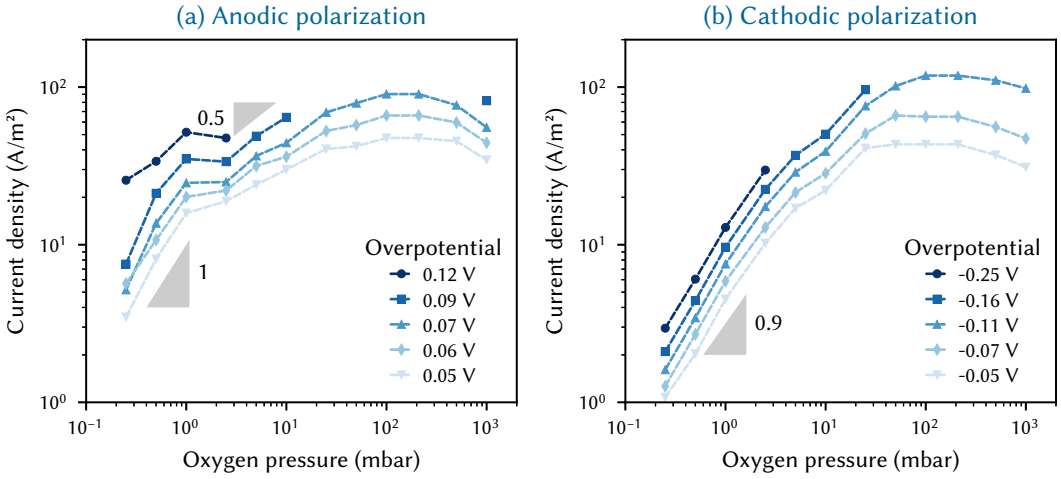

FIGURE 3.4: Current density vs. oxygen partial pressure for different anodic (a) and cathodic (b) overpotentials. Data were obtained from the measurement results shown in figure 3.3 by linear interpolation between the two nearest data points.

Under anodic polarization and at high oxygen partial pressures, the oxygen evolution exhibits only little oxygen partial pressure dependence. For the highest oxygen partial pressures (0.5 to 1 bar) the oxygen evolution rate shows even a slightly negative trend versus the oxygen partial pressure. At first glance, this part of the curve seems easy to understand, assuming oxygen in the gas either being irrelevant for oxygen evolution or even hindering it. However, below 10 mbar oxygen the oxygen release rate quite surprisingly decreases with decreasing oxygen partial pressure. Here, the empirical reaction order with respect to p_{O_2} is in the range of 0.5 to 1, see figure 3.4a, meaning that a higher product concentration, p_{O_2}, enhances the reaction rate of oxygen evolution.

Under cathodic polarization and at oxygen partial pressures below 10 mbar, the oxygen incorporation rates distinctly increase with increasing p_{O_2}, see figure 3.4b. This rate enhancing effect of oxygen seems intuitively understandable, and simple models of p_{O_2} dependent adsorbate concentrations suggest either a slope of 1 for molecular oxygen involved in the rate

limiting step or of 0.5 for atomic oxygen. However, here the empirical reaction order is close to 0.9. Moreover, above 10 mbar the reaction order with respect to gaseous oxygen surprisingly decreases to almost zero and even gets slightly negative above 0.2 bar.

Altogether it is obvious that empirical j-p_{O_2} curves might be very non-trivial and a straightforward interpretation is not possible. The same is true for the j-η data in figure 3.3, where a simple Tafel analysis (linear lines in the $\log(j)$ vs. η plots) fails for many curves. This is due to the non-trivial and largely non-electrostatic effects of the overpotential as discussed in the following.[50,72]

3.4 Data analysis and discussion

3.4.1 Rate equation and general approach

In an empirical analysis of the j-η and j-pO_2 curves in figure 3.3 and figure 3.4, one might assume that the anodic oxygen evolution current density j_a and the cathodic oxygen reduction current density j_c can be split into constant prefactors j_c^0, j_a^0 and voltage and partial pressure dependent factors:

$$j_c = j_c^0 \, f_c(\eta) \, {p_{O_2}}^{\nu_{c,emp}} \tag{3.2}$$

$$j_a = j_a^0 \, f_a(\eta) \, {p_{O_2}}^{\nu_{a,emp}} . \tag{3.3}$$

The total current density is $j = j_a - j_c$. $\nu_{a,emp}$ and $\nu_{c,emp}$ are the empirical reaction orders with respect to gaseous oxygen, f_a and f_c are functions of the overpotential η. For sufficiently anodic polarization, $j_a >> j_c$ is valid, and the anodic reaction order $\nu_{a,emp}$ can be extracted from the anodic branch of the j-p_{O_2} plots in figure 3.4. In the same way, $\nu_{c,emp}$ can be extracted from the cathodic branch. However, as already discussed above, the gaseous oxygen affects both the adsorbate species, and the defect concentrations in the electrode. Thus, there is no simple mechanistic meaning behind the empirical reaction orders.

In the following, a different approach is therefore introduced, which does not rely on the experimental parameters p_{O_2} and η, but instead considers the truly reacting local species (surface adsorbates and point defects in the solid electrode) and the local electrostatics at the decisive gas/solid interface (surface potential). A rate equation was suggested in Ref. [72] to deconvolve the effects of adsorbates and defects. An alternative approach was described by Chueh et al. and specified for different reaction mechanisms.[49] In section 3.B, a specific rate equation is deduced for an exemplary reaction mechanism of electrochemical oxygen surface exchange.

When generalizing this deviation for other possible mechanisms we get

$$j_c = j_c^0 {c_{D,c}}^{\nu_{D,c}} {p_{O_2}}^{\nu_{p,c}} \exp\left(\frac{\beta e \chi_0}{kT}\right) \exp\left(\frac{\beta e \Delta\chi}{kT}\right). \tag{3.4}$$

In equation (3.4) $c_{D,c}$ is the relevant defect species concentration and $\nu_{D,c}$ is the respective reaction order. If more than one defect has to be considered this factor has to be replaced by a product such as ${c_{D,1}}^{\nu_{D,1}} {c_{D,2}}^{\nu_{D,2}}$. $\nu_{p,c}$ is the true reaction order with respect to the oxygen partial pressure, p_{O_2}. In contrast to the empirical reaction order in equations (3.2) and (3.3), this "true" oxygen reaction order only involves the effect of gas phase oxygen via oxygen adsorbates, but not effects via p_{O_2} dependent defect concentrations in the electrode. The symbols χ_0 and $\Delta\chi$ represent the surface potential step in equilibrium and its change under current, respectively; $\Delta\chi$ might largely come from changes of charged adsorbates under current.[50] β is a factor that depends on the reaction mechanism. The prefactor j_c^0 may depend on the concentration of catalytically active sites, if those are not the defects already considered by $c_{D,c}$. Symbols k, T and e denote Boltzmann constant, temperature and elementary charge. In the same way, the oxygen evolution current density can be described by an equation, however with usually different relevant defect species and reaction orders.

The experimental parameter η acts on the defect concentrations c_D, but may also affect the surface potential (χ_0, $\Delta\chi$).[50,72] The experimentally given oxygen partial pressure, affects the adsorbate concentration and the oxygen chemical potential in the solid phase, and thus the defect concentrations. Furthermore, p_{O_2} may influence the surface potential via charged adsorbates. In the following, we simplify this very complex situation by assuming that, at least for low oxygen partial pressures, the surface potential step does not change much with voltage and p_{O_2}. XPS studies on LSF support this assumption.[15] Thus, p_{O_2} mainly affects rates by adsorbate concentrations and the electrode defect chemistry, while the overpotential acts mainly by changing the defect concentrations. We thus get a simplified relation from equation (3.4), with prefactor j_c^{0*} that includes the constant χ and $\Delta\chi$ terms:

$$j_c = j_c^{0*} {c_{D,c}}^{\nu_{D,c}} {p_{O_2}}^{\nu_{p,c}}. \tag{3.5}$$

Since the defect concentration depends on the oxygen chemical potential in the electrode μ_{O_2}, we may express $c_{D,c}$ by the relation $\acute{f}_c\left(\mu_{O_2}\right)$ and thus get:

$$j_c = j_c^{0*} \acute{f}_c\left(\mu_{O_2}\right) {p_{O_2}}^{\nu_{p,c}},. \tag{3.6}$$

This equation explicitly expresses that the cathodic current density is determined by gas adsorbates (via $p_{O_2}{}^{\nu_{p,c}}$) and by the defect chemistry (via $\acute{f}_c\left(\mu_{O_2}\right)$) in contrast to the mechanistically much less insightful equation (3.2).

Based on this model we can now approach a mechanistic interpretation of our experimental data, i.e. the current density as a function of oxygen partial pressure and overpotential. The main advantage of this analysis relies on the fact that the defect concentrations can be tuned independently by either oxygen partial pressure or overpotential. More specific, the defect concentrations are determined by the chemical potential of oxygen in the electrode μ_{O_2}, which depends on the experimental parameters p_{O_2} and η according to[2,57]

$$\mu_{O_2} = 4e\eta + kT \ln\left(\frac{p_{O_2}}{1\,\text{bar}}\right). \tag{3.7}$$

Here, the oxygen chemical potential is referenced to 1 bar oxygen ($\mu_{O_2} = 0$ for 1 bar and $\eta = 0\,\text{V}$). Hence, a certain defect chemical state can be established by different combinations of oxygen partial pressure and overpotential. By an appropriate choice of η, we can thus counterbalance any p_{O_2} change such that the oxygen chemical potential and thus the defect concentrations remain fixed.

In order to exploit the advantages of equation (3.6), we first have to transform our data set from $j\left(\eta, p_{O_2}\right)$ to $j\left(\mu_{O_2}, p_{O_2}\right)$ by using the relation in equation (3.7). Then, a two step analysis follows: First, we analyse the j-p_{O_2} dependency at fixed oxygen chemical potential and extract the true reaction order with respect to oxygen partial pressure. This true reaction order only involves the effect of adsorbed oxygen species and does not include any effect of defect concentrations. In terms of equations (3.5) and (3.6) we fix μ_{O_2}, and thereby c_D, and thus get ν_p. Second, from the j-μ_{O_2} curves at fixed oxygen partial pressures, we can extract the dependencies on the oxygen chemical potential (and thus on the defect chemistry) in the electrode, i.e. $\acute{f}_c\left(\mu_{O_2}\right)$ in equation (3.6). By comparing these dependencies to the Brouwer diagram of the electrode material (defect concentrations vs. oxygen chemical potential), we can get information on the relevant defect species. In the following, this approach is exemplified for the experimental LSF data shown above.

3.4.2 Analysis of LSF current-voltage curves

Recalculation of the data set

From the experiments, current density vs. overpotential curves for different oxygen partial pressures were obtained. This $j\left(\eta, p_{O_2}\right)$ data set was converted to current density vs. oxygen chemical potential data, $j\left(\mu_{O_2}, p_{O_2}\right)$, by equation (3.7). This is essentially a shift of the current

density vs. overpotential curves (figure 3.3) by the Nernst voltage term in equation (3.7). Figure 3.5 displays selected current density vs. oxygen chemical potential curves for the anodic and cathodic branch. The shape of these curves corresponds to the $\acute{f}_c\left(\mu_{O_2}\right)$ term in equation (3.6) and its anodic counterpart $\acute{f}_a\left(\mu_{O_2}\right)$.

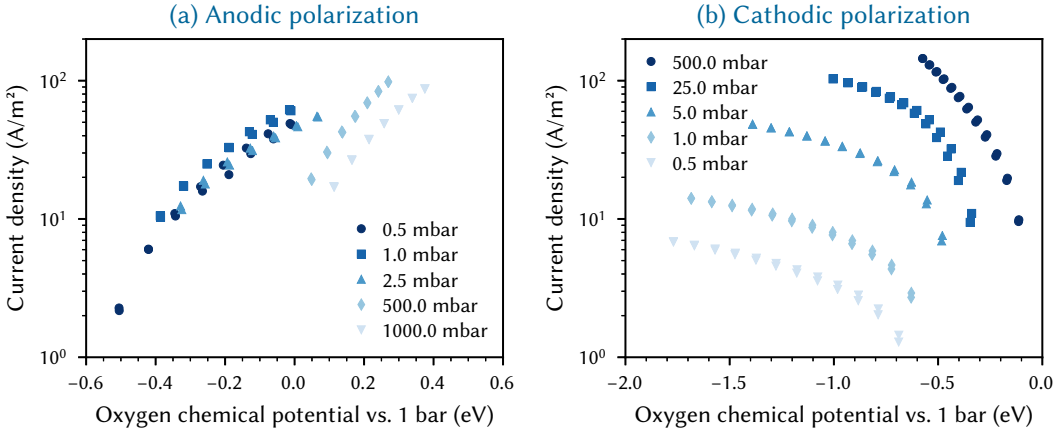

FIGURE 3.5: Current density vs. oxygen chemical potential (vs. 1 bar O_2) for anodic (a) and cathodic (b) polarization at 600 °C. Each curve consists of data from one bias sweep (0 mV to ±600 mV to 0 mV set voltage).

From this recalculated data set, the current density vs. oxygen partial pressure characteristics at constant oxygen chemical potentials were extracted in the same manner as described above for the j-η curves, i.e. by linear interpolation between the two closest data points. From the resulting plots we can get the partial pressure dependency, i.e. the ${p_{O_2}}^{\nu_p}$ factor in equation (3.6). Several current density vs. p_{O_2} curves are shown in figure 3.6. The number of data points on these curves strongly differs for different oxygen chemical potentials. This is simply due to the fact that some oxygen chemical potentials were only accessible in a limited p_{O_2} range in the experiment. For example, in the anodic regime high oxygen chemical potentials were only reached at high p_{O_2}. For low oxygen partial pressures, the overpotentials in the experiment were not sufficiently high to induce large shifts towards a high oxygen chemical potential. In the cathodic regime, on the other hand, the slightly negative oxygen chemical potential range with respect to the reference state at 1 bar was only accessible for high oxygen partial pressures. The resulting data set can again be divided into a high p_{O_2} regime and a low p_{O_2} regime for both anodic and cathodic branches. These are discussed below, based on the following defect chemical model for bulk LSF.

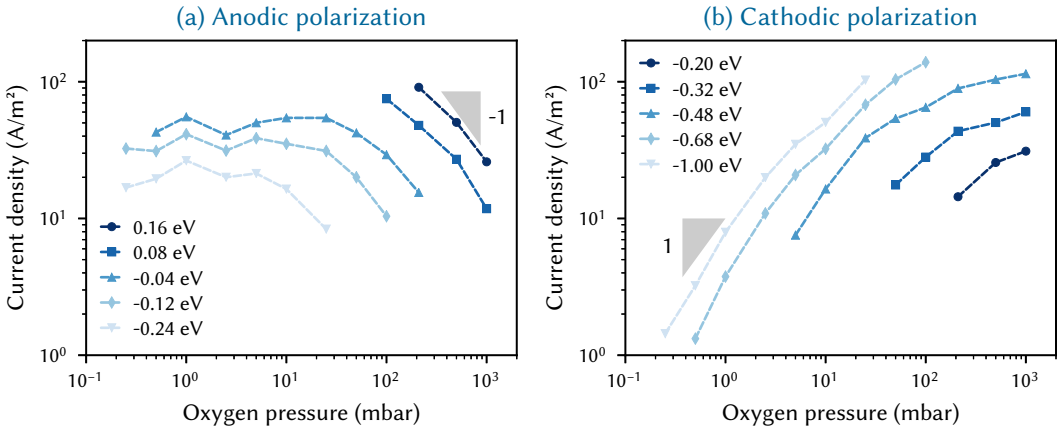

FIGURE 3.6: Current density vs. oxygen partial pressure curves for several oxygen chemical potentials under anodic (a) and cathodic (b) polarization, extracted from the data in figure 3.5 by linear interpolation. The oxygen chemical potential, and thus the defect chemical state in the electrode, is constant along each curve. Thus, only the adsorbate concentrations change with oxygen partial pressure.

Defect model of bulk LSF

A quantitative bulk defect model of LSF is described in Refs. [8, 35]. The main defect species in this model are oxygen vacancies $V_O^{\bullet\bullet}$, electrons e' and electron holes $h^{\bullet}$. The reaction enthalpies and entropies for electron/hole pair formation ($2\,Fe_{Fe}^{\times} \rightleftharpoons Fe_{Fe}^{\bullet} + Fe_{Fe}'$) and oxygen incorporation reaction ($V_O^{\bullet\bullet} + 1/2\,O_2 + 2\,Fe_{Fe}^{\times} \rightleftharpoons O_O^{\times} + 2\,Fe_{Fe}^{\bullet}$) were determined via thermogravimetry and coulometric titration, see table 3.1.[14] From these data, the defect concentrations can be calculated and figure 3.7 shows the corresponding Brouwer diagram for LSF at 600 °C.

TABLE 3.1: Thermodynamic defect data of LSF.[14]

	ΔH (kJ mol^{-1})	ΔS (J mol^{-1} K)
Oxygen incorporation	-95.62	-54.27
Electron/hole formation	95.75	-21.63

Mechanistic analysis of anodic oxygen evolution

For low oxygen partial pressures and anodic polarization, the current density vs. oxygen chemical potential curves approximately coincide, see figure 3.5a, i.e. the true reaction order with respect to gaseous oxygen $\nu_{p,a}$ is almost zero, see figure 3.6a. Thus, the surprisingly positive empirical reaction order mentioned above, see figures 3.3 and 3.4, suggesting an acceleration

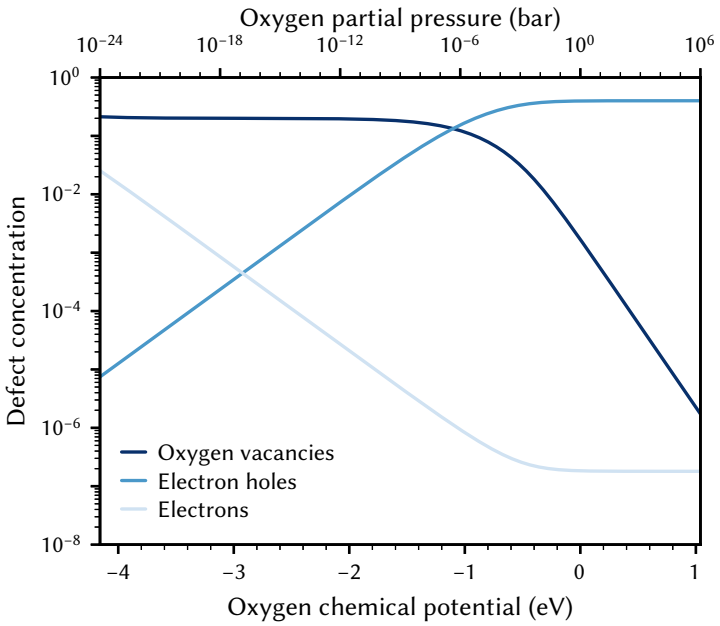

FIGURE 3.7: LSF Brouwer diagram at 600 °C, calculated from literature data on bulk LSF.[14]

of the oxygen evolution reaction by gas molecules, is only an indirect effect due to the dependence of defect concentrations on p_{O_2}. Therefore, this phenomenon vanishes when keeping the defect chemistry (μ_{O_2}) constant. As a first result of our analysis we can thus conclude that for low oxygen partial pressures the true reaction order of gas molecules is close to zero.

The dependency of the current density on the oxygen chemical potential at fixed p_{O_2} (figure 3.5a), on the other hand, reflects $\acute{f}_a\left(\mu_{O_2}\right)$ and thus the dependency on the defect concentrations, i.e. ${c_D}^{\nu_D}$ in equation (3.5). These curves can be compared with the known relation between bulk defect concentrations and the oxygen chemical potential calculated from bulk data,[14] see Brouwer diagram in figure 4.1. Only electron holes exhibit a similar shape as the current density vs. oxygen chemical potential curves, suggesting that electron holes are the defect species determining the oxygen evolution rate.

For a more detailed analysis, we may use the current density at a given oxygen chemical potential and plot it versus the electron hole concentration calculated from the defect model for this oxygen chemical potential. The resulting double logarithmic plot shows a clear correlation between electron holes and the oxygen evolution current density, see figure 3.8a. The relation does not follow a simple power law, and additionally shows an extremely high slope (roughly 20 on average), i.e. a very strong dependency of the oxygen evolution current density on the hole concentration. However, we have to keep in mind, that the calculated bulk defect

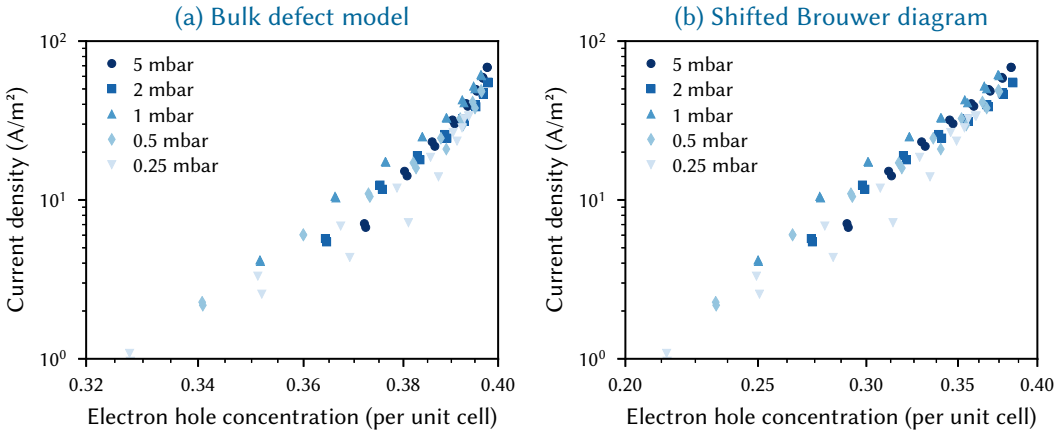

FIGURE 3.8: Oxygen evolution current density vs. electron hole concentration. Hole concentrations were calculated based on the bulk defect model for LSF[14] (a) and from a Brouwer diagram shifted to higher oxygen chemical potential by 320 meV (b).

concentrations can severely differ from the local defect concentration at the surface. Simulations of the related perovskite material $LaCoO_3$ revealed a lower formation energy of oxygen vacancies at the surface, resulting in a more reduced state of the surface, and thus less electron holes, compared with the bulk.[73]

Owing to the lack of experimental data on the exact defect chemical state of our LSF surfaces, we tried to consider the effect of such a reduced surface by simply shifting the bulk Brouwer diagram towards higher oxygen chemical potentials. We then used the shifted Brouwer diagrams to calculate the defect concentrations for the respective oxygen chemical potentials. For a μ_{O_2} shift of 320 meV, i.e. a shift on the oxygen partial pressure axis by a factor of 70, the resulting oxygen evolution current density versus electron hole concentration plot (figure 3.8b) shows a linear correlation between electron hole concentration and oxygen evolution rate in the double logarithmic plot. Thus a simple power law relation exists, and a fit revealed an exponent of 6.7. Owing to the given assumptions and uncertainties, we do not dare to interpret the exact value of 6.7 mechanistically, but such a high value strongly suggests involvement of multiple electron holes in the mechanism of oxygen evolution. However, these electron holes do not necessarily enter the rate determining step as reacting species, but may also be included in preceding equilibrium steps.

In the anodic regime above 10 mbar p_{O_2} (figure 3.6a), the current density decreases with higher oxygen partial pressure, i.e. the true reaction order becomes negative. Since the defect chemistry is fixed, this effect has to be caused by gas adsorbate species. Hence, the only weak empirical dependence of the oxygen evolution rate on oxygen partial pressure (see figure 3.4a)

turns out to be just an incidental counterbalancing between the true, negative reaction order of p_{O_2}, and an accelerating effect due to the oxygen partial pressure dependent defect concentrations. Possible explanations for this negative true reaction order are a blockage of catalytically active sites for oxygen evolution on the surface by gas adsorbates, or a change in the surface potential step due to higher adsorbate coverages (only considered in equation (3.4)). A gas diffusion limitation should still lead to an increase of the current with increasing p_{O_2}. The defect chemical dependence of the current density, given by $\acute{f}_a\left(\mu_{O_2}\right)$, again suggests an important role of electron holes, but a more quantitative analysis as for low p_{O_2} is beyond the scope of our study.

Mechanistic analysis of cathodic oxygen reduction

Under cathodic polarization and low p_{O_2}, the current vs. oxygen partial pressure plots at constant μ_{O_2} (see figure 3.6b) reveal a clear dependence of the oxygen reduction current on the oxygen partial pressure, with a true reaction order close to 1. This true reaction order again reflects the pure effects of gas phase and adsorbate species and does not include any influence of defect chemistry. A true reaction order of 1 with respect to molecular oxygen suggests either molecular oxygen adsorbates of unknown charge being involved in the rate determining step or gas diffusion/adsorption as rate limiting step. The empirical reaction order of 0.9 found in our first analysis, see figure 3.4, is thus a convolution of the true reaction order of 1 and a slightly negative indirect effect of p_{O_2} via an impact of p_{O_2} on defect concentrations. This negative impact of the oxygen partial pressure on the defect chemistry already hints at oxygen vacancies as the relevant defects, since their concentration decreases with increasing p_{O_2}.

At high oxygen partial pressure and cathodic polarization (figure 3.6b), the true reaction order with respect to oxygen gas continually decreases, and reaches almost zero. This is again a true gas species/adsorbate effect and not a result of changes in defect concentrations. It means that more gas species do no longer accelerate the reduction rate via more adsorbates. The onset of this decrease in reaction order is at around 10 to 20 mbar oxygen partial pressure. Interestingly, this is exactly the pressure range where the oxygen partial pressure begins to have a negative effect on the anodic reaction rate, see figure 3.6a. Moreover, in the same oxygen partial pressure range the p_{O_2} dependence of the polarization resistance from impedance spectroscopy changes its sign, see figure 3.11 in section 3.A.

A common mechanism behind these three observations is likely. As already mentioned above, the saturation of catalytically active sites with oxygen adsorbate species may be responsible. Another possible reason for the onset of deviations is a change in the surface potential, due to higher surface coverage of charged adsorbates for higher oxygen partial pressure.

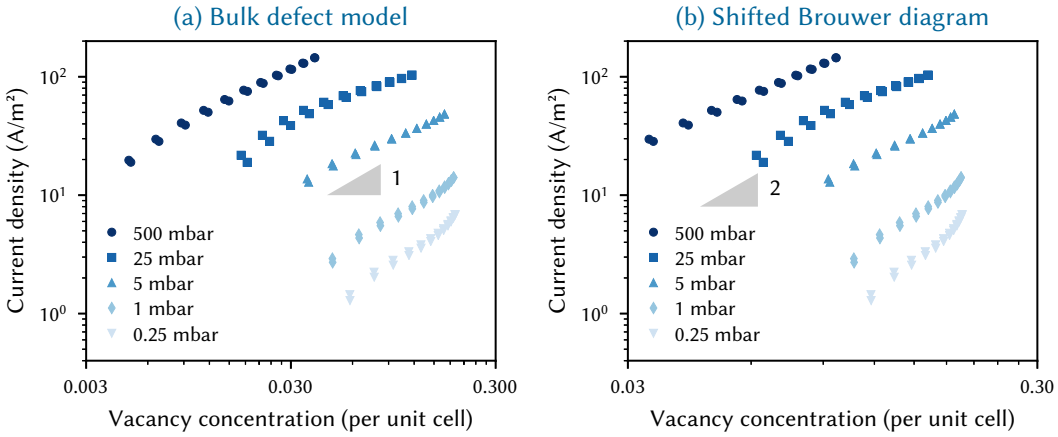

FIGURE 3.9: Oxygen incorporation current density vs. oxygen vacancy concentration. Vacancy concentrations were calculated based on the bulk defect model for LSF[14] (a) and from a Brouwer diagram shifted to higher oxygen chemical potential by 320 meV (b).

The current density vs. oxygen chemical potential curves at constant p_{O_2} reflect the influence of the defect chemistry on oxygen reduction, see figure 3.5b. When comparing the shapes of the current density vs. oxygen chemical potential curves and the defect concentrations in the Brouwer diagram (see figure 4.1), we find a good agreement for oxygen vacancies. Therefore, we assume that oxygen vacancies are the limiting defect species for the oxygen incorporation. Oxygen vacancies are also suggested in literature as the rate limiting defect species for oxygen incorporation on related perovskites of the (La,Sr)MnO_3, (La,Sr)(Co,Fe)O_3 and (Ba,Sr)(Co,Fe)O_3 families.[43,52,74]

The current density as a function of calculated bulk oxygen vacancy concentration is shown in figure figure 3.9a for oxygen partial pressures of the entire investigated pressure range. To a first approximation, these curves exhibit close to linear relations between oxygen vacancy concentration and oxygen reduction current density, indicating a reaction order close to one with respect to oxygen vacancies. For high concentrations of oxygen vacancies, however, the current densities deviate from the linear relationship. As these deviations occur where the overpotential was highest, a sight surface potential change with bias is a possible explanation.

Moreover, we again have to emphasize the possible difference between bulk and surface defect chemistry. In accordance with the bulk-to-surface difference introduced above for electron holes and anodic current densities, we shifted the bulk Brouwer diagram by 320 meV towards higher oxygen chemical potentials. Then we calculated the oxygen vacancy concentration of the more reduced surface for each experimental oxygen chemical potential and the resulting plot is shown in figure 3.9b. The current density vs. oxygen vacancy concentration curves

again show an approximate power law relation, but with a higher exponent in the range of 2. This dependence of the defect related reaction order on the shift due to a more reduced surface shows that a final elucidation of the mechanism is problematic without a detailed knowledge of the surface defect concentrations. Still, to the best of our knowledge, the plot in figure 3.9 gives the first semi-quantitative relation between the oxygen reduction rate and the oxygen vacancy concentration determined for one and the same material. So far, similar plots (e.g. surface exchange coefficient vs. vacancy concentration) were published only for different materials or doping levels.[43,74]

We may also consider the consistency of the main qualitative and semi-quantitative conclusions drawn so far and thus can speculate about the reaction mechanism. First, it is consistent that all the deduced reaction orders are comparatively high: for oxygen vacancies involved in oxygen reduction it is possibly two, for molecular oxygen in the gas phase it is one, and for electron holes during oxygen evolution it is very large; a value of more than six is found, which means that it is probably at least in the range of three to four or even larger. Finally, all reaction orders have to be in agreement with the thermodynamic mass action law, given by

$$K = \frac{{c_{\mathrm{Ox}}}^2 {c_{\mathrm{h}}}^4}{{c_{\mathrm{V}}}^2 {c_{\mathrm{Fe}}}^4 p_{\mathrm{O_2}}} . \tag{3.8}$$

We can conclude that the measured reaction orders are indeed in acceptable agreement with this equation, which supports the consistency of our analysis. Please note: High reaction orders do not mean that many particles or defect species have to be involved in the rate determining step. Rather, also species in fast preceding steps enter the rate equation. The reaction orders of gas (1) and oxygen vacancies (possibly 2) would be in accordance with incorporation of an adsorbed oxygen molecule into two neighbouring vacancies as rate limiting step (probably accompanied by further reduction). However, only further studies may reveal the validity of this hypothesis.

Altogether, this example demonstrates that the analysis of measured $j\left(\eta, p_{\mathrm{O_2}}\right)$ data in terms of $j\left(\mu_{\mathrm{O_2}}, p_{\mathrm{O_2}}\right)$ allows important mechanistic conclusions. In our specific case of LSF electrodes, most effects can be explained by changes in either adsorbate or defect concentrations when varying overpotential and oxygen partial pressure. Accordingly, the measured non-linearity of current density vs. overpotential curves is largely the result of voltage induced defect concentration changes. This is in strong contrast to a charge transfer limited kinetics at aqueous/metal interfaces described by Butler-Volmer's equation. There, electrostatic potential changes rather than concentration changes cause the non-linearity of the often exponential current voltage-curves. Accordingly, analysis of solid state electrochemical measurements cannot simply rely on established concepts from aqueous electrochemistry, but has to implement novel analysis

tools. The concept introduced in this paper may serve as the basis for future data analysis of similar experiments. It is not only applicable to other mixed conducting electrodes, but also for investigating other electrochemical reactions such as water splitting or CO_2 reduction.

3.5 Conclusion

A simple empirical analysis of p_{O_2} and overpotential dependent oxygen exchange currents in terms of reaction orders may be highly misleading in mechanistic discussions. Current-overpotential curves of dense LSF thin films, for example, yield surprising results, such as an apparent reaction order of zero with respect to the oxygen partial pressure for oxygen reduction in high p_{O_2} or acceleration of oxygen evolution by increasing p_{O_2}. For the analysis and mechanistic interpretation of such or similar experiments we propose a novel approach. In a first step, the oxygen chemical potential in the electrode is kept constant, while analysing the effect of the oxygen partial pressure on the oxygen evolution or incorporation current. A second step considers the dependence of these currents on the defect chemical state, defined by the oxygen chemical potential. The defect chemical state is varied by the overpotential at constant oxygen partial pressure. In this manner, the effects of the experimental parameters oxygen partial pressure and electrode overpotential can be deconvolved, and the true dependencies of the oxygen reduction and evolution currents on the concentration of gas phase or adsorbate species and on the point defect concentrations can be obtained.

This way of analysis can become a powerful tool when aiming at a better mechanistic understanding of oxygen exchange reactions, as exemplified for LSF. For the oxygen evolution on LSF we found strong indication for a limitation by the electron hole concentration. Oxygen gas species or adsorbates had no effect at low p_{O_2}, and even slowed the oxygen evolution reaction at higher oxygen pressures. For the oxygen incorporation, a linear dependence of the oxygen reduction current on p_{O_2} via gas adsorbates was found for p_{O_2} up to 10 mbar. This indicates that a molecular oxygen species is involved in the rate determining step. Additionally, a clear correlation between oxygen vacancy concentration and reaction rate could be deduced. Such a correlation was already hypothesized in literature from measurement on different materials, but here experimental evidence is given for one and the same material. This strongly suggests oxygen vacancies as the rate limiting defect species for oxygen reduction. Non-linearities of the current voltage curves seem to be largely the result of voltage induced changes in defect concentrations, rather than due to electrostatic effects. To finally clarify the exact reaction mechanism on LSF a more detailed investigation of the defect chemistry of the perovskite surface is essential.

Appendix 3.A Impedance spectroscopy

Impedance spectra were measured at oxygen partial pressures from 2.5×10^{-4} to 1 bar to determine the electrolyte resistance R_{offset}. Figure 3.10 displays the impedance spectra and the corresponding fits to the equivalent circuit shown in the inset. A CPE element with impedance $Z_{\text{CPE}} = -i(\omega T)^{-P}$ was used to model an imperfect capacitance. The fit results are listed in table 3.2 and the polarization resistance is also plotted in figure 3.11 versus the oxygen partial pressure. At low p_{O_2} the data can be fit to a power law with an exponent of -0.73. Above 20 mbar the polarization resistance increases with p_{O_2}. This is consistent with the bend found for both anodic and cathodic current voltage curves in the same pressure region.

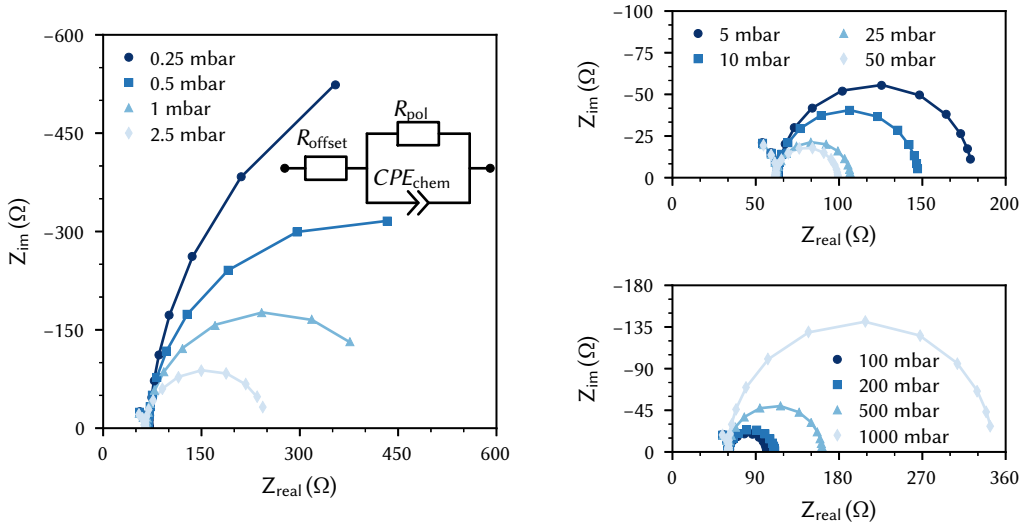

Figure 3.10: Impedance spectra (1 MHz to 100 mHz, 5 points per decade) measured between an LSF thin film electrode and the reference electrode at 600 °C in various oxygen partial pressures. Symbols are measured data, lines are fits to the equivalent circuit shown in the inset. Only the low frequency semicircles/arcs were included in the fits.

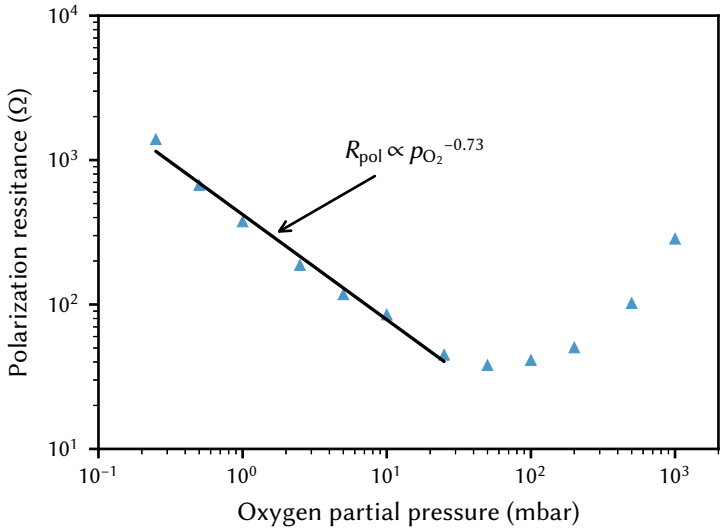

FIGURE 3.11: Polarization resistance of a LSF film at 600 °C versus oxygen partial pressure (symbols) and fit to power law(line).

TABLE 3.2: Fit results for impedance spectra in different atmospheres between 2.5×10^{-4} bar and 1 bar oxygen. Only the low frequency semicircle/arc was fitted.

p_{O_2} (bar)	R_{offset} (Ω)	R_{pol}(Ω)	$CPE_{chem} - T$(mF$^{1/P}$ s$^{1-1/P}$)	$CPE_{chem} - P$
2.5×10^{-4}	69.68 ± 0.11	1395.00 ± 11.47	2.317 ± 0.004	0.965 ± 0.001
5.0×10^{-4}	68.14 ± 0.06	671.50 ± 1.75	2.129 ± 0.003	0.964 ± 0.001
1.0×10^{-3}	65.79 ± 0.10	375.50 ± 1.15	1.824 ± 0.005	0.962 ± 0.001
2.5×10^{-3}	63.65 ± 0.10	187.50 ± 0.52	1.534 ± 0.006	0.963 ± 0.002
5.0×10^{-3}	63.04 ± 0.08	117.60 ± 0.21	1.343 ± 0.005	0.966 ± 0.001
1.0×10^{-2}	62.67 ± 0.04	85.16 ± 0.11	1.229 ± 0.004	0.969 ± 0.001
2.5×10^{-2}	62.15 ± 0.04	44.89 ± 0.06	1.054 ± 0.004	0.969 ± 0.001
5.0×10^{-2}	61.35 ± 0.02	38.04 ± 0.03	0.944 ± 0.003	0.969 ± 0.001
1.0×10^{-1}	60.53 ± 0.01	41.22 ± 0.03	0.808 ± 0.002	0.971 ± 0.001
2.0×10^{-1}	59.97 ± 0.03	50.38 ± 0.06	0.671 ± 0.003	0.976 ± 0.001
5.0×10^{-1}	59.72 ± 0.06	102.30 ± 0.15	0.575 ± 0.003	0.985 ± 0.001
1.0	60.36 ± 0.09	285.30 ± 0.41	0.547 ± 0.002	0.991 ± 0.001

Appendix 3.B Derivation of the rate equation

Charge transfer at aqueous electrolyte|electrode interfaces is frequently studied and detailed models have been established, describing the corresponding current-voltage characteristics according to Butler-Volmer's equation.[75,76]

$$j = j_0 \left(e^{\frac{\alpha |z| e\eta}{kT}} - e^{\frac{(\alpha-1)|z|e\eta}{kT}} \right). \tag{3.9}$$

Here, j denotes the net current density, j_0 is the exchange current density and includes the reactant concentrations, η is the overpotential, α represents the symmetry factor — for electronic transfer it is often close to 0.5 — and z is the charge number of the transferred species.

Electrochemical reactions at mixed conducting oxide electrode|gas interfaces, however, differ from aqueous reactions in several respects, making the analysis in terms of equation (3.9) unsuitable. First, the applied overpotential changes the oxygen chemical potential in the electrode bulk and thus modifies the concentration of point defects, i.e. the reacting species. Second, despite the possibly existing electrostatic potential difference $\chi = \varphi_{\mathrm{ode}} - \varphi_{\mathrm{ads}}$ between the electrode bulk (φ_{ode}) and the adsorbate layer (φ_{ads}), an applied overpotential does not directly translate to a change of this surface potential. If χ is caused by charged adsorbates, any overpotential driven change of this surface potential is correlated with a change in adsorbate concentration, and the resulting $\chi - \eta$ relation can become quite non-trivial.[50] Owing to these differences, a modified approach is required to describe the current-voltage characteristics of electrochemical reactions at solid electrode|gas interfaces. In the following we deduce such a model, i.e. a rate equation, for an exemplary mechanism and this can then be generalized. This mechanism is not necessarily the most realistic one, rather it is chosen for the sake of clarity.

Let us assume that the reaction consists of a reductive adsorption of molecular oxygen to form adsorbed $O_{2(ad)}^{-}$ (3.10), followed by dissociative incorporation into the electrode (3.11) and reduction to oxide ions (3.12), and let (3.10) and (3.12) be sufficiently fast compared to (3.11), such that (3.11) is the rate determining step (rds).

$$O_2 + \rightleftharpoons O_{2(ad)}^{-} + h^{\bullet} \tag{3.10}$$

$$O_{2(ad)}^{-} + 2V_O^{\bullet\bullet} \overset{\text{rds}}{\rightleftharpoons} O_O^{\bullet} + O_O^{\bullet\bullet} \tag{3.11}$$

$$O_O^{\bullet} + O_O^{\bullet\bullet} \rightleftharpoons 2O_O^{\times} + 3h^{\bullet} \tag{3.12}$$

Steps (3.10) and (3.12) include holes ($h^{\bullet}$) in the valence band but could also be formulated with electrons (e') from the conduction band, due to equilibrium of equation (3.10) and electron hole formation. The reaction rates of the rate limiting forward ($\vec{r}$) and backward ($\overleftarrow{r}$) ion transfers

are then given by

$$\vec{r} = \vec{k}\,\theta_{\mathrm{m}}^{-} {c_{\mathrm{V}}}^2 \tag{3.13}$$

$$\overleftarrow{r} = \overleftarrow{k}\, c_{\mathrm{Op}} c_{\mathrm{Opp}} \tag{3.14}$$

with the surface potential dependent rate constants $\vec{k}$ and $\overleftarrow{k}$, the normalized reactant concentrations of vacancies (c_{V}) and onefold (c_{Op}) or twofold (c_{Opp}) positive charged oxygen and the surface coverage with adsorbed superoxide (θ_{m}^{-}). The net reaction rate r is the difference between forward and backward reaction rates. Owing to equilibrium of the fast steps (equations (3.10) and (3.12)) the electrochemical potentials $\tilde{\mu}$ of all species are related by

$$\tilde{\mu}_{\mathrm{O}_{2(\mathrm{ad})}^{-}} + \tilde{\mu}_{\mathrm{h}^{\bullet}} = \mu_{\mathrm{O}_2} \tag{3.15}$$

$$2\tilde{\mu}_{\mathrm{O}^{2-}} + 3\tilde{\mu}_{\mathrm{h}^{\bullet}} = \tilde{\mu}_{\mathrm{O}_{\mathrm{O}}^{\bullet\bullet}} + \tilde{\mu}_{\mathrm{O}_{\mathrm{O}}^{\bullet}}\,. \tag{3.16}$$

Assuming $\tilde{\mu}_{\mathrm{i}} = \mu_{\mathrm{i}}^{0} + kT \ln c_{\mathrm{i}} + z_{\mathrm{i}} e \varphi_{\mathrm{i}}$, yields

$$\theta_{\mathrm{m}}^{-} = \frac{p_{\mathrm{O}_2}}{c_{\mathrm{h}}} \exp\left(\frac{\mu_{\mathrm{O}_2}^{0} - \mu_{\mathrm{h}^{\bullet}}^{0} - \mu_{\mathrm{O}_{2(\mathrm{ad})}^{-}}^{0}}{kT} + \frac{-z_{\mathrm{O}_{2(\mathrm{ad})}^{-}} e\varphi_{\mathrm{ads}} - z_{\mathrm{h}^{\bullet}} e\varphi_{\mathrm{ode}}}{kT} \right) = \frac{p_{\mathrm{O}_2}}{c_{\mathrm{h}}} K_1 \exp\left(-\frac{e\chi}{kT}\right) \tag{3.17}$$

$$c_{\mathrm{Op}} c_{\mathrm{Opp}} = {c_{\mathrm{h}}}^3 {c_{\mathrm{Ox}}}^2 \exp\left(\frac{2\mu_{\mathrm{O}_{\mathrm{O}}^{\times}}^{0} + 3\mu_{\mathrm{h}^{\bullet}}^{0} - \mu_{\mathrm{O}_{\mathrm{O}}^{\bullet}}^{0} - \mu_{\mathrm{O}_{\mathrm{O}}^{\bullet\bullet}}^{0}}{kT} \right) = {c_{\mathrm{h}}}^3 {c_{\mathrm{Ox}}}^2 K_3\,. \tag{3.18}$$

Here, $\chi = \varphi_{\mathrm{ode}} - \varphi_{\mathrm{ads}}$ is the electrostatic potential difference between electrode bulk and adsorbate layer, μ_{i}^{0} is the standard chemical potential and z_{i} is the charge number of species i ($z_{\mathrm{O}_{2(\mathrm{ad})}^{-}} = -1$ and $z_{\mathrm{h}^{\bullet}} = 1$). K_1 and K_3 are the purely chemical equilibrium constants of the preceding and succeeding equilibria without the factor due to the equilibrium surface potential. Combining equations (3.13), (3.14), (3.17) and (3.18) yields

$$\vec{r} = \vec{k} \frac{p_{\mathrm{O}_2} {c_{\mathrm{V}}}^2}{c_{\mathrm{h}}} K_1 \exp\left(-\frac{e\chi}{kT}\right) \tag{3.19}$$

$$\overleftarrow{r} = \overleftarrow{k} {c_{\mathrm{h}}}^3 {c_{\mathrm{Ox}}}^2 K_3 \tag{3.20}$$

The rate determining transfer of $\mathrm{O}_{2(\mathrm{ad})}^{-}$ from the adsorbate layer to the electrode bulk can be considered a jump of the $\mathrm{O}_{2(\mathrm{ad})}^{-}$ ion over a spatial energy barrier, where initial and final state are at different electrostatic potentials φ_{ads} and φ_{ode}, respectively.[77] The activation barrier for this ion jump consists of a purely chemical term ($\vec{E}_{\mathrm{a,c}}^{\mathrm{eq}}$ and $\overleftarrow{E}_{\mathrm{a,c}}^{\mathrm{eq}}$) and an additional component due to the potential difference between the two phases ($\alpha z_{\mathrm{O}_{2(\mathrm{ad})}^{-}} e\chi$ and $-(1-\alpha)\, z_{\mathrm{O}_{2(\mathrm{ad})}^{-}} e\chi$). The surface potential $\chi = \chi_0 + \Delta\chi$ includes the equilibrium surface potential χ_0 and its deviation

under current $\Delta\chi$; α reflects the symmetry of the energy barrier, see figure 3.12. Thus, we get

$$\vec{k} = \overrightarrow{k^0} \exp\left(-\frac{\overrightarrow{E_{a,c}^{eq}}}{kT}\right) \exp\left(\frac{\alpha e\chi}{kT}\right) \tag{3.21}$$

$$\overleftarrow{k} = \overleftarrow{k^0} \exp\left(-\frac{\overleftarrow{E_{a,c}^{eq}}}{kT}\right) \exp\left(-\frac{(1-\alpha)\, e\chi}{kT}\right). \tag{3.22}$$

with the pre-exponential factors $\overrightarrow{k^0}$ and $\overleftarrow{k^0}$ of the forward and backward ion transfer. As sketched in figure 3.12, the change in surface potential upon current $\Delta\chi = \chi - \chi_0$ modifies the equilibrium activation barriers by $\alpha z_{O^-_{2(ad)}} e\Delta\chi$ and $-(1-\alpha)\, z_{O^-_{2(ad)}} e\Delta\chi$ for the forward and backward reaction, respectively; a possible χ dependence of α is neglected. Combining equations (3.19) to (3.22) leads to

$$\vec{r} = \overrightarrow{k^0} \exp\left(-\frac{\overrightarrow{E_{a,c}^{eq}}}{kT}\right) \exp\left(\frac{\alpha e\chi_0}{kT}\right) \exp\left(\frac{\alpha e\Delta\chi}{kT}\right) K_1 \frac{p_{O_2} {c_V}^2}{c_h} \exp\left(-\frac{e\left(\chi_0 + \Delta\chi\right)}{kT}\right) \tag{3.23}$$

$$\overleftarrow{r} = \overleftarrow{k^0} \exp\left(-\frac{\overleftarrow{E_{a,c}^{eq}}}{kT}\right) \exp\left(-\frac{(1-\alpha)\, e\chi_0}{kT}\right) \exp\left(-\frac{(1-\alpha)\, e\Delta\chi}{kT}\right) K_3 {c_h}^3 {c_{Ox}}^2 . \tag{3.24}$$

Thus, we get

$$\vec{r} = \overrightarrow{r^0} p_{O_2} \frac{{c_V}^2}{c_h} \exp\left(\frac{(\alpha-1)\, e\chi_0}{kT}\right) \exp\left(\frac{(\alpha-1)\, e\Delta\chi}{kT}\right) \tag{3.25}$$

$$\overleftarrow{r} = \overleftarrow{r^0} {c_h}^3 {c_{Ox}}^2 \exp\left(\frac{(\alpha-1)\, e\chi_0}{kT}\right) \exp\left(\frac{(\alpha-1)\, e\Delta\chi}{kT}\right) \tag{3.26}$$

with $\overrightarrow{r^0} = K_1 \overrightarrow{k^0} \exp\left(-\frac{\overrightarrow{E_{a,c}^{eq}}}{kT}\right)$ and $\overleftarrow{r^0} = K_3 \overleftarrow{k^0} \exp\left(-\frac{\overleftarrow{E_{a,c}^{eq}}}{kT}\right)$. One peculiar feature of this specific mechanism is the fact that forward and backward reaction have the same surface potential dependency, i.e. both reaction rates decrease with increasing surface potential. The reason for this behaviour is that in forward direction, the thermodynamic term of the preceding equilibrium ($-e\chi_0$, $-e\Delta\chi$) adds to the kinetic term of the rate limiting ion transfer ($\alpha e\chi_0$, $\alpha e\Delta\chi$) resulting in the same surface potential dependency as the kinetic factor of the backward reaction ($(\alpha-1)\, e\chi_0$, $(\alpha-1)\, e\Delta\chi$). The succeeding equilibrium does not contribute a surface potential dependency since no charge is transferred between the two phases. Equal surface potential

dependencies of forward and backward rate can occur if a preceding equilibrium involves a charge transfer with the opposite direction of the charge transfer in the rate determining step. In general, however, different dependencies of $\vec{r}$ and $\overleftarrow{r}$ result.

This example shows how an expression for the reaction rate can be derived for a given mechanism. The same approach can be applied to different mechanisms, leading to rate equations of the generalized form

$$\vec{r} = \overrightarrow{r_0}\, {p_{O_2}}^{\overrightarrow{\nu_p}}\, {c_D}^{\overrightarrow{\nu_D}}\, \exp\left(\frac{\vec{\beta} e \chi_0}{kT}\right) \exp\left(\frac{\vec{\beta} e \Delta\chi}{kT}\right) \tag{3.27}$$

$$\overleftarrow{r} = \overleftarrow{r_0}\, {p_{O_2}}^{\overleftarrow{\nu_p}}\, {c_D}^{\overleftarrow{\nu_D}}\, \exp\left(\frac{\overleftarrow{\beta} e \chi_0}{kT}\right) \exp\left(\frac{\overleftarrow{\beta} e \Delta\chi}{kT}\right) \tag{3.28}$$

where $\overrightarrow{r_0}$ and $\overleftarrow{r_0}$ are prefactors including chemical equilibrium constants of the pre- and succeeding reactions as well as pre-exponential factors and chemical activation energies of the rate determining step. ${c_D}^{\nu_D}$ represents the product of defect concentrations with their corresponding reaction orders, ${p_{O_2}}^{\nu_p}$ describes the oxygen partial pressure dependency via adsorbate species and $\vec{\beta}$ and $\overleftarrow{\beta}$ are factors depending on the mechanism. The equilibrium surface potential χ_0 generally depends on the oxygen partial pressure, since it is (partly) caused by charged adsorbates.[44,50]

Since reaction rates are proportional to current densities we finally get

$$j_c = j_c^0\, {p_{O_2}}^{\nu_{p,c}}\, {c_{D,c}}^{\nu_{D,c}}\, \exp\left(\frac{\beta_c e \chi_0}{kT}\right) \exp\left(\frac{\beta_c e \Delta\chi}{kT}\right) \tag{3.29}$$

$$j_a = j_a^0\, {p_{O_2}}^{\nu_{p,a}}\, {c_{D,a}}^{\nu_{D,a}}\, \exp\left(\frac{\beta_a e \chi_0}{kT}\right) \exp\left(\frac{\beta_a e \Delta\chi}{kT}\right) \tag{3.30}$$

for the anodic (j_a) and cathodic (j_c) current densities. As detailed above for the specific mechanism, β_a and β_c have non-trivial meanings, since they combine a thermodynamic effect of χ (via steps in equilibrium) with the kinetic charge transfer effect of the rate limiting step.

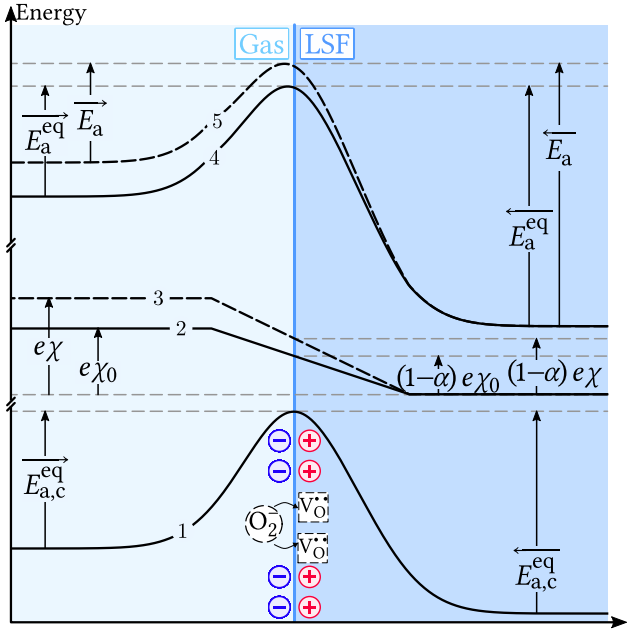

Figure 3.12: The incorporation of an $O^-_{2(ad)}$ion can be considered an ion jump over an activation barrier. Under equilibrium this energy barrier consists of a purely chemical energy contribution (1) with the activation energies $\overrightarrow{E_{a,c}^{eq}}$ and $\overleftarrow{E_{a,c}^{eq}}$ and an electrostatic potential term ($e\chi_0$) due to charged adsorbates (2). This potential term causes a modified energy barrier (4) with activation energies $\overrightarrow{E_a^{eq}} = \overrightarrow{E_{a,c}^{eq}} - \alpha e\chi_0$ and $\overleftarrow{E_a^{eq}} = \overleftarrow{E_{a,c}^{eq}} + (1-\alpha)e\chi_0$. Under current flow, the surface potential changes from its equilibrium value (3), and this further modifies the energy barrier (5) and leads to activation energies of $\overrightarrow{E_a} = \overrightarrow{E_{a,c}^{eq}} - \alpha e\chi_0 - \alpha e\Delta\chi$ and $\overleftarrow{E_a} = \overleftarrow{E_{a,c}^{eq}} + (1-\alpha)\,e\chi_0 + (1-\alpha)\,e\Delta\chi$ for the forward and backward reaction.

4 Rate equations for defect controlled reactions

The study presented in this chapter has been published as a scientific paper in the "Journal of the Electrochemical Society".[78]

4.1 Introduction

Studies aiming at mechanistic information often investigate the exchange current density by means of isotope exchange,[2,39] conductivity relaxation[40] or impedance spectroscopy.[6,41–44] While the determination of oxygen exchange rates via such close-to-equilibrium methods is well established and frequently employed, it is nevertheless often challenging to extract mechanistic details from such experiments, also because experimental data often include effects of both cathodic and anodic reactions.[43,45,46] In contrast, experiments far from equilibrium, i.e. at sufficiently high electrode polarization, enhance the reaction rate in one direction while suppressing the reaction in reverse direction, and thus may offer a better view, for example on the dependencies of reaction rates on concentrations. Nevertheless, measurements and mechanistic interpretations of oxygen reduction/evolution current-voltage curves are rather scarce,[16,47,48] and the concepts for a theoretical description of such current-voltage curves are still under development.[49,50,69]

Several differences exist between such solid|gas reactions and usual aqueous electrochemical reactions at metal electrodes, and the current-voltage characteristics of the solid|gas reactions often cannot be described by standard electrochemical models such as Butler-Volmer's equation.[50] First, in liquid electrochemistry an applied overpotential often translates directly into an electrostatic potential step at the reaction site, i.e. the electrolyte|electrode interface. For electrochemical reactions at MIEC|gas interfaces, however, an applied overpotential acts mainly upon the oxygen chemical potential in the MIEC electrode, and thereby on the MIEC defect concentrations.[2,46,57] The overpotential might also affect the potential step at the MIEC|gas interface, but mostly in a rather indirect and complex manner.[50] Second, the oxygen partial pressure not only determines the concentration of oxygen species adsorbed at the MIEC|gas

interface. Rather, the gas phase also affects the oxygen chemical potential in the MIEC electrode and thereby the concentration of defects involved in the reactions. Furthermore, in atmospheres consisting mostly of oxygen and nitrogen it is plausible that charged oxygen adsorbates are the main contributors to a possible electrostatic potential step at the MIEC|gas interface. Therefore, the oxygen partial pressure can also affect the surface potential.[50]

These considerations clearly show that the interpretation of current-voltage curves and their partial pressure dependencies requires novel concepts beyond standard models known from metal|liquid interfaces. Knowing the defect chemistry of the MIEC electrode and the interrelationship between defect concentrations, oxygen partial pressure and electrode polarization is vital for understanding the kinetics of such reactions. A quantitative approach to tackle such situations has been introduced in chapter 3, and it was shown how the true, i.e. mechanistically meaningful, reaction orders of defects and gas species can be determined from combined voltage and partial pressure variations.

In this chapter, we extend these considerations by modelling current-voltage curves for the known defect chemical data set of a specific material ($La_{0.6}Sr_{0.4}FeO_{3-\delta}$) and different possible reaction mechanisms. Various slopes of current-voltage curves can result, depending on the reaction mechanism and partial pressure. However, neither do limiting currents indicate any diffusion limitation, nor do exponential relations reflect charge transfer limitations. The true meanings of Tafel slopes and partial pressure dependent current densities are discussed for specific mechanisms and in general. This opens new ways to draw mechanistic conclusions from empirically measured current-voltage curves and partial pressure dependences.

4.2 Rate equation model for defect controlled reactions

In this section we derive an equation that describes the effect of the main experimental parameters (overpotential and oxygen partial pressure) on the current density resulting from oxygen reduction or evolution on a MIEC surface. These considerations are largely based on the rate equation model suggested in Ref. [72] and Ref. [69]. It describes the oxygen incorporation and evolution rates in terms of local defect concentrations, surface adsorbates and surface potentials. According to this rate equation model the current densities of anodic oxygen evolution (j_a) and cathodic oxygen incorporation (j_c) can be expressed as

$$j_a = j_a^{0*}\, {p_{O_2}}^{\nu_{p,a}}\, {c_{D,a}}^{\nu_{D,a}}\, \exp\left(\frac{\beta_a e \chi_0}{kT}\right) \exp\left(\frac{\beta_a e \Delta\chi}{kT}\right), \tag{4.1}$$

$$j_c = j_c^{0*}\, {p_{O_2}}^{\nu_{p,c}}\, {c_{D,c}}^{\nu_{D,c}}\, \exp\left(\frac{\beta_c e \chi_0}{kT}\right) \exp\left(\frac{\beta_c e \Delta\chi}{kT}\right), \tag{4.2}$$

where the net current density j is the difference between anodic and cathodic current density: $j = j_a - j_c$. Symbols j_a^{0*} and j_c^{0*} are constant prefactors including equilibrium constants of equilibria before and after the rate limiting step, p_{O_2} is the oxygen partial pressure and $\nu_{p,a}$ and $\nu_{p,c}$ are the corresponding reaction orders for the anodic and cathodic reactions. These partial pressure related factors describe the effect of p_{O_2} on the surface adsorbates involved in the rate liming step but do not include the p_{O_2} dependence of electronic or ionic defect concentrations.

Defects are treated separately and symbols $c_{D,a}$ and $c_{D,c}$ are the concentrations of the defect species in the MIEC being relevant in anodic or cathodic direction, with their corresponding reaction orders $\nu_{D,a}$ and $\nu_{D,c}$. If multiple defects are relevant, ${c_D}^{\nu_D}$ has to be expanded to a product such as ${c_{D_1}}^{\nu_{D_1}} {c_{D_2}}^{\nu_{D_2}}$. These relevant defects are either reaction partners in the rate determining step, or they are involved in preceding or succeeding equilibria. β_a and β_c are factors depending on the reaction mechanism, χ_0 and $\Delta\chi$ are the equilibrium surface potential and its variation upon current flow and e, k and T have their usual meaning of elementary charge, Boltzmann constant and temperature. Please note, the anodic and cathodic current densities in equation (4.1) and equation (4.2) represent the ionic current flowing in the MIEC from the surface towards the MIEC|electrolyte interface. However, it does not reflect the charge transferred across the MIEC surface itself since this depends on the specific mechanism. In principle, it is even possible to incorporate neutral oxygen and ionize the atoms within the MIEC; then there is no charge flow across the MIEC surface itself.

In equilibrium, i.e. at zero overpotential, the anodic and cathodic current densities are equal, thus

$$j_a^{eq} = j^0 = j_a^{0*} \, {p_{O_2}}^{\nu_{p,a}} \, {c_{D,a}^{eq}}^{\nu_{D,a}} \, \exp\left(\frac{\beta_a e \chi_0}{kT}\right), \tag{4.3}$$

$$j_c^{eq} = j^0 = j_c^{0*} \, {p_{O_2}}^{\nu_{p,c}} \, {c_{D,c}^{eq}}^{\nu_{D,c}} \, \exp\left(\frac{\beta_c e \chi_0}{kT}\right), \tag{4.4}$$

where $c_{D,a}^{eq}$ and $c_{D,c}^{eq}$ are the equilibrium concentrations of the relevant defects and j^0 is the exchange current density. This exchange current density is thus determined by the oxygen partial pressure, the equilibrium defect concentrations and the equilibrium surface potential χ_0. For a given temperature, the equilibrium defect concentrations are defined by p_{O_2} and the defect chemical equilibrium constant(s) of the MIEC. The equilibrium surface potential χ_0 may also depend on p_{O_2}.[44,50] Thus, for a given material, all variable factors can be traced back to the gas phase and the exchange current density j^0 depends on p_{O_2} solely. Combining equations (4.1)

to (4.4) leads to

$$j_\mathrm{a} = j^0 \frac{c_{\mathrm{D,a}}{}^{\nu_{\mathrm{D,a}}}}{c_{\mathrm{D,a}}^{\mathrm{eq}\ \nu_{\mathrm{D,a}}}} \exp\left(\frac{\beta_\mathrm{a} e\Delta\chi}{kT}\right), \tag{4.5}$$

$$j_\mathrm{c} = j^0 \frac{c_{\mathrm{D,c}}{}^{\nu_{\mathrm{D,c}}}}{c_{\mathrm{D,c}}^{\mathrm{eq}\ \nu_{\mathrm{D,c}}}} \exp\left(\frac{\beta_\mathrm{c} e\Delta\chi}{kT}\right), \tag{4.6}$$

and the net current density is then

$$j = j^0 \left[\exp\left(\frac{\beta_\mathrm{a} e\Delta\chi}{kT}\right)\left(\frac{c_{\mathrm{D,a}}}{c_{\mathrm{D,a}}^{\mathrm{eq}}}\right)^{\nu_{\mathrm{D,a}}} - \exp\left(\frac{\beta_\mathrm{c} e\Delta\chi}{kT}\right)\left(\frac{c_{\mathrm{D,c}}}{c_{\mathrm{D,c}}^{\mathrm{eq}}}\right)^{\nu_{\mathrm{D,c}}}\right]. \tag{4.7}$$

The relation between surface potential, oxygen partial pressure and overpotential can be very complex and may also vary with overpotential and $p_{\mathrm{O_2}}$.[50] Accordingly, $\Delta\chi$ is generally unknown which makes general predictions of current-voltage curves difficult. However, XPS studies on $\mathrm{La_{0.6}Sr_{0.4}FeO_{3-\delta}}$ suggest that the surface potential does not change much with overpotential or $p_{\mathrm{O_2}}$.[15] In the following we therefore assume such a simplified situation with a constant $\chi = \chi_0$ and thus $\Delta\chi = 0$ for all overpotentials and partial pressures. For such "defect controlled reactions", equation (4.7) can be simplified to

$$j = j^0 \left[\left(\frac{c_{\mathrm{D,a}}}{c_{\mathrm{D,a}}^{\mathrm{eq}}}\right)^{\nu_{\mathrm{D,a}}} - \left(\frac{c_{\mathrm{D,c}}}{c_{\mathrm{D,c}}^{\mathrm{eq}}}\right)^{\nu_{\mathrm{D,c}}}\right], \tag{4.8}$$

and for the exchange current densities (equations (4.3) and (4.4)) we get

$$j^0 = j_\mathrm{a}^0\ {p_{\mathrm{O_2}}}^{\nu_{\mathrm{p,a}}}\ c_{\mathrm{D,a}}^{\mathrm{eq}\ \nu_{\mathrm{D,a}}}, \tag{4.9}$$

$$j^0 = j_\mathrm{c}^0\ {p_{\mathrm{O_2}}}^{\nu_{\mathrm{p,c}}}\ c_{\mathrm{D,c}}^{\mathrm{eq}\ \nu_{\mathrm{D,c}}}. \tag{4.10}$$

where the prefactors j_a^0 and j_c^0 include j_a^{0*} and j_c^{0*} but also include the $p_{\mathrm{O_2}}$ independent equilibrium surface potential factors.

An applied overpotential causes a net current density ($j \neq 0$) by driving the defect concentrations in the MIEC electrode away from their equilibrium values, i.e. by changing the ratio $c_\mathrm{D}/c_\mathrm{D}^{\mathrm{eq}}$. (Please note: If several defects are involved in anodic or cathodic direction these ratios have to be replaced by products with ratios for each relevant ionic or electronic defect.) The current-voltage characteristics is therefore a direct consequence of the relation between defect concentrations and electrode overpotential. This relation can be quantified in the following manner: If the ion and electron transport in the electrode is much faster than the surface ex-

change reaction, the electrode overpotential η directly translates to a change in (molecular) oxygen chemical potential μ_{O_2} in the MIEC according to the Nernstian relation[2,57]

$$\mu_{O_2} = 4e\eta + kT \ln\left(\frac{p_{O_2}}{1\,\text{bar}}\right). \tag{4.11}$$

Under polarization, the defects are thus no longer in equilibrium with the gas phase (p_{O_2}), but are defined by the oxygen chemical potential in the electrode film according to equation (4.11). Accordingly, the change in oxygen chemical potential by $4e\eta$ causes a change in defect concentrations and thus a current according to equation (4.8).

The (equilibrium) defect chemistry of MIEC oxides is often described by Brouwer diagrams, which relate the defect concentrations to the oxygen partial pressure.[77] Actually, this p_{O_2} dependence of defect concentrations in the MIEC is a μ_{O_2} dependence. Only in equilibrium, μ_{O_2} in the MIEC is given by $\mu_{O_2} = kT \ln\left(\frac{p_{O_2}}{1\,\text{bar}}\right)$, while upon a current the overpotential changes μ_{O_2} according to equation (4.11). Studies of the chemical capacitance of LSF confirmed the equivalence of μ_{O_2} changes by electrode overpotential and gas phase p_{O_2}.[57] In simplified Brouwer diagrams the specific c_D vs. μ_{O_2} relations switch between two extremes: either the defect concentrations are essentially μ_{O_2} independent, or there exists an exponential relation[77]

$$c_D = c_D{}' \exp\left(n\frac{\mu_{O_2} - \mu'_{O_2}}{kT}\right). \tag{4.12}$$

For equilibrium situations ($\eta = 0$) the latter is equivalent to the power law relation

$$c_D = c_D{}'\left(\frac{p_{O_2}}{p'_{O_2}}\right)^n \tag{4.13}$$

between defect concentrations for two oxygen partial pressures p_{O_2} and p'_{O_2}. Exponent n describes the slope in the Brouwer diagram, e.g. 0.25 for electron holes as minority charge carriers in an acceptor doped MIEC or -0.5 for oxygen vacancies as minority defects.

Upon a current and for $c'_D = c_D^{eq}$ we can combine equations (4.11) and (4.12) and the resulting relation between defect concentration and the overpotential η is

$$c_D = c_D^{eq} \exp\left(\frac{4en\eta}{kT}\right). \tag{4.14}$$

Combining equations (4.8) and (4.14) finally yields

$$j = j^0\left[\exp\left(\frac{4en_{D,a}\nu_{D,a}\eta}{kT}\right) - \exp\left(\frac{4en_{D,c}\nu_{D,c}\eta}{kT}\right)\right]. \tag{4.15}$$

Again, involvement of several defect species in anodic or cathodic direction would mean that $n_{D,a}\nu_{D,a}$ or $n_{D,c}\nu_{D,c}$ have to be expanded to products including several defects. Equation (4.15) shows that for relevant defects following exponential relations with respect to μ_{O_2}, defect controlled reactions can also exhibit Butler-Volmer like exponential current-voltage characteristics. However, the reason for this curve shape is different than for Butler-Volmer reaction kinetics in aqueous systems. There, the two exponential terms originate from rate limiting charge transfer affected by a voltage induced change of the interfacial Galvani potential and thus of activation energies or shifts of electronic energy levels in solution.[75] In our MIEC case, on the other hand, the exponential curve shape is a consequence of changes in defect concentrations by the applied voltage, i.e. of Nernst's equation. The Tafel slopes of the exponential curves thus no longer include a symmetry factor of a charge transfer process. Rather, the slope is given by a product of the μ_{O_2} dependence of the relevant defects ($n_{D,a}$ and $n_{D,c}$), the defect reaction orders of the specific reaction mechanism ($\nu_{D,a}$ and $\nu_{D,c}$) and the factor of $4e$ from the Nernst relation between μ_{O_2} and η in equation (4.11).

For the sake of comparison, we may write equation (4.15) formally equivalent to a Butler-Volmer equation, i.e. as

$$j = j^0 \left[\exp\left(\frac{m_a \alpha e \eta}{kT}\right) - \exp\left(-\frac{m_c (1-\alpha) e \eta}{kT}\right)\right], \tag{4.16}$$

and for $\alpha = \frac{1}{2}$ we thus get

$$m_a = 8 n_{D,a} \nu_{D,a} \tag{4.17}$$

$$m_c = -8 n_{D,c} \nu_{D,c}\,. \tag{4.18}$$

Hence, the factor $m_{a,c}$, which may indicate the number of electrons transferred in standard liquid electrochemical cases, has a very different meaning here.[75] As an example: for two oxygen vacancies being involved in the reaction rate in cathodic direction ($\nu_{D,c} = 2$) and a vacancy related slope of -0.5 in a Brouwer diagram we find a m_c value of 8. If, on the other hand, the relevant defect concentrations are independent of the oxygen chemical potential ($\nu_D = 0$), the corresponding current density becomes η-independent, thus pretending a kind of diffusion limitation in a standard interpretations. In the following we will exemplify these relations between defect concentrations and current-voltage characteristics for different mechanisms on the perovskite material $La_{0.6}Sr_{0.4}FeO_{3-\delta}$ (LSF).

4.3 LSF defect model

In order to specify defect controlled current-voltage characteristics of a mixed conducting material, knowledge on its defect chemistry is required. For LSF as a model material the defect chemical model is well established and includes oxygen vacancies ($V_O^{\bullet\bullet}$), electron holes ($h^\bullet$) and electrons (e') as the main point defects. Electrons and holes are frequently attributed to the Fe cations and thus holes correspond to Fe^{4+} ($Fe_{Fe}^{\bullet}$) while electrons are realized by Fe^{2+} (Fe_{Fe}'). Some recent studies suggest that holes are more distributed across the oxygen ions surrounding the corresponding Fe ion.[67,79,80] Here, we use the general notation ($h^\bullet$ and e'). Thus the following two defect chemical equilibria exist

$$\tfrac{1}{2}\,O_2 + V_O^{\bullet\bullet} + 2\,Fe_{Fe}^{\times} \rightleftharpoons O_O^{\times} + 2\,h^{\bullet} \tag{4.19}$$

$$2\,Fe_{Fe}^{\times} \rightleftharpoons h^{\bullet} + e' \tag{4.20}$$

with mass action constants

$$K_{ox} = \exp\left(\frac{T\Delta S_{ox} - \Delta H_{ox}}{RT}\right) = \frac{c_{Ox}{c_h}^2}{\sqrt{p_{O_2}}c_V{c_{Fe}}^2} \tag{4.21}$$

$$K_i = \exp\left(\frac{T\Delta S_i - \Delta H_i}{RT}\right) = \frac{c_h c_e}{{c_{Fe}}^2}\,, \tag{4.22}$$

where c_V, c_h, c_e, c_{Fe}, c_{Ox} are the concentrations of oxygen vacancies, holes, electrons, Fe^{3+} ($Fe_{Fe}^{\times}$) and oxide ions, respectively. When dealing with dilute defects, the concentration of regular units is much larger than the defect concentrations and does not change notably with p_{O_2} or overpotential, it can be included in the respective equilibrium constants. In heavily doped mixed conductors such as LSF though, the concentration of ideal lattice species can easily be in the same range as defect concentrations. Therefore $Fe_{Fe}^{\times}$ and $O_O^{\times}$ are also included in the defect chemical equations and take into account the fact of site restriction. Activity coefficients due to defect interactions, however, are not included.[8,14,19,35]

Enthalpies and entropies for the oxygen exchange reaction and electron/hole pair formation in macroscopic LSF bulk samples were determined by thermogravimetry and coulometric titration.[8,14] Table 4.1 shows enthalpies and entropies for bulk LSF. Our own measurements of the chemical capacitance of thin LSF films (30 to 120 nm) are in good agreement for the oxygen exchange, but indicate higher electronic charge carrier concentrations in thin films.[57] For the following calculations we use the established bulk thermodynamic data set.

TABLE 4.1: Enthalpies and entropies for oxygen exchange (ΔH_{ox}, ΔS_{ox}) and electron/hole pair formation (ΔH_i, ΔS_i).[14]

ΔH_{ox}	($kJ\,mol^{-1}$)	-95.62 ± 4.18
ΔS_{ox}	($J\,mol^{-1}\,K^{-1}$)	-54.27 ± 4.43
ΔH_i	($kJ\,mol^{-1}$)	95.75 ± 2.05
ΔS_i	($J\,mol^{-1}\,K^{-1}$)	-21.63 ± 2.13

The Brouwer diagram for these bulk data is displayed in figure 4.1 for 600 °C. The ideal lattice sites ($O_O^\times$ and $Fe_{Fe}^\times$) are included to show that, especially for iron ($Fe_{Fe}^\times$) and electron holes ($h^\bullet$) in the oxidising regime, the concentrations can become comparable. For example, in high oxygen partial pressure the concentration of electron holes is 0.4 per unit cell, and thus the concentration of ideal lattice iron is 0.6 per unit cell. However, the voltage driven relative concentration changes of those ideal lattice species are small compared to those of the minority point defects, and thus their impact on the current-voltage characteristics is rather small.

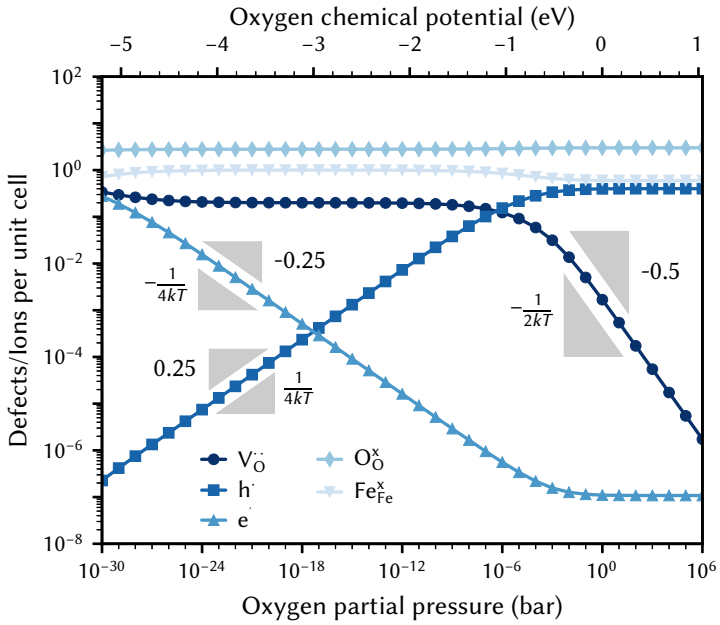

FIGURE 4.1: Brouwer diagram for LSF based on bulk data.[14] Slope markers above the respective curves denote the power law exponent in the defect concentration vs. p_{O_2} relation, see equation (4.13). Slope markers below the respective curves indicate the exponent in the defect concentration vs. μ_{O_2} relation, see equation (4.12).

Please note that these data reflect the defect chemistry of the LSF bulk. The surface defect chemistry relevant for the oxygen exchange reactions is not necessarily the same as the defect chemistry in the LSF bulk. However, we may assume that the surface defect chemistry is still governed by the same defect chemical equilibria, though with different equilibrium constants. Accordingly, the surface Brouwer diagram differs from the bulk diagram primarily by a shift on the p_{O_2} axis and a change in the electronic charge carrier concentrations. Hence, even though the following calculations are based on bulk defect chemistry they are also valid for the (unknown) surface defect chemistry, though the p_{O_2} validity ranges are most probably shifted. In the next sections we combine the kinetic model of section 4.2 and the defect model of section 4.3 and derive current-voltage curves for different specific reaction mechanisms, atomic and molecular ones, i.e. with an atomic or a molecular oxygen species in the rate determining step. Please note: The two reaction mechanisms discussed below were chosen to illustrate our "defect controlled" reaction kinetics model and its predictions, rather than with regards to their likeliness. They are representative also for more complex (and thus more realistic) mechanisms.

4.4 Current-voltage curves for an atomic mechanism

4.4.1 General equations and exchange current density

First we want to examine a simple atomic mechanism, i.e. one where the oxygen species in the rate determining step is atomic. This mechanism further illustrates the approach described in section 4.2 and also allows simple interpretation of the resulting dependencies. We assume fast adsorption and dissociation of oxygen (4.23), followed by the rate determining incorporation of the adsorbed O ad-atom (4.24), and a fast reduction to form oxide ions (4.25).

$$1/2\,O_2 \rightleftharpoons O_{(ad)} \tag{4.23}$$

$$O_{(ad)} + V_O^{\bullet\bullet} \overset{rds}{\rightleftharpoons} O_O^{\bullet\bullet} \tag{4.24}$$

$$O_O^{\bullet\bullet} + 2Fe_{Fe}^{\times} \rightleftharpoons O_O^{\times} + 2h^{\bullet} \tag{4.25}$$

Thus,

$$j_a = k_a c_{Opp} \tag{4.26}$$

$$j_c = k_c c_V \theta_a^0\,, \tag{4.27}$$

where c_{Opp} is the concentration of lattice oxygen with two positive relative charge ($O_O^{\bullet\bullet}$) and θ_a^0 is the surface coverage with neutral atomic oxygen ($O_{(ad)}$). The constant factors k_a and k_c are proportional to the rate constants of the anodic and cathodic reactions. The fast steps (4.23) and (4.25) are always in equilibrium and thus can be described by the mass action laws

$$K_{\mathrm{ion}} = \frac{c_{\mathrm{Ox}} {c_h}^2}{c_{\mathrm{Opp}} {c_{\mathrm{Fe}}}^2} \tag{4.28}$$

$$K_{\mathrm{ads}} = \frac{\theta_a^0}{\sqrt{p_{O_2}}} . \tag{4.29}$$

Combing equations (4.26) to (4.29) gives

$$j_a = j_a^0 {c_h}^2 c_{\mathrm{Ox}} {c_{\mathrm{Fe}}}^{-2} \tag{4.30}$$

$$j_c = j_c^0 \sqrt{p_{O_2}} c_V , \tag{4.31}$$

where $j_a^0 = k_a / K_{\mathrm{ion}}$ and $j_c^0 = k_c K_{\mathrm{ads}}$. Thus, equation (4.8) becomes:

$$j = j^0 \left[\left(\frac{c_h}{c_h^{\mathrm{eq}}} \right)^2 \left(\frac{c_{\mathrm{Ox}}}{c_{\mathrm{Ox}}^{\mathrm{eq}}} \right) \left(\frac{c_{\mathrm{Fe}}}{c_{\mathrm{Fe}}^{\mathrm{eq}}} \right)^{-2} - \left(\frac{c_V}{c_V^{\mathrm{eq}}} \right) \right] , \tag{4.32}$$

This is a first case where at least in anodic direction several defects are relevant and thus a product of defect terms has to be used in equation (4.8). However, the following calculations illustrate that only the c_h factor plays a decisive role for anodic currents.

The exchange current density in equation (4.32) is

$$j^0 = j_a^0 \left(c_h^{\mathrm{eq}} \right)^2 c_{\mathrm{Ox}}^{\mathrm{eq}} \left(c_{\mathrm{Fe}}^{\mathrm{eq}} \right)^{-2} = j_c^0 \sqrt{p_{O_2}} c_V^{\mathrm{eq}} . \tag{4.33}$$

Symbols c_h^{eq}, c_V^{eq}, $c_{\mathrm{Fe}}^{\mathrm{eq}}$ and $c_{\mathrm{Ox}}^{\mathrm{eq}}$ denote the equilibrium concentrations (i.e. without current flow) of electron holes, oxygen vacancies, lattice iron and lattice oxide, respectively. The exchange current density j^0 and the equilibrium defect concentrations are determined by the oxygen partial pressure via the defect chemical equilibria of LSF, i.e. by its Brouwer diagram, see figure 4.1.

Knowing the relation between defect concentrations and oxygen partial pressure, we can calculate the p_{O_2} dependence of the exchange current density (figure 4.2). The exchange current density is constant at high oxygen partial pressure. Only at lower oxygen partial pressure it scales with $\sqrt{p_{O_2}}$ as one might expect for an atomic mechanism. This is due to the fact that the p_{O_2} dependence of the exchange current density does not only depend on the nature of the oxygen species in the rate determining step, but includes also the reaction orders of the

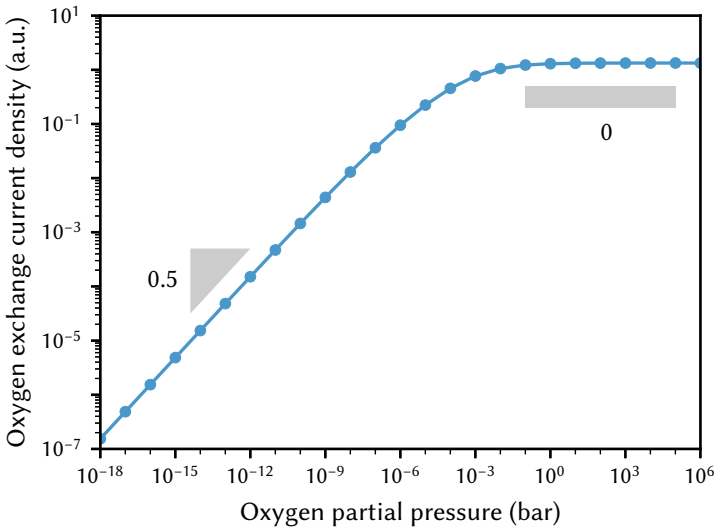

FIGURE 4.2: Oxygen exchange current density for the atomic mechanism as a function of oxygen partial pressure, calculated by equation (4.33).

relevant defects (equation (4.33)) and thus the partial pressure dependence of these defects. In this particular case, the slope of 0 in the high p_{O_2} regime of figure 4.2 is a combination of the slope of 0.5 (due to the atomic nature of the mechanism) and a slope of -0.5 due to the oxygen vacancy concentration decreasing with $\sqrt{p_{O_2}}$ in this regime.

An overpotential drives the defect concentration out of equilibrium by changing the oxygen chemical potential, see equation (4.11). The current-voltage curves can be calculated from equations (4.11) and (4.32) and the Brouwer diagram (figure 4.1) and depend on the oxygen partial pressure in the gas phase. Examples are shown in figure 4.3 for a broad p_{O_2} range. These current-voltage characteristics show a variety of Tafel-like exponential regions and current limited regions, both with various p_{O_2} dependencies. In the following, we discuss how these current-voltage characteristics for the anodic oxygen evolution and the cathodic oxygen incorporation are a direct consequence of the defect chemistry of LSF. Please note that related mechanisms, e.g. including formation of one electron hole into the rds (equation (4.24)), would lead to almost identical curves.

4.4.2 Anodic branch

In high oxygen partial pressures (figures 4.3a and 4.3b), the anodic current first increases steeply with overpotential but reaches a plateau already at very low overpotentials. This is because for high μ_{O_2} the concentration of electron holes is essentially constant, and thus the overpotential

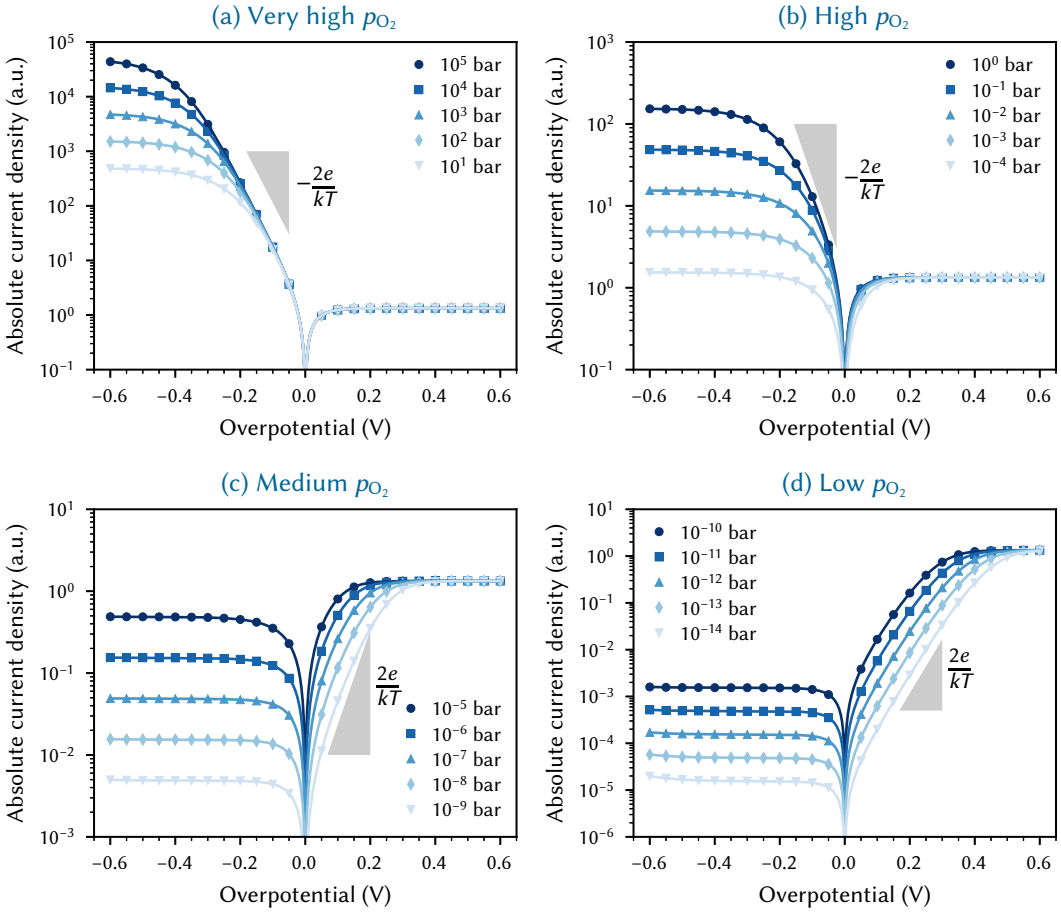

FIGURE 4.3: Current voltage characteristics for the atomic mechanism, calculated by equation (4.32), for different oxygen partial pressures. Defect concentrations are based on the Brouwer diagram in figure 4.1.

does not drive the hole concentration away from its equilibrium value noticeably. Therefore, the only effect of the overpotential in equation (4.32) is to suppress the cathodic current and this is the origin of the first steep increase in current. In the plateau regime, the anodic current-density is then just the exchange current density.

At lower oxygen partial pressures (figures 4.3c and 4.3d), higher overpotentials are required to reach this current limit, since the lower μ_{O_2} of the atmosphere has to be compensated by a larger overpotential to drive the electrode to a μ_{O_2} range of constant hole concentration. For low p_{O_2} and only moderate overpotentials the current-voltage curves thus become exponential, which reflects the exponential relation between electron holes and oxygen chemical potential in this regime. The Tafel slope of those current-voltage curves is $\frac{2e}{kT}$ and this value consists of

three factors:

$$\frac{\partial \ln j_a}{\partial \eta} = \frac{\partial \ln j_a}{\partial \ln c_h}\frac{\partial \ln c_h}{\partial \mu_{O_2}}\frac{\partial \mu_{O_2}}{\partial \eta} = 2\frac{1}{4kT}4e = \frac{2e}{kT}. \tag{4.34}$$

The first factor $\frac{\partial \ln j_a}{\partial \ln c_h}$ is the reaction order with respect to electron holes, i.e. 2 for this specific mechanism (cf. $\nu_{D,a}$ in equation (4.15)), the second one $\frac{\partial \ln c_h}{\partial \mu_{O_2}}$ is a consequence of the Brouwer diagram (cf. $n_{D,a}/kT$ in equation (4.15)) and the third one comes from Nernst's equation (4.11). In this exponential regime, the oxygen evolution current scales with oxygen partial pressure. This surprising accelerating effect of gaseous oxygen on the evolution rate (O_2 is a reaction product) is only indirect and caused by the LSF defect chemistry. More specific, the (equilibrium) hole concentration increases with ${p_{O_2}}^{0.25}$, and due to j^0 being proportional to $(c_h^{eq})^2$ (equation (4.33)) the current density for a given overpotential increases with ${p_{O_2}}^{0.5}$. In the high overpotential range where the hole concentration is constant at 0.4, however, the effect of p_{O_2} vanishes.

4.4.3 Cathodic branch

In very high oxygen partial pressures and under moderate cathodic polarization (figures 4.3a and 4.3b) the current is independent of p_{O_2} and increases exponentially with overpotential; the Tafel-slope in this regime is $-\frac{2e}{kT}$. At more cathodic overpotentials the current reaches a plateau and in this plateau regime the current becomes p_{O_2} dependent and scales with $\sqrt{p_{O_2}}$. The overpotential where this transition from exponential to flat current-voltage curves occurs also depends on the oxygen partial pressure. Again, this behaviour is a direct consequence of the LSF defect chemistry and the relation between defect concentrations and oxygen chemical potential. At high p_{O_2} the oxygen vacancy concentration increases with decreasing μ_{O_2}, i.e. the cathodic overpotential increases the current by driving the oxygen vacancy concentration away from its equilibrium value. The slope of $-\frac{2e}{kT}$ again consists of three factors, one from the specific mechanism, one from the Brouwer diagram and one from Nernst's equation:

$$\frac{\partial \ln j_c}{\partial \eta} = \frac{\partial \ln j_c}{\partial \ln c_V}\frac{\partial \ln c_V}{\partial \mu_{O_2}}\frac{\partial \mu_{O_2}}{\partial \eta} = 1\frac{-1}{2kT}4e = -\frac{2e}{kT}. \tag{4.35}$$

In this exponential regime the current is p_{O_2} independent because the accelerating effect of p_{O_2} via adsorbates is counter-balanced by the oxygen vacancy concentration decreasing with $\sqrt{p_{O_2}}$.

At very cathodic overpotentials, the oxygen vacancy concentration becomes μ_{O_2} independent. Thus the cathodic overpotential causes no further increase in oxygen vacancy concentration and the current becomes constant. However, in this regime the accelerating effect of p_{O_2}

via adsorbates is no longer counter-balanced by defect changes and therefore the current for a given overpotential scales with $\sqrt{p_{O_2}}$. In higher oxygen partial pressures (higher μ_{O_2}) higher cathodic overpotentials are required to drive the oxygen chemical potential into the regime with constant vacancy concentration, and thus the limiting current regime shifts to more cathodic overpotentials in higher p_{O_2}. In lower oxygen partial pressures (see figures 4.3c and 4.3d) the slope $\frac{2e}{kT}$ regime vanishes and the cathodic current reaches a current limited regime already at very low overpotentials. This is due to the oxygen vacancy concentration being constant and equal to its equilibrium value even at very low overpotential. Since there is no effect of p_{O_2} on the oxygen vacancy concentration the current scales with $\sqrt{p_{O_2}}$ in this regime.

Thus, in both anodic and cathodic direction we find current limited regimes. However, these current limitations are not caused by mass transport limitation, but instead are the result of the relevant defect concentrations being μ_{O_2} independent in those regimes.

4.4.4 Adsorption site restriction

So far the cathodic current scaled with $\sqrt{p_{O_2}}$ even at very high partial pressures, since we assumed that adsorbates are sufficiently dilute, i.e. site restriction was neglected. To account for limited adsorption sites, we can extend the given model by modifying the first reaction step to include adsorption sites (ad_a) for atomic oxygen (Langmuir-type dissociative adsorption). Steps (4.23) to (4.25) then transform to

$$\tfrac{1}{2}\,O_2 + ad_{(a)} \rightleftharpoons O_{(ad)} \tag{4.36}$$

$$O_{(ad)} + V_O^{\bullet\bullet} \underset{}{\overset{rds}{\rightleftharpoons}} O_O^{\bullet\bullet} + ad_{(a)} \tag{4.37}$$

$$O_O^{\bullet\bullet} + 2Fe_{Fe}^{\times} \rightleftharpoons O_O^{\times} + 2h^{\bullet}\,. \tag{4.38}$$

The equilibrium constant of the preceding adsorption equilibrium then becomes

$$K_{ads} = \frac{\theta_a^0}{\sqrt{p_{O_2}}\left(1-\theta_a^0\right)}\,. \tag{4.39}$$

From this we get

$$\theta_a^0 = \frac{K_{ads}\sqrt{p_{O_2}}}{1+K_{ads}\sqrt{p_{O_2}}}\,, \tag{4.40}$$

$$\left(1-\theta_a^0\right) = \frac{1}{1+K_{ads}\sqrt{p_{O_2}}}\,. \tag{4.41}$$

Equation (4.33) then becomes

$$j^0 = j_a^0 \left(c_h^{eq}\right)^2 \left(c_{Fe}^{eq}\right)^{-2} c_{Ox}^{eq} \frac{1}{1 + K_{ads}\sqrt{p_{O_2}}} = j_c^0 \sqrt{p_{O_2}} c_V^{eq} \frac{1}{1 + K_{ads}\sqrt{p_{O_2}}} . \tag{4.42}$$

with $j_a^0 = k_a / K_{ion}$ and $j_c^0 = k_c K_{ads}$.

Figure 4.4 shows the exchange current as a function of p_{O_2} for K_{ads} of 10 bar$^{-0.5}$, i.e. a situation where a p_{O_2} of 10 mbar leads to a surface coverage with atomic oxygen adsorbates of 50 %. In the low p_{O_2} regime the exchange current still increases with the square root of partial pressure; at higher p_{O_2} however, the exchange current decreases with $\sqrt{p_{O_2}}$ due to the increasing occupation of adsorption sites.

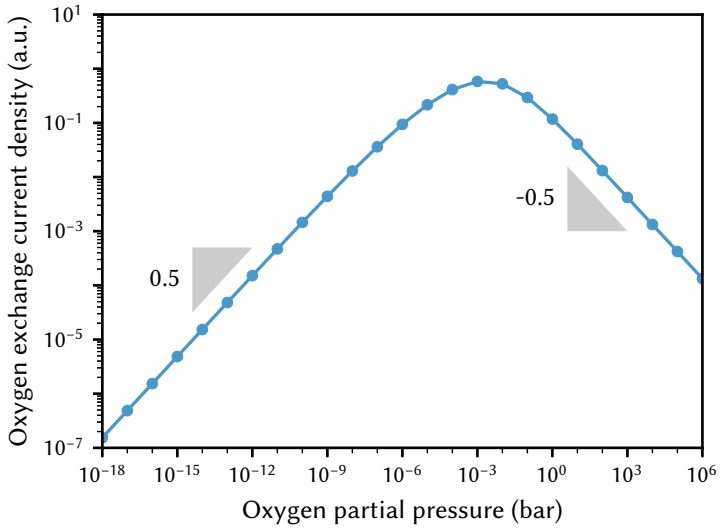

Figure 4.4: Oxygen exchange current density for the atomic mechanism with adsorption site restriction as a function of oxygen partial pressure, calculated by equation (4.42) with K_{ads} = 10 bar$^{-0.5}$.

This decrease at higher p_{O_2} is also reflected in the current-voltage curves shown in figure 4.5 (calculated from equations (4.32) and (4.42) and the Brouwer diagram in figure 4.1 at 600 °C). At moderately high oxygen partial pressure (figure 4.5b) the cathodic current still increases with p_{O_2}; at around 1 bar the cathodic current reaches a maximum and then decreases with increasing p_{O_2}, see figure 4.5a, in contrast to the situation without adsorption site restriction in figure 4.3a. This surprising decrease of the cathodic current density with increasing p_{O_2} is

due to the saturation of adsorption sites and the oxygen vacancy decrease for increasing p_{O_2}. Only the limiting current for very cathodic overpotentials remains p_{O_2} independent due to the saturation of c_V.

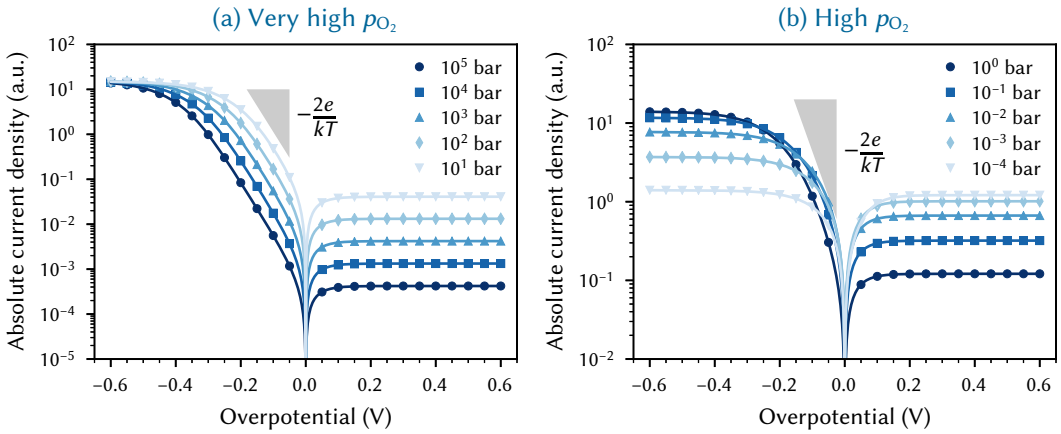

FIGURE 4.5: Current voltage characteristics for the atomic mechanism with adsorption site restriction for different oxygen partial pressures and K_{ads} of 10 bar$^{-0.5}$. Defect concentrations are based on the Brouwer diagram in figure 4.1.

Also for anodic currents the adsorption limitation affects the current-voltage characteristics. Without site restriction, a p_{O_2} independent limiting current was found for high oxygen partial pressure (figures 4.3a and 4.3b) due to the p_{O_2} independence of the hole concentration. With site restriction, however, free adsorption sites have to be available to form $O_{(ad)}$. Those sites are strongly reduced by high p_{O_2} and thus the limiting current (which is the exchange current) decreases with increasing p_{O_2}. The shape of the individual (cathodic and anodic) current-voltage curves, however, remains the same as discussed above, since the adsorption limitation only affects the exchange current density but not the overpotential dependent c_D/c_D^{eq} defect concentration ratios in equation (4.32).

4.5 Current-voltage curves for a molecular mechanism

4.5.1 General equations and exchange current density

As the second mechanism we consider a molecular mechanism: A fast adsorption and partial reduction of molecular oxygen (4.43) is followed by rate determining dissociation with partial incorporation of the adsorbate into an oxygen vacancy (4.44), and a fast incorporation of the remaining atomic oxygen dissociates with complete reduction of all incorporated O species

(4.45).

$$O_2 + Fe_{Fe}^{\times} \rightleftharpoons O_{2(ad)}^{-} + h^{\bullet} \tag{4.43}$$

$$O_{2(ad)}^{-} + V_O^{\bullet\bullet} \overset{rds}{\rightleftharpoons} O_O^{\bullet} + O_{(ad)} \tag{4.44}$$

$$O_{(ad)} + O_O^{\bullet} + V_O^{\bullet\bullet} + 3Fe_{Fe}^{\times} \rightleftharpoons 2O_O^{\times} + 3h^{\bullet} \tag{4.45}$$

The anodic and cathodic current densities are given by

$$j_a = k_a \theta_a^0 c_{Op} \tag{4.46}$$

$$j_c = k_c c_V \theta_m^- \tag{4.47}$$

where θ_a^0 and θ_m^- are the surface coverages with neutral atomic oxygen ($O_{(ad)}$) and negatively charged molecular oxygen ($O_{2(ad)}^-$), respectively. Symbol c_{Op} denotes the concentration of oxygen with one positive relative charge ($O_O^{\bullet}$). Steps (4.43) and (4.45) are assumed sufficiently fast and thus always in equilibrium with the mass action laws

$$K_{ion} = \frac{{c_{Ox}}^2 {c_h}^3}{\theta_a^0 c_{Op} c_V {c_{Fe}}^3} \tag{4.48}$$

$$K_{ads} = \frac{\theta_m^- c_h}{p_{O_2} c_{Fe}} . \tag{4.49}$$

Combining equations (4.46) to (4.49) gives

$$j_a = j_a^0 {c_{Ox}}^2 {c_h}^3 {c_{Fe}}^{-3} {c_V}^{-1} \tag{4.50}$$

$$j_c = j_c^0 p_{O_2} c_V c_{Fe} {c_h}^{-1} , \tag{4.51}$$

with $j_a^0 = k_a / K_{ion}$ and $j_c^0 = k_c K_{ads}$. Equation (4.8) thus becomes

$$j = j^0 \left[\left(\frac{c_{Ox}}{c_{Ox}^{eq}} \right)^2 \left(\frac{c_h}{c_h^{eq}} \right)^3 \left(\frac{c_{Fe}}{c_{Fe}^{eq}} \right)^{-3} \left(\frac{c_V}{c_V^{eq}} \right)^{-1} - \left(\frac{c_V}{c_V^{eq}} \right) \left(\frac{c_{Fe}}{c_{Fe}^{eq}} \right) \left(\frac{c_h}{c_h^{eq}} \right)^{-1} \right] , \tag{4.52}$$

with the partial pressure dependent exchange current density

$$j^0 = j_a^0 \left(c_{Ox}^{eq} \right)^2 \left(c_h^{eq} \right)^3 \left(c_{Fe}^{eq} \right)^{-3} \left(c_V^{eq} \right)^{-1} = j_c^0 p_{O_2} c_V^{eq} c_{Fe}^{eq} \left(c_h^{eq} \right)^{-1} . \tag{4.53}$$

In figure 4.6 the exchange current density, i.e. the reaction rate of the anodic and cathodic reactions without bias, is plotted versus p_{O_2} in arbitrary units. At low oxygen partial pressure the exchange current scales with ${p_{O_2}}^{0.75}$. Intuitively one might assume a slope of 1 versus

p_{O_2} for a molecular mechanism. However, the exchange current density depends not only on the nature of the oxygen species in the rate determining step (atomic or molecular) but also on the defect concentrations. The reason for the slope of 0.75 is that the oxygen partial pressure also acts upon the concentration of electron holes (slope of 0.25 vs. p_{O_2}). Since holes enter the cathodic reaction rate with a negative exponent, it partly counteracts the direct p_{O_2} effect via adsorbates, resulting in a p_{O_2} dependency of 0.75. Alternatively, one may consider the anodic direction in equation (4.53), where the oxygen partial pressure only affects the exchange current density indirectly by changing the electron hole concentration (slope 0.25). This also results in a slope of 0.75 since three holes are involved in the anodic reaction rate. Oxygen vacancies are irrelevant as their concentration is constant in the low p_{O_2} regime.

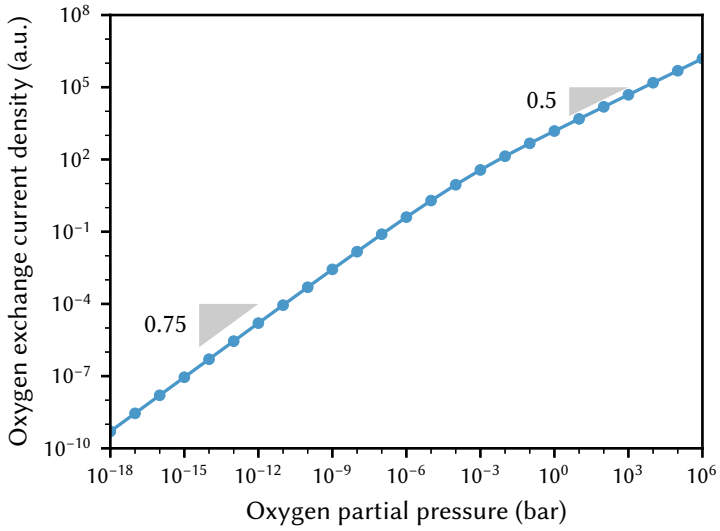

FIGURE 4.6: Oxygen exchange current density for the molecular mechanism as a function of oxygen partial pressure, calculated by equation (4.53).

At high oxygen partial pressure the exchange current scales only with $\sqrt{p_{O_2}}$, and this might be interpreted in terms of an atomic mechanism. However, this is again due to p_{O_2} induced changes in defect concentrations. In the cathodic direction the reaction order of one with respect to p_{O_2} (direct effect via adsorbates) is partly counter-balanced by the oxygen vacancy concentration decreasing with $\sqrt{p_{O_2}}$ and thus a reaction order of 0.5 results. Alternatively, we may again consider the anodic direction, where the indirect effect (oxygen vacancy concentration decreasing with increasing p_{O_2}) also leads to a slope of 0.5 since the anodic exchange

current density is proportional to $\left(c_V^{eq}\right)^{-1}$. The reaction orders with respect to electron holes play no role here, as the electron hole concentration is constant in high oxygen partial pressures.

This example shows that the common connection of molecular mechanisms with a linear scaling of the exchange current density with p_{O_2} (slope of 1) is not mandatory. Rather, the p_{O_2} dependence of j^0 is a complex interplay between the nature of the oxygen adsorbate in the rate determining step, the involved defects and their p_{O_2} dependence. In this example, the oxygen exchange current density at high p_{O_2} scales with ${p_{O_2}}^{0.5}$, which is often interpreted as a sign of an atomic reaction mechanism.

From equations (4.52) and (4.53) we can calculate the partial pressure dependent current-voltage characteristics, which are shown in figure 4.7. Below we discuss how these curves can be interpreted as a result of the LSF defect chemistry.

4.5.2 Anodic polarization

In high oxygen partial pressures (see figures 4.7a and 4.7b) the current-voltage curves are exponential and thus show straight lines in the Tafel plot. Since the overpotential acts by driving defect concentrations away from their equilibrium values, the reason for the shape of these curves is a consequence of the Brouwer diagram. Oxygen vacancies and electron holes both affect the anodic reaction rate (and thus current density) by the preceding equilibrium in equation (4.43). However, the electron hole concentration is virtually constant at these high oxygen chemical potentials. Thus, the effect of anodic overpotential is to decrease the concentration of oxygen vacancies, which causes an increase of the net current density, as the anodic reaction order with respect to vacancies is -1. The slope of $\ln j_a$ vs. η is $\frac{2e}{kT}$ and this value consist of three factors:

$$\frac{\partial \ln j_a}{\partial \eta} = \frac{\partial \ln j_a}{\partial \ln c_V}\frac{\partial \ln c_V}{\partial \mu_{O_2}}\frac{\partial \mu_{O_2}}{\partial \eta} = -1\frac{-1}{2kT}4e = \frac{2e}{kT}. \tag{4.54}$$

The first factor $\frac{\partial \ln j_a}{\partial \ln c_V}$ is the reaction order with respect to oxygen vacancies, i.e. -1 for this specific mechanism, the second one $\frac{\partial \ln c_V}{\partial \mu_{O_2}}$ is a consequence of the Brouwer diagram and the third one comes from Nernst's equation (4.11). The current also scales with ${p_{O_2}}^{0.5}$ which reflects the slope of the exchange current (see figure 4.6); the reason for this accelerating effect of p_{O_2} is only an indirect one due to the oxygen vacancy concentration scaling with ${p_{O_2}}^{-0.5}$.

In lower oxygen partial pressures (see figures 4.7c and 4.7d) the current-voltage curves are also exponential, but the slope varies from $\frac{3e}{kT}$ at lower overpotentials to $\frac{2e}{kT}$ at higher overpotentials; the overpotential of this transition depends on p_{O_2}. Again, the slopes can be understood as a consequence of the LSF Brouwer diagram. Oxygen vacancies and electrons enter

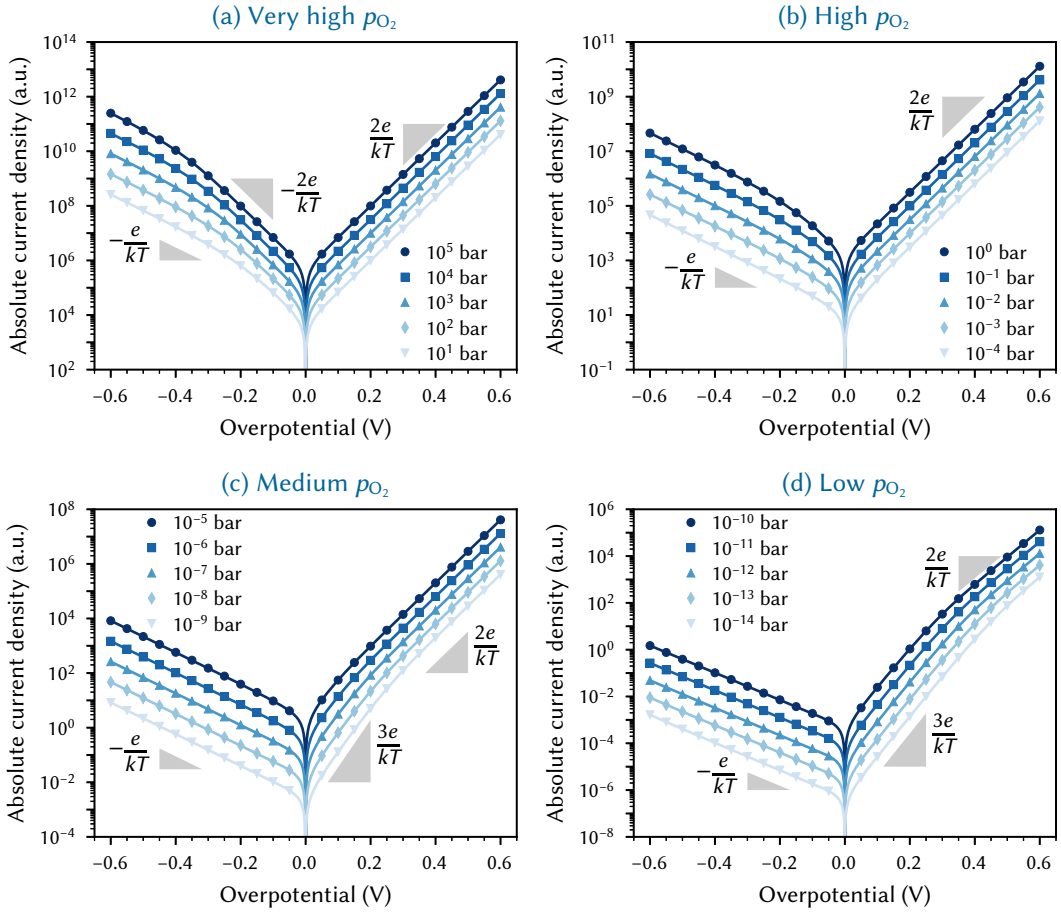

FIGURE 4.7: Current voltage characteristics for the molecular mechanism, calculated by equation (4.52), for different oxygen partial pressures. Defect concentrations are based on the Brouwer diagram in figure 4.1.

the anodic rate equation, but in the low μ_{O_2} regime (i.e. for low overpotential and low p_{O_2}) the concentration of vacancies is constant and the overpotential acts by increasing the electron hole concentration. The slope of $\ln j_a$ vs. η ($\frac{3e}{kT}$) is again the sum of three terms:

$$\frac{\partial \ln j_a}{\partial \eta} = \frac{\partial \ln j_a}{\partial \ln c_h} \frac{\partial \ln c_h}{\partial \mu_{O_2}} \frac{\partial \mu_{O_2}}{\partial \eta} = 3\frac{1}{4kT}4e = \frac{3e}{kT}. \tag{4.55}$$

At higher overpotentials (and thus high μ_{O_2}) the electron hole concentration reaches a plateau and the oxygen vacancy concentration starts to decrease, resulting in a slope of $\frac{2e}{kT}$ as described above. This also explains why the overpotential of the transition from $\frac{3e}{kT}$ to $\frac{2e}{kT}$ depends on p_{O_2},

since at low oxygen partial pressures higher overpotentials are required to reach the oxygen chemical potential where the minority charge carrier changes from electron holes to oxygen vacancies. At low overpotential the current scales with ${p_{O_2}}^{0.75}$ which is due to the hole concentration increasing with ${p_{O_2}}^{0.25}$ in accordance with the slope of the exchange current density. At higher overpotentials the current scales only with ${p_{O_2}}^{0.5}$, since there the vacancies are the μ_{O_2} dependent defects.

4.5.3 Cathodic polarization

Under mildly cathodic polarization and in very high oxygen partial pressures (figures 4.7a and 4.7b), the oxygen incorporation rate increases exponentially with overpotential with an exponent of $-\frac{2e}{kT}$ and the p_{O_2} dependence of j_c in this regime is $j_c \propto {p_{O_2}}^{0.5}$. At higher overpotentials the curves bend towards a slope of $-\frac{e}{kT}$, the overpotentials where this transition occurs depends again on p_{O_2}. Furthermore, j_c scales with ${p_{O_2}}^{0.75}$. This behaviour can again be explained as a direct consequence of the LSF defect chemistry. Both oxygen vacancies and electron holes enter the cathodic current density in equation (4.52). At low polarization (and thus in the high μ_{O_2} regime) the electron hole concentration is essentially constant, but the oxygen vacancy concentration changes with μ_{O_2}. An applied overpotential thus acts by increasing the oxygen vacancy concentration and the resulting slope of $-\frac{2e}{kT}$ consists of three factors:

$$\frac{\partial \ln j_c}{d\eta} = \frac{\partial \ln j_c}{\partial \ln c_V}\frac{\partial \ln c_V}{\partial \mu_{O_2}}\frac{\partial \mu_{O_2}}{\partial \eta} = 1\frac{-1}{2kT}4e = -\frac{2e}{kT}. \tag{4.56}$$

The current scales with ${p_{O_2}}^{0.5}$ in this regime, since the reaction order due to molecular gas adsorbates ($\nu_{p,c} = 1$) is partly compensated by the oxygen vacancy concentration which decreases with ${p_{O_2}}^{0.5}$.

At sufficiently large cathodic overpotentials the oxygen vacancy concentration reaches a plateau and the electron holes start to decrease with increasingly cathodic overpotential. The overpotential thus acts now by decreasing the electron hole concentration resulting is a slope of $-\frac{e}{kT}$ according to

$$\frac{d \ln j_c}{d\eta} = \frac{d \ln j_c}{d \ln c_h}\frac{d \ln c_h}{d\mu_{O_2}}\frac{d\mu_{O_2}}{d\eta} = -1\frac{1}{4kT}4e = -\frac{e}{kT}. \tag{4.57}$$

The overpotential at which this transition from $-\frac{2e}{kT}$ to $-\frac{e}{kT}$ occurs depends on p_{O_2} since high oxygen partial pressures require more cathodic overpotentials to reach the μ_{O_2} regime where electron holes begin to change with μ_{O_2}. The partial pressure dependence of the current-density in the $-\frac{e}{kT}$ regime is ${p_{O_2}}^{0.75}$, since here the reaction order due to molecular gas adsorbates ($\nu_{p,c}$)

of 1 gets reduced by 0.25 due to the electron hole concentration increasing with $p_{O_2}{}^{0.25}$. In lower oxygen partial pressures (figures 4.7c and 4.7d) the slope is constant at $-\frac{e}{kT}$ since even at very low cathodic polarization the oxygen chemical potential is already in the regime where the oxygen vacancy concentration is constant. Consequently, the only effect of the overpotential on the current occurs via decreasing the electron hole concentration.

In contrast to the atomic mechanism (figure 4.3) neither anodic nor cathodic limiting currents are found for the molecular mechanisms considered here (figure 4.7). This is due to the fact that anodic as well as cathodic currents depend on both, oxygen vacancies and holes, see equation (4.32). In accordance with the Brouwer diagram either c_V or c_h has to depend on μ_{O_2} and thus exponential current-voltage curves are found in all cases.

4.5.4 Adsorption site limitation

In section 4.4.4 we discussed the effect of adsorption site limitation for the case of neutral adsorption, i.e. without charge transfer prior to the rate determining step. There, we found that the adsorption site only causes a decreasing exchange current-density above a certain p_{O_2} threshold, while leaving the individual current-voltage relations unchanged. Below, we discuss the effects of site restriction on the current-voltage and current-partial pressure relations for our molecular mechanism, i.e. for the case where there is an electron transfer prior to the rate limiting step.

We again assume a Langmuir-type adsorption, i.e. we neglect any variation of the adsorption enthalpy with coverage and specifically neglect any surface potential changes. For the sake of simplicity, we neglect site limitation for the intermediate atomic adsorbates ($O_{(ad)}$), and further assume different adsorption sites for molecular and atomic adsorbates. Steps (4.43) to (4.45) then transform to

$$O_2 + ad_{(m)} + Fe_{Fe}^{\times} + \rightleftharpoons O_{2(ad)}^{-} + h^{\bullet} \tag{4.58}$$

$$O_{2(ad)}^{-} + V_O^{\bullet\bullet} \overset{\text{rds}}{\rightleftharpoons} O_O^{\bullet} + O_{(ad)} + ad_{(m)} \tag{4.59}$$

$$O_{(ad)} + O_O^{\bullet} + V_O^{\bullet\bullet} + 3Fe_{Fe}^{\times} \rightleftharpoons 2O_O^{\times} + 3h^{\bullet} \tag{4.60}$$

The equilibrium constant of the preceding adsorption equilibrium then becomes

$$K_{ads} = \frac{\theta_m^{-} c_h}{p_{O_2}\left(1-\theta_m^{-}\right) c_{Fe}}\,. \tag{4.61}$$

From this we get

$$\theta_{\mathrm{m}}^{-} = \frac{1}{1 + K_{\mathrm{ads}} p_{\mathrm{O}_2} c_{\mathrm{Fe}} / c_{\mathrm{h}}} K_{\mathrm{ads}} p_{\mathrm{O}_2} \frac{c_{\mathrm{Fe}}}{c_{\mathrm{h}}}, \tag{4.62}$$

$$\left(1 - \theta_{\mathrm{m}}^{-}\right) = \frac{1}{1 + K_{\mathrm{ads}} p_{\mathrm{O}_2} c_{\mathrm{Fe}} / c_{\mathrm{h}}}. \tag{4.63}$$

Equation (4.53) then becomes

$$\begin{aligned} j^0 &= j_{\mathrm{a}}^0 \left(c_{\mathrm{h}}^{\mathrm{eq}}\right)^3 \left(c_{\mathrm{V}}^{\mathrm{eq}}\right)^{-1} \left(c_{\mathrm{Fe}}^{\mathrm{eq}}\right)^{-3} \left(c_{\mathrm{Ox}}^{\mathrm{eq}}\right)^2 \frac{1}{1 + K_{\mathrm{ads}} p_{\mathrm{O}_2} c_{\mathrm{Fe}}^{\mathrm{eq}} / c_{\mathrm{h}}^{\mathrm{eq}}} \\ &= j_{\mathrm{c}}^0 p_{\mathrm{O}_2} \left(c_{\mathrm{V}}^{\mathrm{eq}}\right) \left(c_{\mathrm{h}}^{\mathrm{eq}}\right)^{-1} \left(c_{\mathrm{Fe}}^{\mathrm{eq}}\right) \frac{1}{1 + K_{\mathrm{ads}} p_{\mathrm{O}_2} c_{\mathrm{Fe}}^{\mathrm{eq}} / c_{\mathrm{h}}^{\mathrm{eq}}}, \end{aligned} \tag{4.64}$$

with $j_{\mathrm{a}}^0 = k_{\mathrm{a}} / K_{\mathrm{ion}}$ and $j_{\mathrm{c}}^0 = k_{\mathrm{c}} K_{\mathrm{ads}}$.

We assume an equilibrium constant for the adsorption (K_{ads}) of $59.4\,\mathrm{bar}^{-1}$ such that the surface coverage (θ_{m}^{-}) is 50 % at an oxygen partial pressure of 10 mbar; similar to the atomic mechanism discussed in section 4.4.4. The additional factor of 0.594 compared to section 4.4.4 is due to the involvement of electron holes in the adsorption equilibrium. Figure 4.8 shows the exchange current density as a function of p_{O_2}. In the low p_{O_2} regime the site restriction is irrelevant and the exchange current still increases with ${p_{\mathrm{O}_2}}^{0.75}$ as described above. At higher p_{O_2} however, the exchange current decreases with ${p_{\mathrm{O}_2}}^{-0.5}$ due to the increasing occupation of adsorption sites. In principle, electron holes are involved in the adsorption equilibrium, and thus their (p_{O_2} dependent) concentration also affects the adsorbate concentration. However, for this specific value of K_{ads} the hole concentration is almost constant in the regime where the site restriction becomes relevant. Thus, in the high p_{O_2} regime the oxygen partial pressure acts only by decreasing oxygen vacancy concentration and thus the exchange current-density decreases with ${p_{\mathrm{O}_2}}^{0.5}$. Equivalently, we may consider the anodic j^0 in equation (4.42) and see that higher p_{O_2} decreases the number of free adsorption sites needed to form $\mathrm{O}_{2(\mathrm{ad})}^{-}$.

For the current under polarization, equation (4.52) has to be replaced by

$$j = j^0 \frac{1 + K_{\mathrm{ads}} p_{\mathrm{O}_2} \frac{c_{\mathrm{Fe}}^{\mathrm{eq}}}{c_{\mathrm{h}}^{\mathrm{eq}}}}{1 + K_{\mathrm{ads}} p_{\mathrm{O}_2} \frac{c_{\mathrm{Fe}}}{c_{\mathrm{h}}}} \left[\left(\frac{c_{\mathrm{Ox}}}{c_{\mathrm{Ox}}^{\mathrm{eq}}} \right)^2 \left(\frac{c_{\mathrm{h}}}{c_{\mathrm{h}}^{\mathrm{eq}}} \right)^3 \left(\frac{c_{\mathrm{Fe}}}{c_{\mathrm{Fe}}^{\mathrm{eq}}} \right)^{-3} \left(\frac{c_{\mathrm{V}}}{c_{\mathrm{V}}^{\mathrm{eq}}} \right)^{-1} - \left(\frac{c_{\mathrm{V}}}{c_{\mathrm{V}}^{\mathrm{eq}}} \right) \left(\frac{c_{\mathrm{Fe}}}{c_{\mathrm{Fe}}^{\mathrm{eq}}} \right) \left(\frac{c_{\mathrm{h}}}{c_{\mathrm{h}}^{\mathrm{eq}}} \right)^{-1} \right]. \tag{4.65}$$

Figure 4.9 shows the corresponding current-voltage curves for a wide p_{O_2} range. At low oxygen partial pressures (figures 4.9c and 4.9d) the current-voltage curves are very similar to the ones without adsorption site restriction discussed above (figures 4.7c and 4.7d) in both anodic and

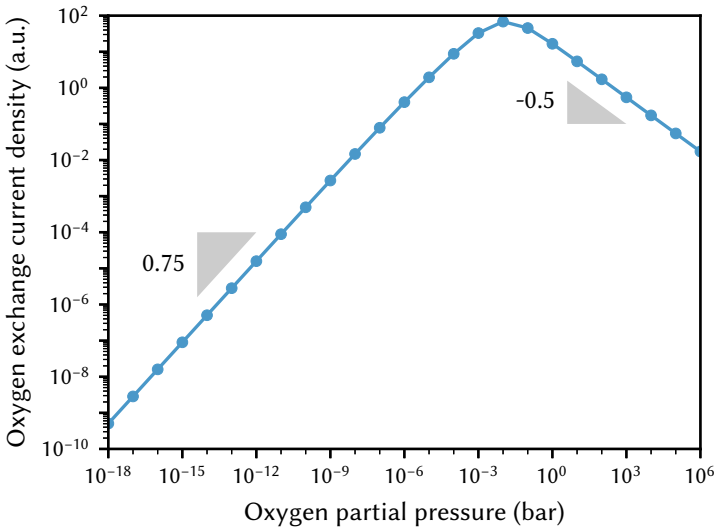

FIGURE 4.8: Oxygen exchange current density for the molecular mechanism with adsorption site restriction as a function of oxygen partial pressure, calculated by equation (4.64) for $K_{\text{ads}} = 59.4\,\text{bar}^{-1}$.

cathodic direction. However, at higher oxygen partial pressures (figures 4.9a and 4.9b) the situation is very different since the adsorption site restriction becomes relevant and depends on the overpotential.

In the anodic direction, the current reaches a maximum at an oxygen partial pressure of 100 mbar and scales with ${p_{O_2}}^{-0.5}$ at higher oxygen partial pressures, which reflects the p_{O_2} dependence of the exchange current density. The involvement of electron holes in the adsorption equilibrium plays no role here, since at high p_{O_2}, where site restriction is relevant, the electron hole concentration does not change with p_{O_2} or anodic overpotential. Therefore, the accelerating effect of p_{O_2} (due to $c_V \propto {p_{O_2}}^{-0.5}$) gets overcompensated by a decelerating effect due to the number of free adsorption sites decreasing linearly with increasing p_{O_2}. The shape of the individual current-voltage curves is unaffected by the adsorption site restriction.

In the cathodic direction, the relation between current density, overpotential and partial pressure is more complex. This is because electron holes are involved in the adsorption equilibrium (4.58) and the surface coverage is thus tied to the defect chemistry. Accordingly, site occupancy is affected by the overpotential. More specific, high cathodic overpotentials lower the hole concentration and thus increase the coverage with $O_{2(ad)}^{-}$, possibly approaching full occupancy. At moderate oxygen partial pressures (10^{-5} to 10^{-4} bar) the current first increases exponentially with cathodic overpotential; the corresponding Tafel slope is $-\frac{e}{kT}$. As described above, this slope originates from the decreasing electron hole concentration. Since the surface

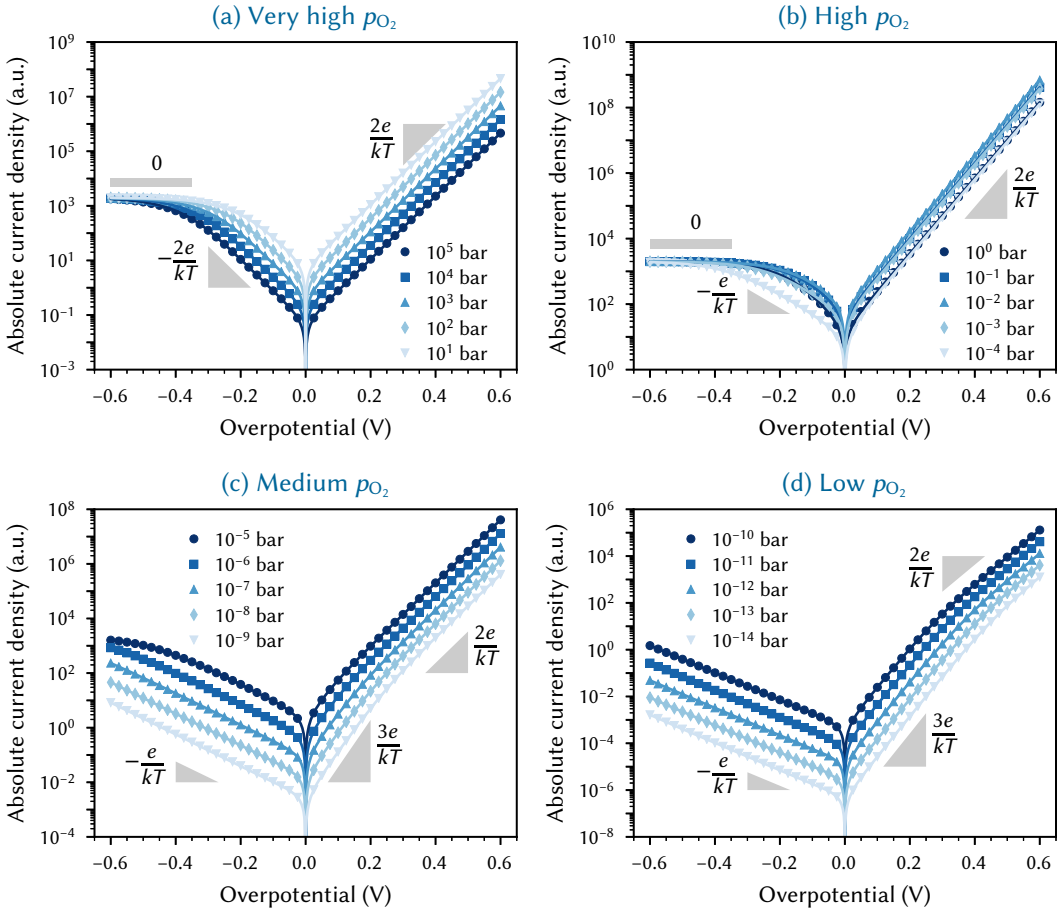

Figure 4.9: Current voltage characteristics for the molecular mechanism with adsorption site restriction for different oxygen partial pressures. Defect concentrations are based on the Brouwer diagram in figure 4.1.

coverage has not reached saturation, the current also increases with p_{O_2}. At more cathodic overpotentials, however, the surface coverage reaches saturation due to the low electron hole concentration. The overpotential thus neither affects the oxygen vacancy concentration nor the surface coverage and thus the current becomes constant, cf. equation (4.47). Furthermore, since the surface is saturated with adsorbates the current also becomes p_{O_2} independent.

At even higher oxygen partial pressures, the current first increases with a Tafel slope of $-\frac{2e}{kT}$ before reaching a current limited regime. Here, the surface is saturated with adsorbates already at zero overpotential and thus an applied overpotential only acts by increasing the

oxygen vacancy concentration, which leads to the Tafel slope of $-\frac{2e}{kT}$. At higher cathodic overpotentials, the oxygen vacancy concentration reaches a plateau and the current becomes constant.

This examplary mechanism illustrates that even without considering any surface potential changes, the adsorbate concentration is tied to the overpotential due to the involvement of defects in the adsorption equilibrium. In the simple case without adsorption site restriction this causes exponential current-voltage curves with a Tafel slope of $-\frac{e}{kT}$ in the low μ_{O_2} regime. If the finite number of adsorption sites is considered, this dependency of the surface coverage on the overpotential (via defect concentrations) leads to a situation, where the surface becomes saturated with adsorbates even at moderately low p_{O_2} if the overpotential is sufficiently cathodic. Moreover, this saturation can cause limiting currents also for the mechanism under investigation, in contrast the case without saturation (figure 4.7).

4.6 Generalized Tafel-slope and partial pressure dependence

In the discussion of the two mechanisms in sections 4.4 and 4.5 we derived the dependencies of the current densities on oxygen partial pressure and the overpotential as a consequence of defect concentrations, based on the known LSF Brouwer diagram. In the following, we derive generalised expressions for the slopes of the anodic and cathodic current densities with respect to p_{O_2} and overpotential, i.e. for the exponents of the p_{O_2} power laws and the Tafel slopes.

The anodic and cathodic current densities in equilibrium (equations (4.3) and (4.4)) have to be in accordance with the mass action laws of the defect chemical reactions, i.e. the oxygen exchange (equation (4.21)) and the iron disproportionation (equation (4.22)). For the sake of simplicity we neglect $O_O^\times$ and $Fe_{Fe}^\times$ as defect species with changing concentrations and thus only oxygen vacancies $V_O^{\bullet\bullet}$, electrons e' and electron holes $h^\bullet$ are left from the defect model of LSF (or other acceptor doped mixed conductors). For those we can specify equations (4.1) and (4.2), still assuming $\Delta\chi = 0$:

$$j_a = j_a^0 c_V^{\nu_{V,a}} c_h^{\nu_{h,a}} c_e^{\nu_{e,a}} p_{O_2}^{\nu_{p,a}} \tag{4.66}$$

$$j_c = j_c^0 c_V^{\nu_{V,c}} c_h^{\nu_{h,c}} c_e^{\nu_{e,c}} p_{O_2}^{\nu_{p,c}} . \tag{4.67}$$

Equilibrium means $j_a = j_c$ and thus

$$\frac{j_c^0}{j_a^0} = K_{kin} = c_V^{(\nu_{V,a}-\nu_{V,c})} c_h^{(\nu_{h,a}-\nu_{h,c})} c_e^{(\nu_{e,a}-\nu_{e,c})} p_{O_2}^{(\nu_{p,a}-\nu_{p,c})} . \tag{4.68}$$

Moreover, we know from equation (4.22) that

$$K_\mathrm{i} {c_\mathrm{Fe}}^2 = K_\mathrm{i}' = c_\mathrm{h} c_\mathrm{e} \tag{4.69}$$

and therefore $c_\mathrm{e} = K_\mathrm{i}'/c_\mathrm{h}$. Hence,

$$K_\mathrm{kin}/{K_\mathrm{i}'}^{\left(\nu_{\mathrm{e,a}}-\nu_{\mathrm{e,c}}\right)} = {c_\mathrm{V}}^{\left(\nu_{\mathrm{V,a}}-\nu_{\mathrm{V,c}}\right)} {c_\mathrm{h}}^{\left(\left(\nu_{\mathrm{h,a}}-\nu_{\mathrm{h,c}}\right)-\left(\nu_{\mathrm{e,a}}-\nu_{\mathrm{e,c}}\right)\right)} {p_{\mathrm{O}_2}}^{\left(\nu_{\mathrm{p,a}}-\nu_{\mathrm{p,c}}\right)} . \tag{4.70}$$

This has to be in accordance with the mass action law for the oxygen incorporation. With $K_\mathrm{ox}' = {K_\mathrm{ox}}^2 \frac{{c_\mathrm{Fe}}^4}{{c_\mathrm{Ox}}^2}$ and constant c_Fe and c_Ox we can write

$$\left(K_\mathrm{ox}'\right)^n = \left(\frac{{c_\mathrm{h}}^4}{p_{\mathrm{O}_2} {c_\mathrm{V}}^2}\right)^n . \tag{4.71}$$

Actually, in the mass action law n can still be chosen arbitrarily, and in equation (4.21) $n = 0.5$ was used (with still variable concentrations c_Ox and c_Fe). However, n becomes well defined by the equivalence of equations (4.70) and (4.71), which requires

$$\nu_{\mathrm{V,a}} - \nu_{\mathrm{V,c}} = -2n \tag{4.72}$$

$$\left(\nu_{\mathrm{h,a}} - \nu_{\mathrm{e,a}}\right) - \left(\nu_{\mathrm{h,c}} - \nu_{\mathrm{e,c}}\right) = \quad 4n \tag{4.73}$$

$$\nu_{\mathrm{p,a}} - \nu_{\mathrm{p,c}} = -n . \tag{4.74}$$

For simple mechanisms, we have $\nu_{\mathrm{p,a}} = 0$ and then n is simply the cathodic reaction order with respect to the oxygen partial pressure $\nu_{\mathrm{p,c}}$, i.e. 0.5 for atomic or 1 for molecular mechanisms. Furthermore, from equations (4.69) and (4.71) we get

$$\frac{\partial \ln K_\mathrm{ox}'}{\partial \mu_{\mathrm{O}_2}} = 4\frac{\partial \ln c_\mathrm{h}}{\partial \mu_{\mathrm{O}_2}} - 2\frac{\partial \ln c_\mathrm{V}}{\partial \mu_{\mathrm{O}_2}} - \frac{\partial \ln p_{\mathrm{O}_2}}{\partial \mu_{\mathrm{O}_2}} = 0 \tag{4.75}$$

$$\frac{\partial \ln K_\mathrm{i}'}{\partial \mu_{\mathrm{O}_2}} = \frac{\partial \ln c_\mathrm{h}}{\partial \mu_{\mathrm{O}_2}} + \frac{\partial \ln c_\mathrm{e}}{\partial \mu_{\mathrm{O}_2}} = 0 . \tag{4.76}$$

Equations (4.75) and (4.76) imply

$$\frac{\partial \ln c_\mathrm{V}}{\partial \mu_{\mathrm{O}_2}} = 2\frac{\partial \ln c_\mathrm{h}}{\partial \mu_{\mathrm{O}_2}} - \frac{1}{2kT} \tag{4.77}$$

$$\frac{\partial \ln c_\mathrm{e}}{\partial \mu_{\mathrm{O}_2}} = -\frac{\partial \ln c_\mathrm{h}}{\partial \mu_{\mathrm{O}_2}} . \tag{4.78}$$

4.6.1 Partial pressure dependence

From equations (4.66) and (4.67) we can deduce slopes according to

$$\frac{\partial \ln j_\mathrm{a}}{\partial \ln p_{\mathrm{O}_2}} = \frac{\partial \ln j_\mathrm{a}}{\partial \mu_{\mathrm{O}_2}} \frac{\partial \mu_{\mathrm{O}_2}}{\partial \ln p_{\mathrm{O}_2}} = kT \left(\nu_{\mathrm{V,a}} \frac{\partial \ln c_\mathrm{V}}{\partial \mu_{\mathrm{O}_2}} + \nu_{\mathrm{h,a}} \frac{\partial \ln c_\mathrm{h}}{\partial \mu_{\mathrm{O}_2}} + \nu_{\mathrm{e,a}} \frac{\partial \ln c_\mathrm{e}}{\partial \mu_{\mathrm{O}_2}} + \nu_{\mathrm{p,a}} \frac{1}{kT} \right) \tag{4.79}$$

$$\frac{\partial \ln j_\mathrm{c}}{\partial \ln p_{\mathrm{O}_2}} = \frac{\partial \ln j_\mathrm{c}}{\partial \mu_{\mathrm{O}_2}} \frac{\partial \mu_{\mathrm{O}_2}}{\partial \ln p_{\mathrm{O}_2}} = kT \left(\nu_{\mathrm{V,c}} \frac{\partial \ln c_\mathrm{V}}{\partial \mu_{\mathrm{O}_2}} + \nu_{\mathrm{h,c}} \frac{\partial \ln c_\mathrm{h}}{\partial \mu_{\mathrm{O}_2}} + \nu_{\mathrm{e,c}} \frac{\partial \ln c_\mathrm{e}}{\partial \mu_{\mathrm{O}_2}} + \nu_{\mathrm{p,c}} \frac{1}{kT} \right). \tag{4.80}$$

Combining equations (4.77) to (4.80) gives

$$\frac{\partial \ln j_\mathrm{a}}{\partial \ln p_{\mathrm{O}_2}} = kT \left(\nu_{\mathrm{h,a}} - \nu_{\mathrm{e,a}} + 2\nu_{\mathrm{V,a}} \right) \frac{\partial \ln c_\mathrm{h}}{\partial \mu_{\mathrm{O}_2}} - \frac{1}{2}\nu_{\mathrm{V,a}} + \nu_{\mathrm{p,a}} = q_\mathrm{a} \tag{4.81}$$

$$\frac{\partial \ln j_\mathrm{c}}{\partial \ln p_{\mathrm{O}_2}} = kT \left(\nu_{\mathrm{h,c}} - \nu_{\mathrm{e,c}} + 2\nu_{\mathrm{V,c}} \right) \frac{\partial \ln c_\mathrm{h}}{\partial \mu_{\mathrm{O}_2}} - \frac{1}{2}\nu_{\mathrm{V,c}} + \nu_{\mathrm{p,c}} = q_\mathrm{c}\,. \tag{4.82}$$

Symbols q_a and q_c denote the empirical power law exponents with respect to p_{O_2}. Including equations (4.72) to (4.74) into these considerations shows that $q_\mathrm{a} = q_\mathrm{c}$. Thus, for a given overpotential the partial pressure dependence is the same for the anodic and cathodic reaction, it is only a function of the oxygen partial pressure itself. Consequently, this is also the partial pressure dependence of the net current density at this overpotential and the p_{O_2} dependence of the exchange current density for equilibrium. Please note: Despite their identical p_{O_2} dependences for a given overpotential, j_a and j_c usually differ strongly in their absolute value, unless close to equilibrium. Hence, mostly only one of the two determines the net current density. In figures 4.10a and 4.10b the exponents of the p_{O_2} dependence of anodic and cathodic currents are shown as a function of p_{O_2} and η for the atomic and molecular mechanism without site restriction.

Actually, the slope $\frac{\partial \ln j}{\partial \ln p_{\mathrm{O}_2}}$ only depends on μ_{O_2}, which is also visible when comparing these p_{O_2} dependencies with the defect concentrations displayed in figure 4.11. Two defect regimes can be distinguished: At low p_{O_2} and negative overpotential (resulting in low μ_{O_2}) electron holes are the minority charge carrier and thus the p_{O_2} dependencies are determined by the electron hole reaction orders of the specific mechanisms. At high p_{O_2} and positive overpotentials (high μ_{O_2}) oxygen vacancies are the minority and consequently the p_{O_2} dependence of the current density depends on the reaction orders of oxygen vacancies. The equivalence of the p_{O_2} dependence of cathodic and anodic currents also means that any measured difference in the p_{O_2} dependence for anodic and cathodic voltages is simply caused by different regimes in the Brouwer diagram (i.e. different p_{O_2}). In other words, p_{O_2} dependencies of j change, when the current-voltage curves cross the colour front line in figure 4.11.

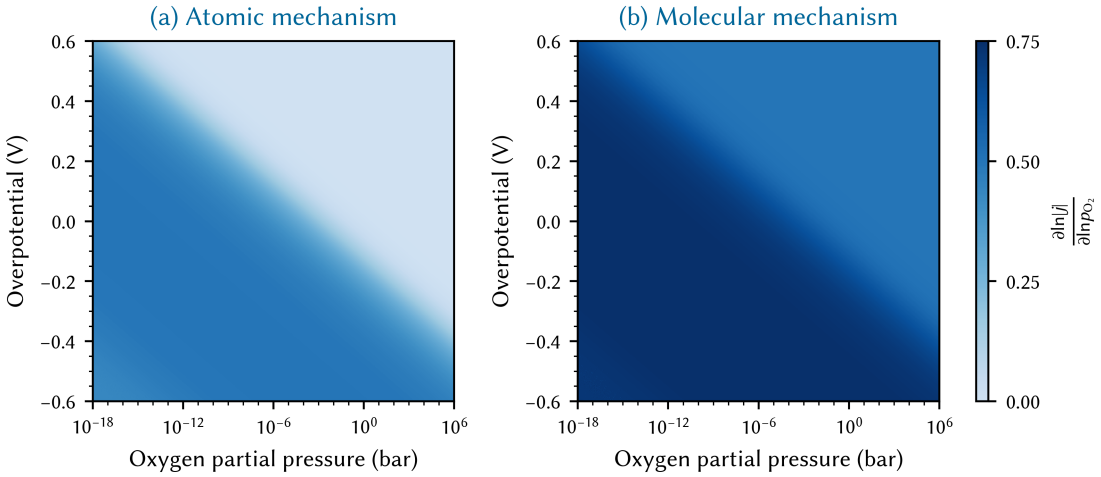

Figure 4.10: Partial pressure dependency of the current-density for the atomic mechanism discussed in section 4.4 (a) and the molecular mechanism in section 4.5 (b) as a function of partial pressure and overpotential.

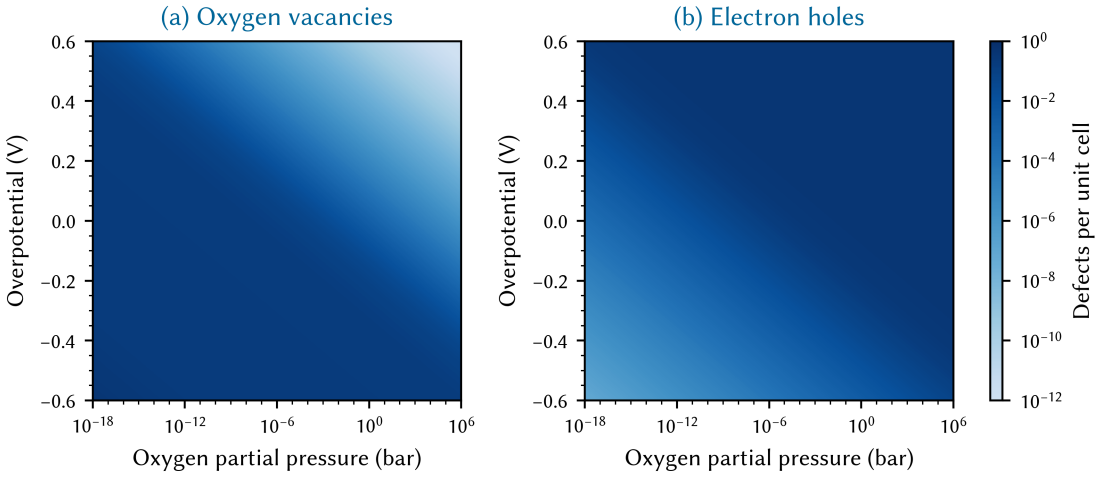

Figure 4.11: Extended LSF Brouwer diagram: Oxygen vacancy (a) and electron hole (b) concentrations as a function of partial pressure and overpotential.

4.6.2 Tafel slopes

From equations (4.66) and (4.67) we get

$$\begin{aligned}\frac{\partial \ln j_\mathrm{a}}{\partial \eta} &= \nu_{\mathrm{V,a}}\frac{\partial \ln c_\mathrm{V}}{\partial \eta} + \nu_{\mathrm{h,a}}\frac{\partial \ln c_\mathrm{h}}{\partial \eta} + \nu_{\mathrm{e,a}}\frac{\partial \ln c_\mathrm{e}}{\partial \eta} + \nu_{\mathrm{p,a}}\frac{\partial \ln p_{\mathrm{O}_2}}{\partial \eta} \\ &= \frac{\partial \mu_{\mathrm{O}_2}}{\partial \eta}\left(\nu_{\mathrm{V,a}}\frac{\partial \ln c_\mathrm{V}}{\partial \mu_{\mathrm{O}_2}} + \nu_{\mathrm{h,a}}\frac{\partial \ln c_\mathrm{h}}{\partial \mu_{\mathrm{O}_2}} + \nu_{\mathrm{e,a}}\frac{\partial \ln c_\mathrm{e}}{\partial \mu_{\mathrm{O}_2}}\right) \\ &= 4e\left(\nu_{\mathrm{V,a}}\frac{\partial \ln c_\mathrm{V}}{\partial \mu_{\mathrm{O}_2}} + \nu_{\mathrm{h,a}}\frac{\partial \ln c_\mathrm{h}}{\partial \mu_{\mathrm{O}_2}} + \nu_{\mathrm{e,a}}\frac{\partial \ln c_\mathrm{e}}{\partial \mu_{\mathrm{O}_2}}\right)\end{aligned} \tag{4.83}$$

and

$$\begin{aligned}\frac{\partial \ln j_\mathrm{c}}{\partial \eta} &= \nu_{\mathrm{V,c}}\frac{\partial \ln c_\mathrm{V}}{\partial \eta} + \nu_{\mathrm{h,c}}\frac{\partial \ln c_\mathrm{h}}{\partial \eta} + \nu_{\mathrm{e,c}}\frac{\partial \ln c_\mathrm{e}}{\partial \eta} + \nu_{\mathrm{p,c}}\frac{\partial \ln p_{\mathrm{O}_2}}{\partial \eta} \\ &= \frac{\partial \mu_{\mathrm{O}_2}}{\partial \eta}\left(\nu_{\mathrm{V,c}}\frac{\partial \ln c_\mathrm{V}}{\partial \mu_{\mathrm{O}_2}} + \nu_{\mathrm{h,c}}\frac{\partial \ln c_\mathrm{h}}{\partial \mu_{\mathrm{O}_2}} + \nu_{\mathrm{e,c}}\frac{\partial \ln c_\mathrm{e}}{\partial \mu_{\mathrm{O}_2}}\right) \\ &= 4e\left(\nu_{\mathrm{V,c}}\frac{\partial \ln c_\mathrm{V}}{\partial \mu_{\mathrm{O}_2}} + \nu_{\mathrm{h,c}}\frac{\partial \ln c_\mathrm{h}}{\partial \mu_{\mathrm{O}_2}} + \nu_{\mathrm{e,c}}\frac{\partial \ln c_\mathrm{e}}{\partial \mu_{\mathrm{O}_2}}\right).\end{aligned} \tag{4.84}$$

By combining equations (4.77), (4.78), (4.83) and (4.84) we get

$$\frac{\partial \ln j_\mathrm{a}}{\partial \eta} = 4e\frac{\partial \ln c_\mathrm{h}}{\partial \mu_{\mathrm{O}_2}}\left(\nu_{\mathrm{h,a}} - \nu_{\mathrm{e,a}} + 2\nu_{\mathrm{V,a}}\right) - \frac{2e}{kT}\nu_{\mathrm{V,a}} \tag{4.85}$$

$$\frac{\partial \ln j_\mathrm{c}}{\partial \eta} = 4e\frac{\partial \ln c_\mathrm{h}}{\partial \mu_{\mathrm{O}_2}}\left(\nu_{\mathrm{h,c}} - \nu_{\mathrm{e,c}} + 2\nu_{\mathrm{V,c}}\right) - \frac{2e}{kT}\nu_{\mathrm{V,c}}\,. \tag{4.86}$$

From equations (4.72) to (4.74) and (4.86) we thus obtain

$$\frac{\partial \ln j_\mathrm{c}}{\partial \eta} = 4e\frac{\partial \ln c_\mathrm{h}}{\partial \mu_{\mathrm{O}_2}}\left(\nu_{\mathrm{h,a}} - \nu_{\mathrm{e,a}} + 2\nu_{\mathrm{V,a}}\right) - \frac{2e}{kT}\left(\nu_{\mathrm{V,a}} + 2n\right). \tag{4.87}$$

Accordingly, for a given overpotential the Tafel-slopes of the anodic and cathodic currents differ by $\frac{4en}{kT}$. This simply reflects the fact that for a changing overpotential the anodic and cathodic currents change in a different manner. Therefore, one of them always dominates sufficiently far from equilibrium. In each direction, however, the slope is still only a function of μ_{O_2}, irrespective of the parameter changing μ_{O_2} (p_{O_2} or η). An equivalent expression for the cathodic oxygen reduction current on Pr-doped ceria was derived by Chueh et al. in Ref. [49]. The generalized expressions (equations (4.85) and (4.87)) also show that the splitting

of Tafel slopes in three factors performed in the specific discussion, e.g. equation (4.54), is already a simplification. Those factors are still present in the generalized expressions but are complemented by additional terms.

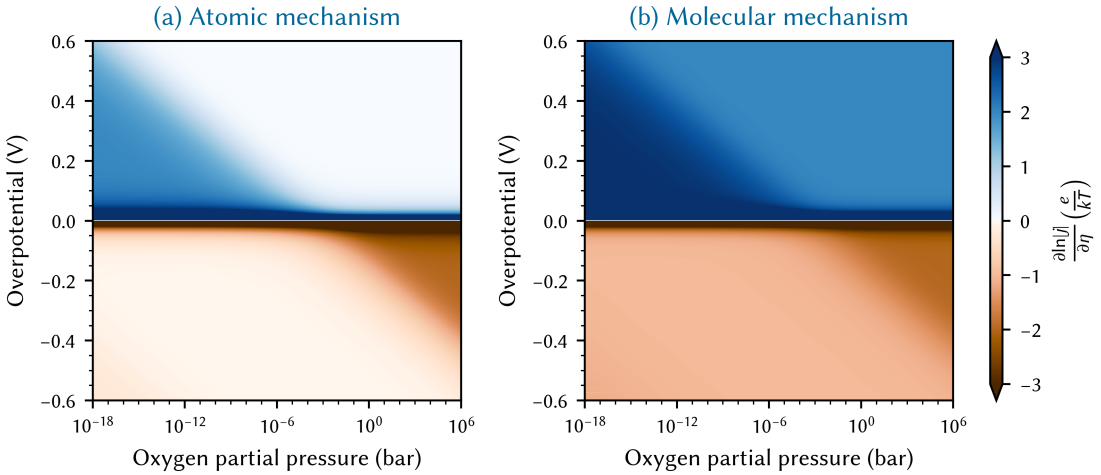

Figure 4.12: Tafel slopes for the atomic mechanism discussed in section 4.4 (a) and the molecular mechanism in section 4.5 (b) as a function of partial pressure and overpotential.

Figures 4.12a and 4.12b display the Tafel slopes of the two mechanisms discussed in sections 4.4 and 4.5 as function of partial pressure and overpotential. Comparing these to the LSF defect concentrations shown in figure 4.11 reveals two facts: First, two regimes can be distinguished, and these follow the minority charge carrier regimes in figure 4.11. At low p_{O_2} and negative overpotential (low μ_{O_2}) the Tafel slopes are determined by the reaction order of electron holes. At high μ_{O_2}, oxygen vacancies are in minority and the Tafel slopes depend on the reaction order of oxygen vacancies. Second, the Tafel slopes of the anodic and cathodic currents differ by $\frac{2e}{kT}$ and $\frac{4e}{kT}$ respectively, over the entire p_{O_2} and η range, as long as we stay in one defect regime. This also implies that knowledge of the nature of the oxygen species in the rate determining step (atomic or molecular) can be obtained from the anodic and cathodic Tafel slopes, provided both are still in the same minority charge carrier regime. A difference of $\frac{4e}{kT}$, for example, results from an anodic slope of $\frac{3e}{kT}$ and a cathodic slope of $-\frac{1e}{kT}$ and indicates a molecular species in the rate determining step. Hence, such a slope analysis of the current-voltage curves can be a simple but powerful approach for obtaining mechanistic information already without further detailed analysis of reaction models. However, one has to keep in mind that it works only if the defect regime does not change and thus, for example, not in figure 4.7b.

4.6.3 Oxygen exchange reaction resistance

Lastly, we briefly discuss the oxygen exchange resistance predicted by this model. The area specific reaction resistance is given by the inverse derivative of the current density with respect to the overpotential:

$$R = \frac{\partial \eta}{\partial j} = \left(\frac{\partial j}{\partial \eta}\right)^{-1} . \tag{4.88}$$

For the sake of simplicity, we limit ourselves to the simple case of equilibrium conditions, i.e. at $\eta = 0$. Then, equation (4.88) leads to

$$R^{\mathrm{eq}} = \frac{kT}{4enj^0} . \tag{4.89}$$

The detailed derivation of this expression is given in section 4.A. Equation (4.89) corresponds to the charge transfer resistance for multi-step single electron transfer processes in aqueous electrochemistry described in Ref. [75]. However, the physical meaning behind these expressions is very different. In the aqueous electrochemical system considered in Ref [75], the overpotential acts by modifying activation barriers for a single electron transfer and also by changing intermediate species concentrations, whereas in our model of MIEC|gas interfaces, the overpotential acts only by changing defect concentrations.

Equation (4.89), however, also shows that that the oxygen exchange current density cannot simply be deduced from the oxygen exchange resistance measured by impedance spectroscopy R^{eq}. Rather, knowledge of n and thus of the mechanism (atomic or molecular oxygen species in the rate limiting step) is required. Conversely, accurate extrapolation of j^0 from Tafel plots and comparison with measured R^{eq} from impedance spectra can allow mechanistic conclusions by determining n. Moreover, equation (4.89) questions the simple approach often used for comparing resistances of impedance spectra with tracer exchange data obtained on the same material.[24] There, the oxygen exchange coefficient k^* is a measure of the oxygen exchange current density j^0 with

$$j^0 = 2ek^*c_{\mathrm{O}} \tag{4.90}$$

and c_{O} denoting the oxygen site concentration. A correct calculation of the corresponding exchange resistance R^* (for the sake of comparison with the electrically measured R^{eq}) should thus use the equation

$$R^* = \frac{1}{2n}\frac{kT}{4e^2k^*c_{\mathrm{O}}} . \tag{4.91}$$

The factor of $2n$ (1 or 2) is usually neglected so far, which is problematic for molecular oxygen in the rate determining step.

4.7 Conclusion

The kinetics of the oxygen exchange reactions are quantified by rate equations including the relevant acting species, i.e. adsorbates (or the gas phase determining the adsorbates) and defects involved in oxygen reduction or oxygen evolution. Any change of surface potential is neglected, hence reaction rates are purely defect controlled. The defect concentrations are defined by μ_{O_2}, which itself depends on p_{O_2} and overpotential, provided that the oxygen surface exchange reaction limits the overall reaction rate. The forward and backward rates, i.e. anodic and cathodic currents thus depend on the overpotential which varies defect concentrations. The dependence of the defect concentrations on overpotential (and p_{O_2}) is given by the Brouwer diagram. Specific p_{O_2} and η dependencies of the anodic, cathodic and net current densities can be calculated for a given rate equation with reaction orders for defects and p_{O_2} (via adsorbates) and a given Brouwer diagram. This is exemplified for LSF and two reaction mechanisms, one with atomic oxygen in the rate determining step and one with molecular oxygen species. Also, adsorption site restriction is considered in separate calculations.

These calculations revealed that frequently exponential j-η curves result, with Tafel slopes given by three factors, one for the reaction order(s) of the defects in the rate equation, one from the slope of defect concentrations in the Brouwer diagram, and one from the Nernst relation between η and μ_{O_2}. Hence, the slope does not reveal the number of electrons in the rate determining step. If the relevant defect concentrations are constant within the considered range of the Brouwer diagram, a Tafel slope of 0 and thus limiting currents result, despite absence of transport limitation. Since the gas p_{O_2} not only modifies adsorbate concentrations but also defect concentrations, the exponents q of empirical power laws $j \propto {p_{O_2}}^q$ have often non-trivial meanings. They depend on the species in the rate limiting step (atomic or molecular oxygen) but also on the reaction orders of defects and on their p_{O_2} slope in the Brouwer diagram. For example, in the molecular mechanism considered, the oxygen exchange current density scales with ${p_{O_2}}^{0.75}$ to ${p_{O_2}}^{0.5}$, depending on p_{O_2}. For the atomic mechanism ${p_{O_2}}^{0.5}$ to ${p_{O_2}}^{0.0}$ was found.

General equations for the partial pressure and overpotential dependencies are derived for anodic and cathodic currents. Those show that for a given overpotential both anodic and cathodic currents show the same p_{O_2} dependency. The Tafel slopes, on the other hand, differ by $4ne/kT$ and measured slope differences can thus give valuable information on the mechanism ($n = 1$ or $n = 1/2$ indicating molecular or atomic oxygen in the rate determining step). Finally, a relation is deduced between the slope of a current-voltage curve close to equilibrium, e.g. measured by impedance spectroscopy, and the exchange current density. It is shown

that knowledge of both values can also give mechanistic information on molecular or atomic oxygen species. Moreover, an inconsistency in the standard procedure of comparing tracer exchange coefficients and electrical surface exchange resistances was identified.

Appendix 4.A Derivation of the equilibrium exchange resistance

Assuming $\Delta\chi = 0$ and neglecting again $O_O^\times$ and $Fe_{Fe}^\times$ as defect species, we can rewrite equation (4.8) explicitly with oxygen vacancies, electron holes and electrons as relevant defect species:

$$j = j^0\left[\left(\frac{c_V}{c_V^{eq}}\right)^{\nu_{V,a}}\left(\frac{c_h}{c_h^{eq}}\right)^{\nu_{h,a}}\left(\frac{c_e}{c_e^{eq}}\right)^{\nu_{e,a}} - \left(\frac{c_V}{c_V^{eq}}\right)^{\nu_{V,c}}\left(\frac{c_h}{c_h^{eq}}\right)^{\nu_{h,c}}\left(\frac{c_e}{c_e^{eq}}\right)^{\nu_{e,c}}\right]. \tag{4.92}$$

Taking the the derivative of the current density with respect to the overpotential gives

$$\begin{aligned}
\frac{1}{R} = \frac{\partial j}{\partial \eta} = \frac{\partial}{\partial \eta}\Bigg[j^0\Bigg[\left(\frac{c_V}{c_V^{eq}}\right)^{\nu_{V,a}}\left(\frac{c_h}{c_h^{eq}}\right)^{\nu_{h,a}}\left(\frac{c_e}{c_e^{eq}}\right)^{\nu_{e,a}} - \left(\frac{c_V}{c_V^{eq}}\right)^{\nu_{V,c}}\left(\frac{c_h}{c_h^{eq}}\right)^{\nu_{h,c}}\left(\frac{c_e}{c_e^{eq}}\right)^{\nu_{e,c}}\Bigg]\Bigg] \\
= j^0\Bigg[\left(\frac{c_h}{c_h^{eq}}\right)^{\nu_{h,a}}\left(\frac{c_e}{c_e^{eq}}\right)^{\nu_{e,a}}\left(\frac{c_V}{c_V^{eq}}\right)^{\nu_{V,a}-1}\nu_{V,a}\frac{1}{c_V^{eq}}\frac{\partial c_V}{\partial \eta} \\
+ \left(\frac{c_V}{c_V^{eq}}\right)^{\nu_{V,a}}\left(\frac{c_e}{c_e^{eq}}\right)^{\nu_{e,a}}\left(\frac{c_h}{c_h^{eq}}\right)^{\nu_{h,a}-1}\nu_{h,a}\frac{1}{c_h^{eq}}\frac{\partial c_h}{\partial \eta} \\
+ \left(\frac{c_V}{c_V^{eq}}\right)^{\nu_{V,a}}\left(\frac{c_h}{c_h^{eq}}\right)^{\nu_{h,a}}\left(\frac{c_e}{c_e^{eq}}\right)^{\nu_{e,a}-1}\nu_{e,a}\frac{1}{c_e^{eq}}\frac{\partial c_e}{\partial \eta} \\
- \left(\frac{c_h}{c_h^{eq}}\right)^{\nu_{h,c}}\left(\frac{c_e}{c_e^{eq}}\right)^{\nu_{e,c}}\left(\frac{c_V}{c_V^{eq}}\right)^{\nu_{V,c}-1}\nu_{V,c}\frac{1}{c_V^{eq}}\frac{\partial c_V}{\partial \eta} \\
- \left(\frac{c_V}{c_V^{eq}}\right)^{\nu_{V,c}}\left(\frac{c_e}{c_e^{eq}}\right)^{\nu_{e,c}}\left(\frac{c_h}{c_h^{eq}}\right)^{\nu_{h,c}-1}\nu_{h,c}\frac{1}{c_h^{eq}}\frac{\partial c_h}{\partial \eta} \\
- \left(\frac{c_V}{c_V^{eq}}\right)^{\nu_{V,c}}\left(\frac{c_h}{c_h^{eq}}\right)^{\nu_{h,c}}\left(\frac{c_e}{c_e^{eq}}\right)^{\nu_{e,c}-1}\nu_{e,c}\frac{1}{c_e^{eq}}\frac{\partial c_e}{\partial \eta}\Bigg].
\end{aligned} \tag{4.93}$$

Since for any defect D

$$\frac{\partial c_D}{\partial \eta} = c_D\frac{\partial \ln c_D}{\partial \eta} = c_D\frac{\partial \ln c_D}{\partial \mu_{O_2}}\frac{\partial \mu_{O_2}}{\partial \eta} = 4ec_D\frac{\partial \ln c_D}{\partial \mu_{O_2}}, \tag{4.94}$$

equation (4.93) can be simplified to

$$\frac{1}{R} = 4ej^0\left[\left(\frac{c_\mathrm{V}}{c_\mathrm{V}^\mathrm{eq}}\right)^{\nu_{\mathrm{V,a}}}\left(\frac{c_\mathrm{h}}{c_\mathrm{h}^\mathrm{eq}}\right)^{\nu_{\mathrm{h,a}}}\left(\frac{c_\mathrm{e}}{c_\mathrm{e}^\mathrm{eq}}\right)^{\nu_{\mathrm{e,a}}}\left(\nu_{\mathrm{V,a}}\frac{\partial \ln c_\mathrm{V}}{\partial \mu_{\mathrm{O}_2}} + \nu_{\mathrm{h,a}}\frac{\partial \ln c_\mathrm{h}}{\partial \mu_{\mathrm{O}_2}} + \nu_{\mathrm{e,a}}\frac{\partial \ln c_\mathrm{e}}{\partial \mu_{\mathrm{O}_2}}\right) - \left(\frac{c_\mathrm{V}}{c_\mathrm{V}^\mathrm{eq}}\right)^{\nu_{\mathrm{V,c}}}\left(\frac{c_\mathrm{h}}{c_\mathrm{h}^\mathrm{eq}}\right)^{\nu_{\mathrm{h,c}}}\left(\frac{c_\mathrm{e}}{c_\mathrm{e}^\mathrm{eq}}\right)^{\nu_{\mathrm{e,c}}}\left(\nu_{\mathrm{V,c}}\frac{\partial \ln c_\mathrm{V}}{\partial \mu_{\mathrm{O}_2}} + \nu_{\mathrm{h,c}}\frac{\partial \ln c_\mathrm{h}}{\partial \mu_{\mathrm{O}_2}} + \nu_{\mathrm{e,c}}\frac{\partial \ln c_\mathrm{e}}{\partial \mu_{\mathrm{O}_2}}\right)\right]. \tag{4.95}$$

Combining equations (4.77), (4.78) and (4.95) gives

$$\frac{1}{R} = 4ej^0\left[\left(\frac{c_\mathrm{V}}{c_\mathrm{V}^\mathrm{eq}}\right)^{\nu_{\mathrm{V,a}}}\left(\frac{c_\mathrm{h}}{c_\mathrm{h}^\mathrm{eq}}\right)^{\nu_{\mathrm{h,a}}}\left(\frac{c_\mathrm{e}}{c_\mathrm{e}^\mathrm{eq}}\right)^{\nu_{\mathrm{e,a}}}\left(\left(2\nu_{\mathrm{V,a}} + \nu_{\mathrm{h,a}} - \nu_{\mathrm{e,a}}\right)\frac{\partial \ln c_\mathrm{h}}{\partial \mu_{\mathrm{O}_2}} - \frac{\nu_{\mathrm{V,a}}}{2kT}\right) - \left(\frac{c_\mathrm{V}}{c_\mathrm{V}^\mathrm{eq}}\right)^{\nu_{\mathrm{V,c}}}\left(\frac{c_\mathrm{h}}{c_\mathrm{h}^\mathrm{eq}}\right)^{\nu_{\mathrm{h,c}}}\left(\frac{c_\mathrm{e}}{c_\mathrm{e}^\mathrm{eq}}\right)^{\nu_{\mathrm{e,c}}}\left(\left(2\nu_{\mathrm{V,c}} + \nu_{\mathrm{h,c}} - \nu_{\mathrm{e,c}}\right)\frac{\partial \ln c_\mathrm{h}}{\partial \mu_{\mathrm{O}_2}} - \frac{\nu_{\mathrm{V,c}}}{2kT}\right)\right]. \tag{4.96}$$

Including relations between anodic and cathodic reaction orders (equations (4.72) and (4.73)) yields

$$\frac{1}{R} = 4ej^0\left[\left(\frac{c_\mathrm{V}}{c_\mathrm{V}^\mathrm{eq}}\right)^{\nu_{\mathrm{V,a}}}\left(\frac{c_\mathrm{h}}{c_\mathrm{h}^\mathrm{eq}}\right)^{\nu_{\mathrm{h,a}}}\left(\frac{c_\mathrm{e}}{c_\mathrm{e}^\mathrm{eq}}\right)^{\nu_{\mathrm{e,a}}}\left(\left(2\nu_{\mathrm{V,a}} + \nu_{\mathrm{h,a}} - \nu_{\mathrm{e,a}}\right)\frac{\partial \ln c_\mathrm{h}}{\partial \mu_{\mathrm{O}_2}} - \frac{\nu_{\mathrm{V,a}}}{2kT}\right) - \left(\frac{c_\mathrm{V}}{c_\mathrm{V}^\mathrm{eq}}\right)^{\nu_{\mathrm{V,c}}}\left(\frac{c_\mathrm{h}}{c_\mathrm{h}^\mathrm{eq}}\right)^{\nu_{\mathrm{h,c}}}\left(\frac{c_\mathrm{e}}{c_\mathrm{e}^\mathrm{eq}}\right)^{\nu_{\mathrm{e,c}}}\left(\left(2\nu_{\mathrm{V,a}} + \nu_{\mathrm{h,a}} - \nu_{\mathrm{e,a}}\right)\frac{\partial \ln c_\mathrm{h}}{\partial \mu_{\mathrm{O}_2}} - \frac{\nu_{\mathrm{V,a}} + 2n}{2kT}\right)\right]. \tag{4.97}$$

At zero overpotential the defect concentrations are equal to their equilibrium values and thus

$$\begin{aligned}\frac{1}{R^\mathrm{eq}} &= 4ej^0\left[\left(2\nu_{\mathrm{V,a}} + \nu_{\mathrm{h,a}} - \nu_{\mathrm{e,a}}\right)\frac{\partial \ln c_\mathrm{h}}{\partial \mu_{\mathrm{O}_2}} - \frac{\nu_{\mathrm{V,a}}}{2kT} - \left(2\nu_{\mathrm{V,a}} + \nu_{\mathrm{h,a}} - \nu_{\mathrm{e,a}}\right)\frac{\partial \ln c_\mathrm{h}}{\partial \mu_{\mathrm{O}_2}} + \frac{\nu_{\mathrm{V,a}} + 2n}{2kT}\right] \\ &= \frac{4nej^0}{kT}.\end{aligned} \tag{4.98}$$

5 High oxygen exchange activity of pristine LSF films and its degradation

5.1 Introduction

Oxygen exchange kinetics of perovskites is often investigated by electrochemical methods such as impedance spectroscopy[13,20,53] or conductivity relaxation[1] and isotope exchange experiments.[3] However, reported values for kinetic parameters (i.e. oxygen exchange coefficients) vary widely, often by several orders of magnitude. Additionally, many of those materials also suffer from limited long term stability, i.e. degradation of the electrode kinetics, which not only hampers industrial application but also complicates basic research as it convolutes the material's inherent oxygen exchange kinetics with the influence of thermal and chemical history.

In order to understand the reasons behind degradation and varying properties, the surface chemistry of such perovskites has been studied by various surface sensitive analytical techniques such as X-ray photoelectron spectroscopy (XPS),[15,22,54] secondary ion mass spectrometry (SIMS)[3,81] or low energy ion scattering (LEIS).[5] Sr enrichment on the surface was found to be responsible for a decrease of electrode kinetics over time, and recent studies could directly observe the adverse effect of Sr decoration on MIEC surfaces.[7] Furthermore, various catalyst poisons such as Si, SO_2 or Cr were found to cause increased degradation of the surface resistance, especially in the presence of humidity.[1,22,55,56]

Moreover, in-situ impedance spectroscopy during electrode deposition offers great potential for an accurate investigation of MIEC thin film electrochemical properties.[7] Impedance measurements inside the pulsed laser deposition vacuum chamber immediately after thin film deposition give access to the kinetics of the electrode in its pristine state, and thus reflect the inherent material kinetics. By exposing the freshly deposited sample to potentially degrading environments inside the deposition chamber and monitoring the impedance, their effect can be investigated in a selective and controlled way. Direct and real time monitoring of the impedance response to potential degradation sources also allows separating their true effect on the oxygen exchange kinetics from effects due to the often quite substantial sample variation found in ex-situ studies.

This approach of in-situ impedance spectroscopy during pulsed laser deposition (IPLD) was used to investigate the oxygen exchange on $La_{0.6}Sr_{0.4}FeO_{3-\delta}$ thin films. Exposing the pristine films to different conditions and comparing the results with ex-situ measured properties revealed the inherent LSF properties in the pristine state and their striking variation depending on the sample history. Additional surface chemistry analysis (XPS) indicated chemical reasons behind the kinetic changes.

5.2 Experimental

5.2.1 Sample preparation

Yttria stabilized zirconia (YSZ) single crystals ($5 \times 5 \times 0.5\,mm^3$ in (100) orientation), polished on the flat sides, were used as electrolyte substrates. Platinum current collector grids (35/15 µm mesh/strip width, 100 nm thickness) were prepared on both sides by lift-off photolithography and magnetron sputtering (BAL-TEC MED 020). A 5 nm Ti layer was deposited between YSZ and Pt to improve adhesion of the Pt grid. On one square surface, a low resistive, porous $La_{0.6}Sr_{0.4}CoO_{3-\delta}$ (LSC) thin film (approximately 300 nm) counter electrode was deposited on top of the Pt grid by pulsed laser deposition (PLD).[4] Pt and LSC deposited on the samples edges were removed by grinding to eliminate parasitic current paths. A dense $La_{0.6}Sr_{0.4}FeO_{3-\delta}$ (LSF) working electrode was deposited on the other side on top of the Pt grid and immediately after this deposition the in-situ EIS measurements were started, see section 5.2.2. Additionally, symmetrical samples with LSF thin films deposited on both sides were prepared for ex-situ characterization.

PLD thin film deposition was done using a KrF excimer laser (Complex Pro 201F, 248 nm). Deposition parameters for the LSC counter electrodes and LSF working electrodes are listed in table 5.1. Figure 5.1 shows a sketch of the sample geometry and a cross-section of a dense LSF film. PLD targets were prepared by Pechini syntheses. La_2O_3, $SrCO_3$ and Co/Fe (all Sigma Aldrich, 99.995 %) were dissolved in nitric acid and citric acid was added in a molar ratio of 1 with respect to the total amount of cations. The solution was then heated and evaporated until self ignition and combustion took place, and the obtained powder was calcined in air at 850 °C for 12 h. Targets were pressed isostatically (150 MPa) and sintered in air at 1200 °C for 12 h. Phase purity of the targets was confirmed by X-ray diffraction.

Table 5.1: Deposition parameters for porous LSC and dense LSF thin films

	LSC	LSF
Substrate temperature	450 °C	600 °C
Oxygen pressure	0.4 mbar	0.04 mbar
Substrate to target distance	5 cm	6 cm
Laser pulses	9000	9000
Laser fluence	2 J cm^{-2}	2 J cm^{-2}
Pulse frequency	5 Hz	5 Hz
Film thickness	300 nm	150 nm

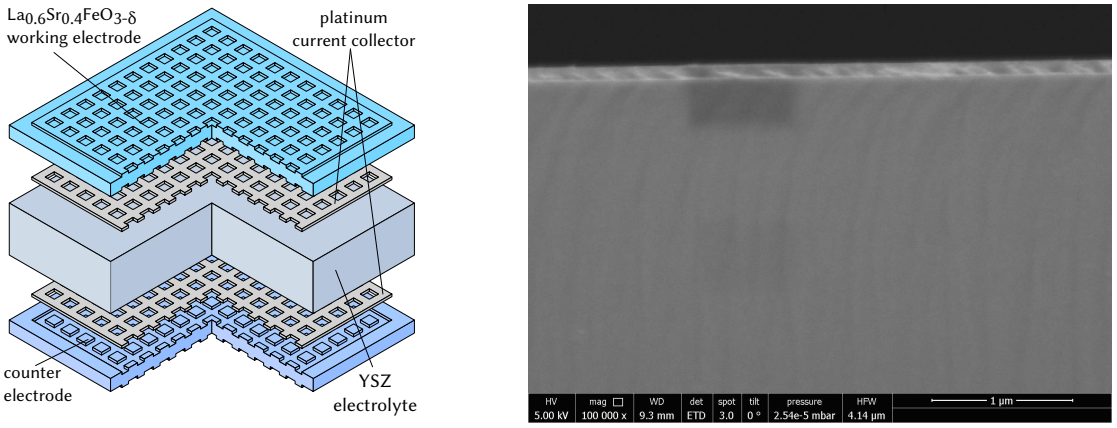

(a) Sample geometry

(b) Film cross section

Figure 5.1: (a) Sketch of the sample geometry used for impedance spectroscopy. (b) Cross section secondary electron microscopy image of an LSF film on top of the YSZ substrate.

5.2.2 In-situ impedance spectroscopy

Samples with Pt current collectors on both sides and a porous LSC counter electrode on one side were prepared as described in section 5.2.1. These were then mounted in the in-situ PLD setup displayed in figure 5.2a. A thin fused silica disk was placed between sample and heater to isolate the sample from the heater. The sample was placed on a platinum sheet to contact the counter electrode, and an alumina disk with a cut-out was used to hold the sample in position. A second thin alumina disk with a smaller cut-out was used as a mask to ensure that LSF is only deposited on a defined area on the flat surface of the substrate and to prevent deposition at the edges of the sample. The top side of the substrate was contacted on the Pt current collector grid via a platinum needle. Dense LSF thin film working electrodes were deposited onto the samples with the parameters described in table 5.1. Immediately after deposition the sample was characterized by impedance spectroscopy either at deposition p_{O_2} (0.04 mbar) or at

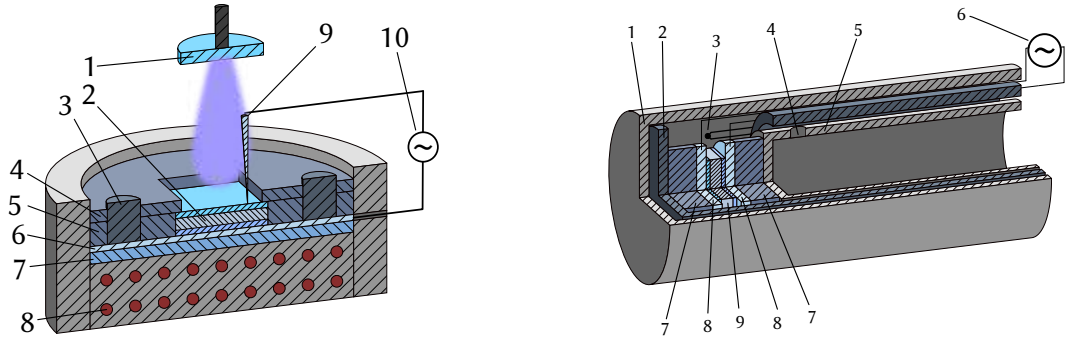

(a) In-situ setup **(b)** Ex-situ setup

Figure 5.2: (a) In-situ setup for impedance spectroscopy inside the PLD chamber, consisting of: ablation target (1), sample (2), alignment pins (3), alumina shadow mask (4), sample holder (5), Pt contact sheet (6), silica insulation disk (7), resistive heater (8), contacting needle (9), impedance analyser (10). (b) Ex-situ setup consisting of: Sealed outer tube (1), spring loaded middle tube (2), thermocouple (3), gas inlet (4), inner tube (5), impedance analyser (6), spacer (7), Pt contacting sheet (8), sample (9).

0.25 mbar or 1 mbar. If the p_{O_2} was adjusted, a change in temperature resulted due to modified heat transfer conditions. Hence, also the temperature as adjusted to reach again 600 °C. An ac voltage of 10 mV was used in impedance measurements with a frequency range of 1 MHz to 0.1 Hz and each frequency point was measured for at least one second or one period.

Time dependency To investigate the time dependency of the resistance degradation inside and outside the PLD chamber, LSF thin film electrodes were prepared and characterized by in-situ impedance spectroscopy as described above. Samples were then measured in an ex-situ setup (see section 5.2.3) for several hours. Afterwards, samples were transferred back to the deposition chamber, the PLD chamber was evacuated to 10^{-5} mbar, the sample was heated to measurement temperature, the p_{O_2} and temperature were adjusted and the impedance was again measured.

Investigating potential degradation sources After film deposition, impedance spectra were measured for 2 h to determine the electrode polarization resistance of the freshly deposited LSF films and estimate their degradation rate. Samples were then exposed to the different potentially degrading sources listed in table 5.2 for 2 h and afterwards impedance spectra were again measured for 2 h at deposition conditions. All these impedance measurements were performed in 0.04 mbar O_2 at 600 °C, except for the humidity test, which was done in 0.25 mbar O_2.

TABLE 5.2: Potential sources of resistance degradation investigated by exposing a freshly deposited LSF film inside the deposition chamber.

Abbreviation	Description
High p_{O_2}	Fill chamber with 50 mbar O_2 (Alphagaz, 99.995 %)
Amb. air	Fill chamber with 50 mbar ambient air
T-cycle	Cool sample to 25 °C and reheat in 0.04 mbar O_2 (15 °C min^{-1})
T-cycle in air	Cool sample to 25 °C and reheat in 1 bar ambient air (15 °C min^{-1})
Humidity	Add 6.25 µbar H_2O to the chamber, measured in 0.25 mbar O_2

5.2.3 Ex-situ impedance spectroscopy

Ex-situ impedance measurements were done in the setup shown in figure 5.2b. Electrodes were contacted by clamping the sample between two platinum sheets with additional Pt meshes in between for better contacting. The spring loaded middle tube ensured good contact by pressing the sample/contacting sheet stack against the fixed inner tube. The inner tube also served as a gas inlet close to the sample. An S-type thermocouple was placed close to the sample for temperature measurement. These setups were placed in an outer tube and sealed by a KF flange with a Viton O-ring sufficiently far from the hot zone of the tube furnace to remain at room temperature. Different measurement setups made from either fused silica or alumina were used.

5.2.4 XPS measurements

The surface chemistry of LSF films was investigated by X-ray photoelectron spectroscopy. Measurements were done on as-deposited samples as well as after 24 h of ex-situ impedance measurement at 600 °C in 0.25 mbar O_2. Additionally, samples were transferred back to the PLD chamber after ex-situ measurements, annealed in the PLD chamber for 4 h at 600 °C and then measured by XPS. Samples were transferred to the XPS measurement setup under Ar atmosphere. XPS measurements were carried out at room temperature in a UHV chamber by SPECS, Germany, using a monochromated Al K-alpha source (XRC-125 MF, SPECS) operated at 80 W, and an angle resolved photoelectron analyser (SPECS POHIBOS WAL), collecting photoelectrons at emission angles from 20 to 80° from the surface normal. Survey spectra were recorded at 100 eV analyser pass energy, and detailed spectra for peak fitting were recorded at 50 eV pass energy. Peak fitting and quantification was carried out with CasaXPS software, using S-shaped "Shirley" background functions, and compositional analysis was based on the

peak areas and Scofield cross sections.[82] Mixed Gaussian-Lorentzian peak shapes were used for the Sr surface and Sr bulk components. The Sr-3d 3/2 and Sr-3d 5/2 multiplet peaks were constrained to an energy difference of 1.7 eV, an area ratio of 2:3, and equal FWHM.

5.3 Results and discussion

5.3.1 Electrochemical characterization

Impedance analysis Figure 5.3 displays impedance spectra measured inside the PLD chamber (in-situ) and in the ex-situ setup for different oxygen partial pressures. All spectra exhibit a high frequency offset and a large semicircle at low frequency, additionally a small shoulder is visible in the intermediate frequency range. The high frequency intercept is mainly caused by the ionic transport resistance in the YSZ electrolyte and a small contribution from the wiring. After subtracting the resistance of the wiring, the corrected electrolyte resistance was used to determine and control the sample temperature based on the known ionic conductivity of YSZ.[83] The large semicircle is attributed to the oxygen exchange reactions at the working and counter electrode in parallel to their chemical capacitances, respectively.[13,57] Since the porous LSC counter electrode has much faster oxygen exchange kinetics, and thus a much lower polarization resistance, the low frequency impedance response of the cell is largely determined by the impedance of the dense LSF working electrode film.[7] The intermediate frequency shoulder can be attributed to an interfacial resistance and capacitance at the LSF|YSZ interface.[24] The resistance of this intermediate frequency feature contributes only marginally to the total electrode resistance. In the following, we therefore consider the entire electrode resistance, i.e. the sum of the small intermediate and the dominant low frequency resistance. The LSF surface above the current collector grid is inactive with respect to oxygen exchange due to the high in-plane oxygen ion transport resistances.[13,84] The electrode resistance was thus normalized to the LSF surface area above the YSZ, which is approximately 51 % of the total LSF surface area.

At the deposition pressure of 0.04 mbar O_2 an initial electrode polarization resistance of $(17.5 \pm 3.1)\,\Omega\,\mathrm{cm}^2$ is found for five samples. Hence, the measured resistance is surprisingly reproducible and very low, keeping in mind the low oxygen partial pressure, see also further comparison below. Unfortunately, this low p_{O_2} was not reached in the ex-situ setup. A direct comparison was thus performed at a somewhat higher oxygen partial pressure. Figure 5.4a displays the area specific electrode resistances in 0.25 mbar O_2 measured in-situ on seven different samples and ex-situ on ten samples. These resistances are again the initial values, i.e. measured immediately after deposition for in-situ measurements, or right after reaching a sta-

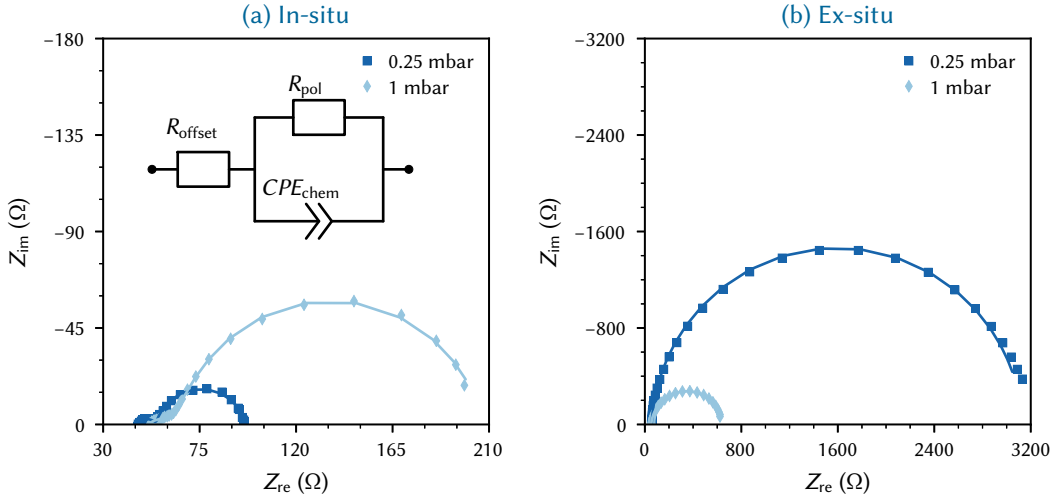

FIGURE 5.3: Impedance spectra of LSF thin films at 600 °C measured inside the PLD chamber ("in-situ") (a) and in an "ex-situ" impedance measurement setup (b). Markers indicate measured data points, lines are fits to an equivalent circuit shown in (a).

ble temperature in the case of ex-situ measurements. Most obvious is the almost two orders of magnitude lower polarization resistance found in-situ. For reasons yet unknown, these in-situ values scatter more than for 0.04 mbar O_2.

The polarization resistance inside the PLD chamber is also remarkably low in comparison to (ex-situ) polarization resistances reported in literature for LSF and other perovskites. For the sake of comparison we may take oxygen surface exchange coefficients of LSF obtained from conductivity relaxation experiments at low p_{O_2} on bulk[40] and thin film[53] samples to estimate the corresponding area specific resistances, and extrapolate them to our measurement temperature (600 °C) with the activation energies given in Refs. [40, 53]. Such a comparison shows a difference in exchange resistance at 0.25 mbar O_2 of two orders of magnitude between in-situ measured thin films and bulk samples, and a difference of even six orders of magnitude between our in situ measured thin films and Ref. [53], respectively. The measured in-situ resistance of LSF is also lower (by factors of 50 and 10, respectively) than some resistances found for $La_{0.6}Sr_{0.4}CoO_{3-\delta}$ (LSC) or $La_{0.6}Ba_{0.4}CoO_{3-\delta}$ (LBC) thin films, both of which are commonly considered much more active towards oxygen exchange than LSF.[6,10] Compared to surface exchange resistances obtained from impedance spectroscopy of LSF thin films at 600 °C in air, our

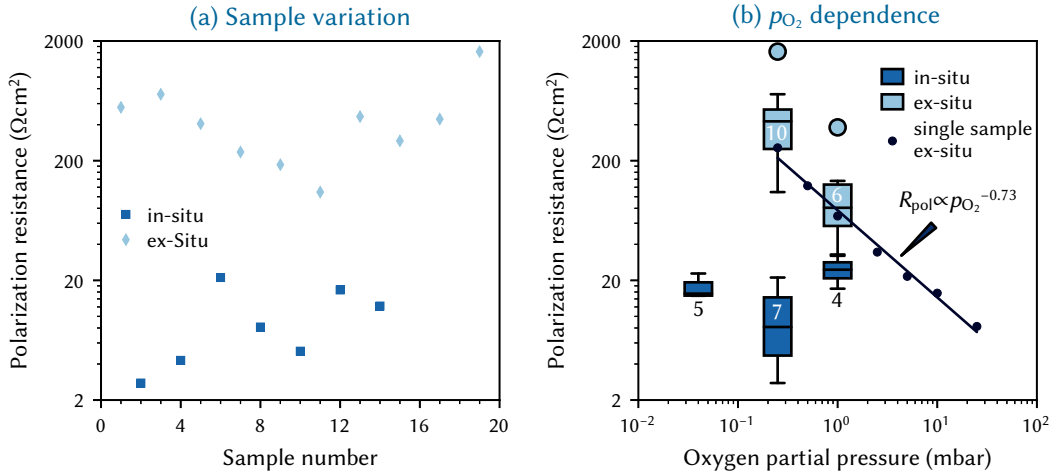

Figure 5.4: Area specific thin film electrode resistances at 600 °C determined by impedance spectroscopy. Measurements were done inside the deposition chamber immediately after thin film deposition ("in-situ") and in an ex-situ impedance spectroscopy setup. a) Polarization resistances of several different samples at 0.25 mbar O_2. b) Area specific resistances at 600 °C and in different p_{O_2}. The filled boxes represent the first and third quartiles, the median is represented by a solid line. Whiskers indicate maximum and minimum resistances measured, outliers are indicated by circles and the numbers in/below the boxes represent the number of investigated films. Markers indicate a p_{O_2} sweep measurement performed on a single sample, the line represents a fit of these resistances to a power law.

in-situ measured resistances are similar[13] or even much faster,[10] despite the much lower p_{O_2}. They are comparable to the performance of $Ba_{0.5}Sr_{0.5}Co_{0.8}Fe_{0.2}O_{3-\delta}$ (BSCF) thin films, one of the most active perovskites for oxygen exchange, in air.[10,43]

Under ex-situ conditions the polarization resistance of LSF shows a distinct decrease with increasing p_{O_2}. Figure 5.4b displays the p_{O_2} dependence for one individual film and the initial ex-situ resistances obtained for ten samples in 0.25 mbar and six samples in 1 mbar O_2. These p_{O_2} dependencies are also in accordance with those reported in literature for LSF and other perovskites.[6,40,53,69] However, when measured in-situ no clear p_{O_2} dependence is found for 5 samples in 0.04 mbar, seven samples in 0.25 mbar and four samples in 1 mbar O_2. Deviations between different oxygen partial pressures are within the uncertainty range due to variations between different samples. This change of the p_{O_2} dependence might indicate a switch of the oxygen incorporation mechanism upon transferring the sample to the ex-situ setup. Altogether, these results strongly indicate, that the electrochemical properties of pristine, as-deposited thin film MIEC electrodes are drastically different compared to the properties

investigated in common ex-situ measurements, not only in our laboratory but in general. This has severe implications for the accurate determination of the inherent oxygen exchange properties of oxides, but also with regard to mechanistic investigations. Moreover, without the possibility of such in-situ impedance measurements one would take the initial ex-situ value as the optimum without realizing that this already refers to a severely degraded surface. In the following we examine more closely this drastic performance change upon transfer of the samples from the deposition chamber to the ex-situ setup and investigate potential causes for this effect.

Time dependency Figure 5.5 shows the time dependency of the LSF polarization resistance degradation in-situ and ex-situ; the striking increase in resistance upon transfer from in-situ to ex-situ is clearly visible. Both in-situ and ex-situ the polarization resistance degrades with time at a moderate rate. However, between the in-situ and ex-situ measurements, i.e. upon transfer of the sample to the ex-situ setup, there is a drastic increase of the resistance at a much faster rate than the continuous degradation mentioned before. Please note, that the sample shown in figure figure 5.5 is the outlier in figure 5.4. In contrast to all other data points in figure 5.4 this ex-situ resistance was measured after the sample had already been investigated in the PLD for 2 h which partly explains the higher resistance.

It is thus very plausible to assume that two distinct degradation mechanisms with different characteristic time scales are at work here. Upon sample transfer back to the in-situ setup in the PLD chamber a decrease in polarization resistance could be observed. However, the initial low resistances were not reached, i.e the fast degradation is partially but not completely reversible on this time scale. Resistance degradation of LSF and related perovskites on the time scale of hours and days is often linked to Sr segregation to the surface.[4,5,7,22,54,85] This is also consistent with our XPS measurements (see below), where we find an increase of surface Sr with time. We thus suggest that the slower, continuous degradation observed both in-situ and ex-situ is caused by Sr segregating to the LSF surface. The much faster, large resistance increase upon transfer from in-situ to ex-situ setups, however, needs further consideration and several potential causes were investigated.

Potential degradation sources The effects of different potential degradation sources on the LSF polarization resistance are shown in figure 5.6. All experiments are performed in the pulsed laser deposition chamber, i.e. in the in-situ setup and resistances refer to 600 °C and 0.04 mbar O_2 (deposition conditions), except the humidity test which was conducted in 0.25 mbar O_2. For each experiment the resistance before and after exposure to a potential degradation source is shown, measured both initially and after 2 h, respectively. One can clearly see an increase of the

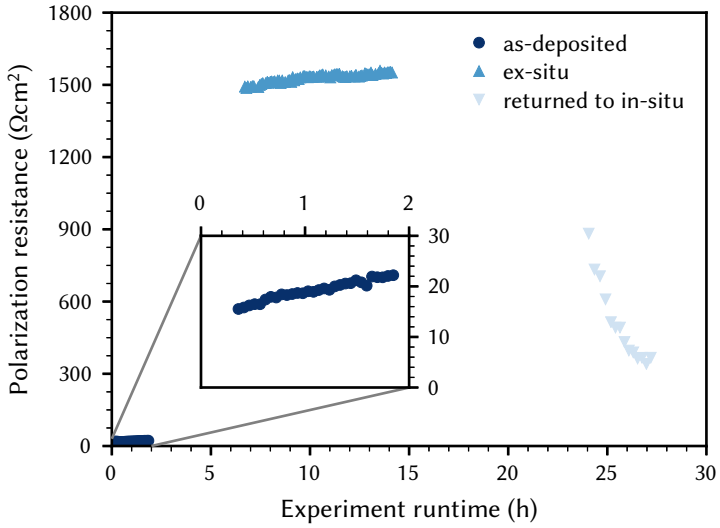

FIGURE 5.5: Time dependence of the polarization resistance of an LSF thin film at 600 °C and 0.25 mbar O_2. Measurements were done inside the PLD chamber after deposition and in an ex-situ setup. After the ex-situ measurement the sample was transferred back into the PLD chamber and measured again. The inset shows a magnification of the first in-situ measurement phase.

polarization resistance with time before, during and after the exposure period. This increase is, however, within the range expected from extrapolating the resistance degradation of the as deposited samples. More importantly, it is much less than the drastic difference in resistance between in-situ and ex-situ setup, and in some cases the exposure even slightly slows down the resistance degradation. Therefore, the discrepancy between in-situ and ex-situ measurements can not be explained by a surface modification of the as-deposited films through exposure to ambient air, high p_{O_2}, temperature cycles, humidity or a combination thereof. These measurements also reveal that highly active LSF surfaces not only exist for pristine films under deposition conditions but can sustain several thermal and chemical treatments, except transfer into the ex-situ setup.

Additionally, silicon contamination from the ex-situ setup (fused silica) was considered as a degradation source, since silicon is known to be a potent catalyst poison for mixed conducting oxygen electrodes.[21,86,87] To investigate the influence of the material used in the ex-situ sample holder two ex-situ measurement setups (see figure 5.2b) were fabricated that differ only by the tubes and spacers made either of fused silica or alumina. Both ex-situ setups led to drastically higher polarization resistances compared to in-situ measurements, and differences

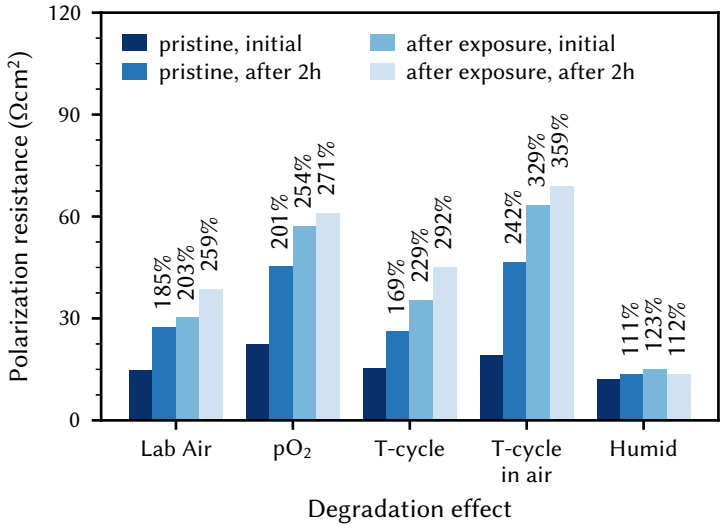

FIGURE 5.6: Polarization resistance of freshly deposited LSF thin film electrodes at 600 °C measured inside the PLD chamber before and after exposure to different potentially degrading conditions. Sample "Humid" was measured in 0.25 mbar O_2, all other samples were measured at the deposition pressure of 0.04 mbar O_2. The values above the bars indicate the resistance relative to the initial (pristine) resistance.

between samples measured in either of them were within the sample variance. Moreover, XPS measurements showed absence of Si signals on all samples. Silicon poisoning from the ex-situ setup can thus also be ruled out as fast degradation source.

5.3.2 Surface composition characterization

The surface composition of LSF thin films was determined by XPS. The Sr region of the spectra was examined more closely (see figure 5.7a) as Sr is known to play a critical role in the resistance degradation of perovskites. In accordance with literature, two different species (surface and bulk) can be identified in the Sr-3d binding energy range.[15,54] An increase of surface Sr was found on samples with thermal history (at least 24 h at 600 °C in the ex-situ setup) compared to the as-deposited films, indicating a segregation of Sr to the LSF surface during annealing, see figure 5.8, bottom. Similar Sr segregation is known for related perovskites and is often linked to resistance degradation of perovskite electrodes.[4,5,54] Additional annealing of the samples in the PLD chamber for four hours after the ex-situ measurement leads to a slight increase in the total Sr signal, but not in the fraction of surface to bulk Sr. The polarization resistance became even lower in the in-situ setup. Hence, this Sr segregation can only explain the standard slow degradation but not the huge resistance increase from in-situ to ex-situ setups.

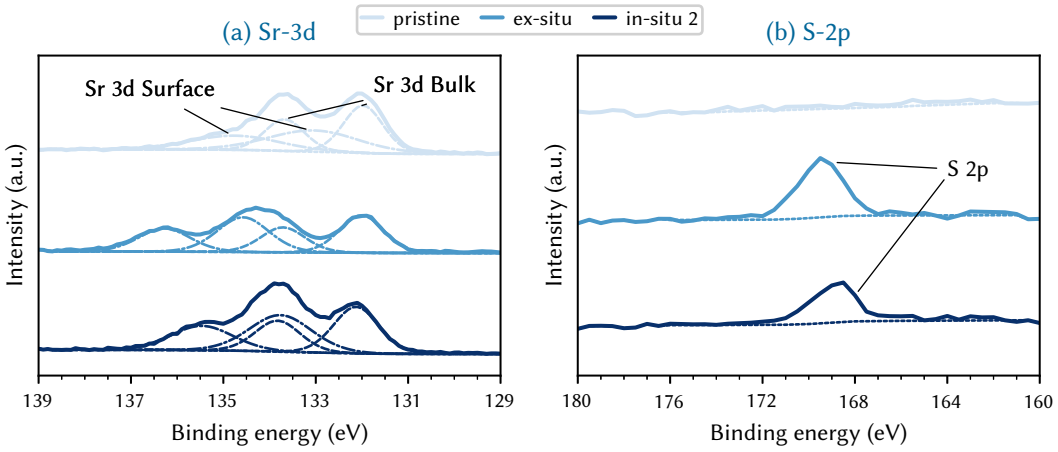

FIGURE 5.7: Sr-3d (a) and S-2p (b) regions of X-ray photoelectron spectra of LSF thin films with different histories. The "ex-situ" film was exposed to ex-situ measurement conditions for 24 h (in 0.25 mbar O_2). "in-situ 2" indicates the same sample after another 4 h in the PLD setup at 0.04 mbar O_2 and 600 °C.

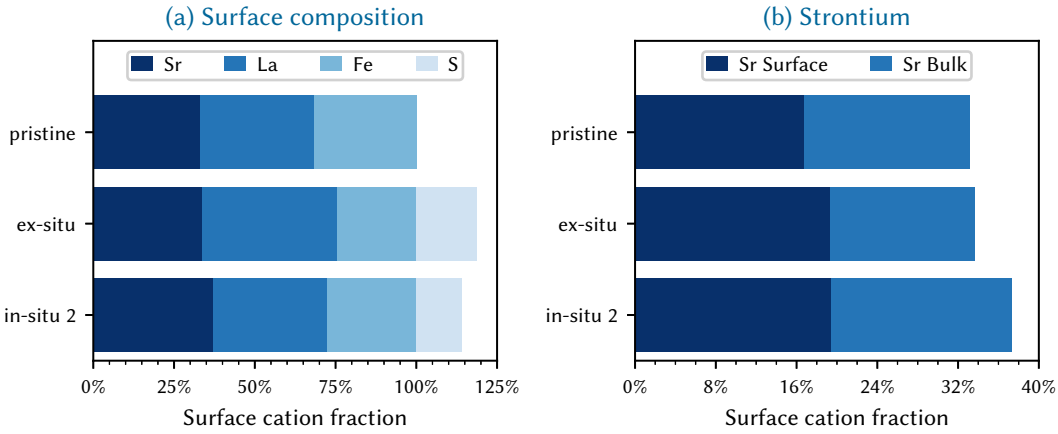

FIGURE 5.8: (a) Surface compositions determined by XPS, normalized to the sum of surface cations (Sr, La, Fe). Ex-situ means after 24 h at 600 °C in the ex-situ setup, in-situ 2 means after additional 4 h at 600 °C inside the PLD chamber. (b) Ratio of Sr surface and bulk species.

However, on samples exposed to the ex-situ setup, considerable amounts of sulphur were found, see figure 5.7b, and the binding energy of the S-2p peak corresponds to an oxidation state of S^{VI}, suggesting SO_4^{2-} ions.[88] Samples that were transferred back to PLD chamber and annealed there showed a reduced amount of sulphur. Accordingly, the presence and amount of sulphur on the surface strongly correlate with the electrochemical measurements. No sulphur

is found on the as-deposited samples and correspondingly these exhibit very low polarization resistances. Samples measured in the ex-situ setup show a large amount of sulphur on the surface and correspondingly, their polarization resistance is drastically increased. Upon transferring back to the PLD chamber and annealing there, both the sulphur content on the surface and the polarization resistance decrease. Besides sulphur, no other surface contaminants (e.g. chromium or silicon) could be detected by XPS.

5.3.3 Proposed degradation mechanism

Based on the electrochemical and surface composition analysis of LSF thin film electrodes in-situ and ex-situ, we propose that also chemically two degradation mechanisms with different time constants are at work. First, there is a segregation of Sr to the surface, either as a SrO phase or simply as a SrO terminating layer on LSF. The Sr segregation causes the slower degradation observed both in-situ and ex-situ. This is a continuous process, possibly accelerated by high p_{O_2}, and takes place on the time scale of hours and days at 600 °C. Second, there is a much faster degradation caused by the rapid formation of a sulfate (most likely $SrSO_4$) at the surface under ex-situ conditions. The latter is partially reversible by transferring the sample back to the PLD chamber and annealing there. Sulphur poisoning of perovskite oxide electrodes or catalysts is also reported in literature.[1,55,56,89] However, such poisoning experiments are often conducted by enriching the gas phase with appreciable amounts of a sulphur source (often SO_2, 1 to 100 ppm), whereas in our nominally sulphur free ex-situ setup high purity gases (99.999 %) are used and great care is taken to ensure a high purity measurement setup. This indicates, that even minute traces of sulphur in the measurement atmosphere can lead to considerable formation of sulphur on the MIEC surface, leading to drastically increased polarization resistances.

It is also worth again emphasizing that the sulphur poisoned electrodes of our study still exhibit polarization resistances that are among the most active LSF films reported so far. Hence, we are confident that we do not face a specific problem of our laboratory, but a rather common effect and thus a general problem (see polarization resistances above). Without sulphur poisoning (achieved in-situ) electrodes can exhibit extremely low polarization resistances. It is yet unclear whether the source of the sulphur traces are the gases or the measurement setup itself. If the high purity gas is responsible, the absence of the sulphur related degradation in the PLD chamber (in-situ) has to be due to a "getter" effect of the chamber. Alternatively, one may speculate about an unknown sulphur releasing part in the ex-situ setup as sulphur source. Great experimental efforts seem to be required to ensure that a pristine MIEC surface is probed and inherent material properties are observed. Moreover, also mechanistic conclusions seem to be affected since different p_{O_2} dependencies are found with and without sulphur poisoning.

5.4 Conclusion

The polarization resistance of LSF thin film electrodes was investigated by electrochemical impedance spectroscopy, both in-situ inside the PLD chamber immediately after deposition and ex-situ in a conventional measurement setup. These measurements revealed exceptionally low polarization resistances of the pristine, in-situ measured films, not only compared to our ex-situ data but also compared to literature. Moreover, a different p_{O_2} dependence of the polarization resistance was found under in-situ conditions, with very little p_{O_2} dependence, suggesting that the oxygen exchange reaction mechanism is different on as-deposited films compared to ex-situ measured samples.

Time dependent degradation measurements revealed two distinct degradation phenomena with different timescales. A continuous slow degradation was observed both in-situ and ex-situ. This continuous degradation correlates with an enrichment of Sr on the surface as determined by XPS and is most likely caused by Sr segregation. Additionally, a fast degradation occurred upon transfer to the ex-situ setup. Several potential sources of this second phenomenon, such as exposure to high p_{O_2}, humidity or ambient air, could be excluded as potential reasons. However, XPS studies revealed the formation of sulfates under ex-situ conditions, despite all measures to avoid sulphur contamination sources. Hence, the fast degradation upon transfer to the ex-situ setup seems to be linked to traces of sulphur contamination and might also be the reason behind increased (ex-situ) polarization resistances of many other studies in literature.

6 Conclusions

$La_{0.6}Sr_{0.4}FeO_{3-\delta}$ (LSF) thin films were prepared by pulsed laser deposition (PLD) on yttria-stabilized zirconia (YSZ) single crystals and characterized by bias dependent impedance spectroscopy and DC current-voltage measurements. From the results the defect related electrochemical electrode properties could be deduced and understood. In this framework, also a model was developed for analyzing and understanding defect related electrochemical properties of mixed conducting electrodes. Thus, the basis was created for detailed mechanistic interpretations of electrode reactions in solid state electrochemsitry. More specific, the following conclusions could be drawn.

Measurements of the chemical capacitance (C_{chem}) at varying DC voltage and oxygen partial (p_{O_2}) pressure revealed many details of the thin film defect chemistry. Analysis of the voltage and partial pressure dependence of C_{chem} showed that the chemical capacitance and thus thin film defect concentrations depend solely on the resulting oxygen chemical potential (μ_{O_2}), be it driven by p_{O_2} or an applied voltage. Variation of LSF film thickness revealed an area specific capacitive contribution, which can be attributed to the LSF|YSZ interface, which is especially prominent under reducing conditions. After subtracting this interfacial capacitance, a defect model for LSF could be used to deduce thermodynamic properties (i.e. enthalpies and entropies) of the defect chemical equilibria in LSF thin films. These measurements demonstrate that voltage and partial pressure dependent chemical capacitance measurements are a powerful tool for investigating thin film defect chemistry, especially with regards to minority defect concentrations. Comparison between predicted thermogravimetry and chemical capacitance curves also show that a much smaller span of oxygen chemical potential is required to gain the desired thermodynamic quantities. This is advantageous in terms of experimental ease, and might be relevant for materials with limited stability regimes.

The kinetics of the oxygen exchange reaction on LSF thin films was investigated by DC current voltage measurements at different oxygen partial pressures. A novel and broadly applicable method was developed to analyze such p_{O_2} dependent current voltage curves. This allowed separating observed p_{O_2} and electrode overpotential (η) dependencies into effects of oxygen adsorbates and thin film defect concentrations. By applying an overpotential that exactly counterbalances p_{O_2} induced changes in μ_{O_2}, the current was measured as a function of

p_{O_2} while keeping the oxygen chemical potential (and thus the defect concentrations) constant. The resulting p_{O_2} dependence represents the direct effect of p_{O_2} due to adsorbates and does not include its indirect effect via changing defect concentrations. In a similar manner, the overpotential was used to vary defect concentrations while keeping p_{O_2} constant. This method of analysing partial pressure dependent current voltage curves revealed novel mechanistic information on the oxygen reduction and evolution reactions on LSF. An apparent accelerating effect of p_{O_2} on the oxygen evolution rate was shown to be only an indirect effect via the impact of p_{O_2} on defect concentrations. This also indicated a strong involvement of electron holes in the oxygen evolution. In the cathodic direction the oxygen partial pressure dependence suggested the involvement of molecular oxygen in the rate limiting step. The oxygen chemical potential dependence hinted at oxygen vacancies as relevant defects for oxygen incorporation.

Based on this, a general framework was derived for describing electrochemical reactions at mixed ionic electronic conductor (MIEC) surfaces. Two exemplary oxygen exchange reaction mechanisms and the known defect chemical data of LSF were used to simulate current voltage curves over a wide range of oxygen partial pressures. These curves exhibit a variety of different shapes such as exponential Tafel like relations as well as essentially flat current limited regimes. However, despite the similarity to curve shapes obtained from classic aqueous electrochemical models, the physical reasons for the specific curve shapes are different. Contrary to aqueous electrochemistry, exponential current voltage curves are not the result of shifting activation barriers or electronic energy levels, but rather are caused by the exponential relation between defect concentrations and overpotential. Likewise, current limited regimes are not due to transport limitations, but arise from regimes of μ_{O_2} independent defect concentrations. General expressions for the p_{O_2} and η dependencies of the current were derived and shown to depend on the specific mechanism but also on the relation between defect concentration and μ_{O_2}, i.e. the Brouwer diagram. Most notably, these calculations reveal, that a direct interpretation of observed dependencies according to established models may lead to false conclusions. Square root oxygen partial pressure dependencies for instance are commonly interpreted as evidence for atomic oxygen species in the rate limiting step. However, due to the effect of p_{O_2} on defect concentrations, also mechanisms featuring molecular oxygen species in the rate determining step may produce such square root dependences.

Finally, in-situ impedance spectroscopy inside the pulsed laser deposition chamber revealed the properties of freshly deposited LSF films and their degradation. Thin film electrodes exhibited strikingly low polarization resistances inside the PLD chamber compared to literature and values obtained from ex-situ measurements. Furthermore, almost p_{O_2} independent polarization resistances were found under in-situ conditions, suggesting that a different oxygen exchange mechanisms is present, compared to ex-situ conditions. The degradation behaviour

was investigated in-situ and ex-situ and revealed two degradation effects with very different timescales. Continuous slow degradation takes place in-situ and ex-situ and this is attributed to Sr segregation. However, upon transfer from in-situ to ex-situ a fast, drastic increase in polarization resistance was observed. Several potentially degrading conditions such as high p_{O_2} or humidity could be excluded. Surface chemistry analysis by X-ray photoelectron spectroscopy indicated formation of $SrSO_4$ on the LSF surface despite all experimental measures to ensure a high purity, sulphur free environment. The fast degradation upon transfer to the ex-situ setup is thus probably linked to traces of sulphur contamination and this might also be the reason behind increased (ex-situ) polarization resistances of many other studies in literature.

Bibliography

[1] E. Bucher, C. Gspan, F. Hofer, and W. Sitte, "Sulphur poisoning of the SOFC cathode material $La_{0.6}Sr_{0.4}CoO_{3-\delta}$", *Solid State Ionics*, vol. 238, pp. 15–23, May 2013.

[2] T. Kawada, J. Suzuki, M. Sase, *et al.*, "Determination of oxygen vacancy concentration in a thin film of $La_{0.6}Sr_{0.4}CoO_{3-\delta}$ by an electrochemical method", *J. Electrochem. Soc.*, vol. 149, no. 7, E252–E259, 2002. DOI: 10.1149/1.1479728.

[3] M. Kubicek, T. M. Huber, A. Welzl, *et al.*, "Electrochemical properties of $La_{0.6}Sr_{0.4}FeO_{3-\delta}$ thin films investigated by complementary impedance spectroscopy and isotope exchange depth profiling", *Solid State Ionics*, vol. 256, pp. 38–44, 2014. DOI: 10/f3spvq.

[4] G. M. Rupp, A. Limbeck, M. Kubicek, *et al.*, "Correlating surface cation composition and thin film microstructure with the electrochemical performance of lanthanum strontium cobaltite (LSC) electrodes", *J. Mater. Chem. A*, vol. 2, no. 19, pp. 7099–7108, 2014. DOI: 10.1039/c3ta15327d.

[5] G. M. Rupp, H. Téllez, J. Druce, *et al.*, "Surface chemistry of $La_{0.6}Sr_{0.4}CoO_{3-\delta}$ thin films and its impact on the oxygen surface exchange resistance", *J. Mater. Chem. A*, vol. 3, no. 45, pp. 22 759–22 769, 2015. DOI: 10.1039/C5TA05279C.

[6] G. M. Rupp, A. Schmid, A. Nenning, and J. Fleig, "The superior properties of $La_{0.6}Ba_{0.4}CoO_{3-\delta}$ thin film electrodes for oxygen exchange in comparison to $La_{0.6}Sr_{0.4}CoO_{3-\delta}$", *J. Electrochem. Soc.*, vol. 163, no. 6, F564–F573, 2016. DOI: 10.1149/2.1061606jes.

[7] G. M. Rupp, A. K. Opitz, A. Nenning, *et al.*, "Real-time impedance monitoring of oxygen reduction during surface modification of thin film cathodes", *Nat. Mater.*, vol. 16, p. 640, Mar. 2017.

[8] J. Mizusaki, M. Yoshihiro, S. Yamauchi, and K. Fueki, "Thermodynamic quantities and defect equilibrium in the perovskite-type oxide solid solution $La_{1-x}Sr_xFeO_{3-\delta}$", *J. Solid State Chem.*, vol. 67, no. 1, pp. 1–8, 1987. DOI: 10.1016/0022 – 4596(87)90331 – 8.

[9] J. Bahteeva, I. Leonidov, M. Patrakeev, *et al.*, "High-temperature ion transport in $La_{1-x}Sr_xFeO_{3-\delta}$", *J. Solid State Electrochem.*, vol. 8, no. 9, pp. 578–584, Aug. 2004. DOI: 10.1007/s10008 – 003 – 0486 – 5.

[10] F. S. Baumann, J. Fleig, G. Cristiani, *et al.*, "Quantitative comparison of mixed conducting SOFC cathode materials by means of thin film model electrodes", *J. Electrochem. Soc.*, vol. 154, no. 9, B931–B941, 2007. DOI: 10.1149/1.2752974.

[11] F. S. Baumann, J. Maier, and J. Fleig, "The polarization resistance of mixed conducting SOFC cathodes: A comparative study using thin film model electrodes", *Solid State Ionics*, vol. 179, no. 21-26, pp. 1198–1204, 2008. DOI: 10.1016/j.ssi.2008.02.059.

[12] E. V. Bongio, H. Black, F. C. Raszewski, *et al.*, "Microstructural and high-temperature electrical characterization of $La_{1-x}Sr_xFeO_{3-\delta}$", *Fuel Cells*, vol. 14, no. 3, pp. 193–198, 2005. DOI: 10.1007/s10832 – 005 – 0957 – 4.

[13] S. Kogler, A. Nenning, G. M. Rupp, *et al.*, "Comparison of electrochemical properties of $La_{0.6}Sr_{0.4}FeO_{3-\delta}$ thin film electrodes: Oxidizing vs. reducing conditions", *J. Electrochem. Soc.*, vol. 162, no. 3, F317–F326, 2015. DOI: 10.1149/2.0731503jes.

[14] M. Kuhn, S. Hashimoto, K. Sato, *et al.*, "Oxygen nonstoichiometry, thermo-chemical stability and lattice expansion of $La_{0.6}Sr_{0.4}FeO_{3-\delta}$", *Solid State Ionics*, vol. 195, no. 1, pp. 7–15, 2011. DOI: 10.1016/j.ssi.2011.05.013.

[15] A. Nenning, A. K. Opitz, C. Rameshan, *et al.*, "Ambient pressure XPS study of mixed conducting perovskite-type SOFC cathode and anode materials under well-defined electrochemical polarization", *J. Phys. Chem. C*, vol. 120, no. 3, pp. 1461–1471, 2016. DOI: 10.1021/acs.jpcc.5b08596.

[16] A. K. Opitz, A. Nenning, C. Rameshan, *et al.*, "Enhancing electrochemical water-splitting kinetics by polarization-driven formation of near-surface iron(0): An in situ XPS study on perovskite-type electrodes", *Angew. Chemie - Int. Ed.*, vol. 54, no. 9, pp. 2628–2632, 2015. DOI: 10.1002/anie.201409527.

[17] B. Steele, "Properties of $La_{0.6}Sr_{0.4}Co_{0.2}Fe_{0.8}O_{3-\delta}$ (LSCF) double layer cathodes on gadolinium-doped cerium oxide (CGO) electrolytes II. Role of oxygen exchange and diffusion", *Solid State Ionics*, vol. 106, no. 3-4, pp. 255–261, 1998. DOI: 10.1016/S0167 – 2738(97)00430 – X.

[18] F. S. Baumann, J. Fleig, M. Konuma, *et al.*, "Strong performance improvement of $La_{0.6}Sr_{0.4}Co_{0.8}Fe_{0.2}O_{3-\delta}$ SOFC cathodes by electrochemical activation", *J. Electrochem. Soc.*, vol. 152, no. 10, A2074–A2079, 2005. DOI: 10.1149/1.2034529.

[19] E. Bucher and W. Sitte, "Defect chemical modeling of (La,Sr)(Co,Fe)$O_{3-\delta}$", *J. Electroceramics*, vol. 13, no. 1-3, pp. 779–784, 2004. DOI: 10.1007/s10832 – 004 – 5192 – x.

[20] F. S. Baumann, J. Fleig, H. U. Habermeier, and J. Maier, "Impedance spectroscopic study on well-defined (La,Sr)(Co,Fe)$O_{3-\delta}$ model electrodes", *Solid State Ionics*, vol. 177, no. 11-12, pp. 1071–1081, 2006. DOI: 10.1016/j.ssi.2006.02.045.

[21] E. Bucher and W. Sitte, "Long-term stability of the oxygen exchange properties of (La,Sr)(Co,Fe)$O_{3-\delta}$ in dry and wet atmospheres", *Proceedings of the 17th International Conference on Solid State Ionics*, vol. 192, no. 1, pp. 480–482, 2011.

[22] E. Bucher, W. Sitte, F. Klauser, and E. Bertel, "Impact of humid atmospheres on oxygen exchange properties, surface-near elemental composition, and surface morphology of $La_{0.6}Sr_{0.4}CoO_{3-\delta}$", *Solid State Ionics*, vol. 208, pp. 43–51, Feb. 2012.

[23] J. Mirzababaei and S. Chuang, "$La_{0.6}Sr_{0.4}Co_{0.2}Fe_{0.8}O_{3-\delta}$ perovskite: A stable anode catalyst for direct methane solid oxide fuel cells", *Catalysts*, vol. 4, no. 2, pp. 146–161, 2014. DOI: 10.3390/catal4020146.

[24] F. S. Baumann, J. Fleig, H. U. Habermeier, and J. Maier, "$Ba_{0.5}Sr_{0.5}Co_{0.8}Fe_{0.2}O_{3-\delta}$ thin film microelectrodes investigated by impedance spectroscopy", *Solid State Ionics*, vol. 177, no. 35-36, pp. 3187–3191, 2006. DOI: 10.1016/j.ssi.2006.07.057.

[25] A. Yan, M. Cheng, Y. Dong, *et al.*, "Investigation of a $Ba_{0.5}Sr_{0.5}Co_{0.8}Fe_{0.2}O_{3-\delta}$ based cathode IT-SOFC I. The effect of CO_2 on the cell performance", *Appl. Catal. B Environ.*, vol. 66, no. 1-2, pp. 64–71, 2006. DOI: 10.1016/j.apcatb.2006.02.021.

[26] J. F. Vente, S. McIntosh, W. G. Haije, and H. J. M. Bouwmeester, "Properties and performance of $Ba_xSr_{1-x}Co_{0.8}Fe_{0.2}O_{3-\delta}$ materials for oxygen transport membranes", *J. Solid State Electrochem.*, vol. 10, no. 8, pp. 581–588, 2006. DOI: 10.1007/s10008 – 006 – 0130 – 2.

[27] S. Gangopadhayay, T. Inerbaev, A. E. Masunov, *et al.*, "Structural characterization combined with the first principles simulations of barium/strontium cobaltite/ferrite as promising material for solid oxide fuel cells cathodes and high-temperature oxygen permeation membranes", *ACS Appl. Mater. Interfaces*, vol. 1, no. 7, pp. 1512–1519, 2009. DOI: 10.1021/am900182p.

[28] S. Lee, Y. Lim, E. A. Lee, *et al.*, "$Ba_{0.5}Sr_{0.5}Co_{0.8}Fe_{0.2}O_{3-\delta}$ (BSCF) and $La_{0.6}Ba_{0.4}Co_{0.2}Fe_{0.8}O_{3-\delta}$ (LBCF) cathodes prepared by combined citrate-EDTA method for IT-SOFCs", *J. Power Sources*, vol. 157, no. 2, pp. 848–854, 2006. DOI: 10.1016/j.jpowsour.2005.12.028.

[29] C. Niedrig, S. Taufall, M. Burriel, *et al.*, "Thermal stability of the cubic phase in $Ba_{0.5}Sr_{0.5}Co_{0.8}Fe_{0.2}O_{3-\delta}$ (BSCF)", *Solid State Ionics*, vol. 197, no. 1, pp. 25–31, 2011. DOI: http://doi.org/b2skps.

[30] N. H. Perry, D. Pergolesi, K. Sasaki, *et al.*, "Influence of donor doping on cathode performance: (La,Sr)(Ti,Fe)O_3 - Case study", *ECS Transactions*, vol. 57, no. 1, pp. 1719–1723, Oct. 2013. DOI: 10.1149/05701.1719ecst.

[31] N. H. Perry, D. Pergolesi, S. R. Bishop, and H. L. Tuller, "Defect chemistry and surface oxygen exchange kinetics of La-doped Sr(Ti,Fe)$O_{3-\alpha}$ in oxygen-rich atmospheres", *Solid State Ionics*, vol. 273, pp. 18–24, 2015. DOI: https : //doi.org/10.1016/j.ssi.2014.09.013.

[32] A. Staykov, H. Tellez, J. Druce, *et al.*, "Electronic properties and surface reactivity of SrO-terminated $SrTiO_3$ and SrO-terminated iron-doped $SrTiO_3$", *Sci. Technol. Adv. Mater.*, vol. 19, no. 1, pp. 221–230, 2018, PMID: 29535797. DOI: 10.1080/14686996.2018.1440136.

[33] E. Konysheva and J. T. S. Irvine, "Thermochemical and structural stability of A- and B-site-substituted perovskites in hydrogen-containing atmosphere", *Chem. Mater.*, vol. 21, no. 8, pp. 1514–1523, 2009. DOI: 10.1021/cm802996p.

[34] J. Mizusaki, T. Sasamoto, W. R. Cannon, and H. K. Bowen, "Electronic conductivity, seebeck coefficient, and defect structure of $La_{1-x}Sr_xFeO_{3-\delta}$ (x=0.1, 0.25)", *J. Am. Ceram. Soc.*, vol. 66, no. 4, pp. 247–252, Apr. 1983. DOI: 10.1111/j.1151 – 2916.1983.tb15707.x.

[35] J. Mizusaki, M. Yoshihiro, S. Yamauchi, and K. Fueki, "Nonstoichiometry and defect structure of the perovskite-type oxides $La_{1-x}Sr_xFeO_{3-\delta}$", *J. Solid State Chem.*, vol. 58, no. 2, pp. 257–266, 1985. DOI: 10.1016/0022 – 4596(85)90243 – 9.

[36] M. V. Patrakeev, I. A. Leonidov, V. L. Kozhevnikov, and K. R. Poeppelmeier, "p-type electron transport in $La_{1-x}Sr_xFeO_{3-\delta}$ at high temperatures", *J. Solid State Chem.*, vol. 178, no. 3, pp. 921–927, 2005. DOI: 10.1016/j.jssc.2004.10.038.

[37] A. M. Ritzmann, A. B. Muñoz-García, M. Pavone, *et al.*, "Ab initio DFT+U analysis of oxygen vacancy formation and migration in $La_{1-x}Sr_xFeO_{3-\delta}$ (x = 0, 0.25, 0.50)", *Chem. Mater.*, vol. 25, no. 15, pp. 3011–3019, 2013. DOI: 10.1021/cm401052w.

[38] M. Søgaard, P. Vang Hendriksen, and M. Mogensen, "Oxygen nonstoichiometry and transport properties of strontium substituted lanthanum ferrite", *J. Solid State Chem.*, vol. 180, no. 4, pp. 1489–1503, 2007. DOI: 10.1016/j.jssc.2007.02.012.

[39] J. A. Kilner, R. A. De Souza, and I. C. Fullarton, "Surface exchange of oxygen in mixed conducting perovskite oxides", *Solid State Ionics*, vol. 86-88, no. 2, pp. 703–709, 1996. DOI: 10.1016/0167 – 2738(96)00153 – 1.

[40] J. E. ten Elshof, "Oxygen exchange and diffusion coefficients of strontium-doped lanthanum ferrites by electrical conductivity relaxation", *J. Electrochem. Soc.*, vol. 144, no. 3, pp. 1060–1067, 1997. DOI: 10.1149/1.1837531.

[41] J. Fleig, H. R. Kim, J. Jamnik, and J. Maier, "Oxygen reduction kinetics of lanthanum manganite (LSM) model cathodes: Partial pressure dependence and rate-limiting steps", *Fuel Cells*, vol. 8, no. 5, pp. 330–337, 2008. DOI: 10.1002/fuce.200800025.

[42] J. Yoo, A. Verma, S. Wang, and A. J. Jacobson, "Oxygen transport kinetics in $SrFeO_3$, $La_{0.5}Sr_{0.5}FeO_{3-\delta}$, and $La_{0.2}Sr_{0.8}Cr_{0.8}Fe_{0.2}O_{3-\delta}$ measured by electrical conductivity relaxation", *J. Electrochem. Soc.*, vol. 152, no. 3, A497–A505, 2005. DOI: 10.1149/1.1854617.

[43] L. Wang, R. Merkle, and J. Maier, "Surface kinetics and mechanism of oxygen incorporation into $Ba_{1-x}Sr_xCo_yFe_{1-y}O_{3-\delta}$ SOFC microelectrodes", *J. Electrochem. Soc.*, vol. 157, no. 12, B1802–B1808, 2010. DOI: 10.1149/1.3494224.

[44] J. Fleig, R. Merkle, J. Maier, *et al.*, "The p(O_2) dependence of oxygen surface coverage and exchange current density of mixed conducting oxide electrodes: Model considerations", *Phys. Chem. Chem. Phys.*, vol. 9, no. 21, p. 2713, 2007. DOI: 10.1039/b618765j.

[45] S. Adler, "Mechanism and kinetics of oxygen reduction on porous $La_{1-x}Sr_xCoO_{3-\delta}$ electrodes", *Solid State Ionics*, vol. 111, no. 1-2, pp. 125–134, 1998. DOI: 10.1016/S0167 – 2738(98)00179 – 9.

[46] S. B. Adler, X. Y. Chen, and J. R. Wilson, "Mechanisms and rate laws for oxygen exchange on mixed-conducting oxide surfaces", *J. Catal.*, vol. 245, no. 1, pp. 91–109, 2007. DOI: 10.1016/j.jcat.2006.09.019.

[47] O. Yamamoto, "Perovskite-type oxides as oxygen electrodes for high temperature oxide fuel cells", *Solid State Ionics*, vol. 22, no. 2-3, pp. 241–246, 1987. DOI: 10.1016/0167 – 2738(87)90039 – 7.

[48] T. Kawada, K. Masuda, and J. Suzuki, "Oxygen isotope exchange with a dense $La_{0.6}Sr_{0.4}CoO_{3-\delta}$ electrode on a $Ce_{0.9}Gd_{0.1}O_{1.9}$ electrolyte", *Solid State Ionics*, vol. 121, pp. 271–279, 1999.

[49] Z. Guan, D. Chen, and W. C. Chueh, "Analyzing the dependence of oxygen incorporation current density on overpotential and oxygen partial pressure in mixed conducting oxide electrodes", *Phys. Chem. Chem. Phys.*, vol. 19, no. 34, pp. 23 414–23 424, 2017. DOI: 10.1039/C7CP03654J.

[50] J. Fleig, "On the current-voltage characteristics of charge transfer reactions at mixed conducting electrodes on solid electrolytes", *Phys. Chem. Chem. Phys.*, vol. 7, no. 9, pp. 2027–2037, 2005. DOI: 10.1039/B501086A.

[51] L. Wang, R. Merkle, Y. A. Mastrikov, *et al.*, "Oxygen exchange kinetics on solid oxide fuel cell cathode materials - General trends and their mechanistic interpretation", *J. Mater. Res.*, vol. 27, no. 15, pp. 2000–2008, Jul. 2012. DOI: 10.1557/jmr.2012.186.

[52] Y. A. Mastrikov, R. Merkle, E. Heifets, *et al.*, "Pathways for oxygen incorporation in mixed conducting perovskites: A DFT-based mechanistic analysis for (La,Sr)$MnO_{3-\delta}$", *J. Phys. Chem. C*, vol. 114, no. 7, pp. 3017–3027, 2010. DOI: 10.1021/jp909401g.

[53] M. Mosleh, M. Søgaard, and P. V. Hendriksen, "Kinetics and mechanisms of oxygen surface exchange on $La_{0.6}Sr_{0.4}FeO_{3-\delta}$ thin films", *J. Electrochem. Soc.*, vol. 156, no. 4, B441, 2009. DOI: 10.1149/1.3062941.

[54] Z. Cai, M. Kubicek, J. Fleig, and B. Yildiz, "Chemical heterogeneities on $La_{0.6}Sr_{0.4}CoO_{3-\delta}$ thin films - Correlations to cathode surface activity and stability", *Chem. Mater.*, vol. 24, no. 6, pp. 1116–1127, 2012. DOI: 10.1021/cm203501u.

[55] I. Rossetti, O. Buchneva, C. Biffi, and R. Rizza, "Effect of sulphur poisoning on perovskite catalysts prepared by flame-pyrolysis", *Appl. Catal., B*, vol. 89, no. 3, pp. 383–390, 2009.

[56] F. Wang, K. Yamaji, D.-H. Cho, *et al.*, "Sulfur poisoning on $La_{0.6}Sr_{0.4}Co_{0.2}Fe_{0.8}O_3$ cathode for SOFCs", *J. Electrochem. Soc.*, vol. 158, B1391, Jan. 2011.

[57] A. Schmid, G. M. Rupp, and J. Fleig, "Voltage and partial pressure dependent defect chemistry in (La,Sr)$FeO_{3-\delta}$ thin films investigated by chemical capacitance measurements", *Phys. Chem. Chem. Phys.*, vol. 20, no. 17, pp. 12 016–12 026, 2018. DOI: 10.1039/c7cp07845e.

[58] J. Jamnik and J. Maier, "Generalised equivalent circuits for mass and charge transport: Chemical capacitance and its implications", *Phys. Chem. Chem. Phys.*, vol. 3, no. 9, pp. 1668–1678, 2001. DOI: 10.1039/b100180i.

[59] J. Jamnik, J. Maier, and S. Pejovnik, "A powerful electrical network model for the impedance of mixed conductors", *Electrochim. Acta*, vol. 44, no. 24, pp. 4139–4145, 1999. DOI: 10.1016/S0013 – 4686(99)00128 – 0.

[60] W. C. Chueh and S. M. Haile, "Electrochemical studies of capacitance in cerium oxide thin films and its relationship to anionic and electronic defect densities", *Phys. Chem. Chem. Phys.*, vol. 11, no. 37, pp. 8144–8148, 2009. DOI: 10.1039/b910903j.

[61] G. Zhou, P. R. Shah, T. Montini, *et al.*, "Oxidation enthalpies for reduction of ceria surfaces", *Surf. Sci.*, vol. 601, no. 12, pp. 2512–2519, 2007. DOI: 10.1016/j.susc.2007.04.238.

[62] W. C. Chueh and S. M. Haile, "A thermochemical study of ceria: Exploiting an old material for new modes of energy conversion and CO_2 mitigation", *Philos. Trans. R. Soc. A Math. Phys. Eng. Sci.*, vol. 368, no. 1923, pp. 3269–3294, 2010. DOI: 10.1098/rsta.2010.0114.

[63] W. C. Chueh, A. H. McDaniel, M. E. Grass, *et al.*, "Highly enhanced concentration and stability of reactive Ce^{3+} on doped CeO_2 surface revealed in operando", *Chem. Mater.*, vol. 24, no. 10, pp. 1876–1882, 2012. DOI: 10.1021/cm300574v.

[64] G. J. Brug, A. L. van den Eeden, M. Sluyters-Rehbach, and J. H. Sluyters, "The analysis of electrode impedances complicated by the presence of a constant phase element", *J. Electroanal. Chem.*, vol. 176, no. 1-2, pp. 275–295, 1984. DOI: 10.1016/S0022–0728(84)80324–1.

[65] J. Maier, "Electrochemical investigation methods of ionic transport properties in solids", *Solid State Phenom.*, vol. 39-40, pp. 35–60, 1994. DOI: 10.4028/www.scientific.net/SSP.39 – 40.35.

[66] J. Maier, "Mass transport in the presence of internal defect reactions-concept of conservative ensembles: III, Trapping effect of dopants on chemical diffusion", *J. Am. Ceram. Soc.*, vol. 76, no. 5, pp. 1223–1227, May 1993. DOI: 10.1111/j.1151 – 2916.1993.tb03745.x.

[67] R. Zohourian, R. Merkle, and J. Maier, "Bulk defect chemistry of PCFC cathode materials: Discussion of defect interactions", *ECS Trans.*, vol. 77, no. 10, pp. 133–138, 2017. DOI: 10.1149/07710.0133ecst.

[68] J. Mizusaki, Y. Mima, S. Yamauchi, *et al.*, "Nonstoichiometry of the Perovskite-type oxides $La_{1-x}Sr_xCoO_{3-\delta}$", *J. Solid State Chem.*, vol. 80, no. 1, pp. 102–111, 1989. DOI: 10.1016/0022 – 4596(89)90036 – 4.

[69] A. Schmid, G. M. Rupp, and J. Fleig, "How to get mechanistic information from partial pressure-dependent current–voltage measurements of oxygen exchange on mixed conducting electrodes", *Chem. Mater.*, vol. 30, no. 13, pp. 4242–4252, 2018. DOI: http : //doi.org/gdwq9m.

[70] R. Merkle and J. Maier, "Oxygen incorporation into Fe-doped $SrTiO_3$: Mechanistic interpretation of the surface reaction", *Phys. Chem. Chem. Phys.*, vol. 4, no. 17, pp. 4140–4148, 2002. DOI: 10.1039/b204032h.

[71] S. Miyoshi, A. Takeshita, S. Okada, and S. Yamaguchi, "Rate-determining elementary step of oxygen reduction reaction at (La,Sr)CoO_3-based cathode surface", *Solid State Ionics*, vol. 285, pp. 202–208, 2016. DOI: 10.1016/j.ssi.2015.08.015.

[72] J. Fleig, G. M. Rupp, A. Nenning, and A. Schmid, "Towards an improved understanding of electrochemical oxygen exchange reactions on mixed conducting oxides", *ECS Trans.*, vol. 77, no. 10, pp. 93–108, 2017.

[73] M. S. D. Read, M. Saiful Islam, G. W. Watson, *et al.*, "Defect chemistry and surface properties of $LaCoO_3$", *J. Mater. Chem.*, vol. 10, no. 10, pp. 2298–2305, 2000. DOI: 10.1039/b002168g.

[74] M. M. Kuklja, E. a. Kotomin, R. Merkle, *et al.*, "Combined theoretical and experimental analysis of processes determining cathode performance in solid oxide fuel cells.", *Phys. Chem. Chem. Phys.*, vol. 15, no. 15, pp. 5443–5471, 2013. DOI: 10.1039/c3cp44363a.

[75] A. Bard and L. Faulkner, *Electrochemical Methods: Fundamentals and Applications*. Wiley, 2000.

[76] H. Gerischer, D. Kolb, and J. Sass, "The study of solid surfaces by electrochemical methods", *Adv. Phys.*, vol. 27, no. 3, pp. 437–498, 1978. DOI: 10.1080/00018737800101424.

[77] J. Maier, *Physical Chemistry of Ionic Materials: Ions and Electrons in Solids*. Wiley, 2004.

[78] A. Schmid and J. Fleig, "The current-voltage characteristics and partial pressure dependence of defect controlled electrochemical reactions on mixed conducting oxides", *Journal of The Electrochemical Society*, vol. 166, no. 12, F831–F846, 2019. DOI: 10.1149/2.1031912jes.

[79] R. Zohourian, R. Merkle, G. Raimondi, and J. Maier, "Mixed-conducting perovskites as cathode materials for protonic ceramic fuel cells: Understanding the trends in proton uptake", *Adv. Funct. Mater.*, vol. 28, no. 35, p. 1 801 241, 2018. DOI: 10.1002/adfm.201801241.

[80] D. N. Mueller, M. L. Machala, H. Bluhm, and W. C. Chueh, "Redox activity of surface oxygen anions in oxygen-deficient perovskite oxides during electrochemical reactions", *Nat. Commun.*, vol. 6, p. 6097, Jan. 2015.

[81] C. Kreller, T. McDonald, S. Adler, *et al.*, "Origin of enhanced chemical capacitance in $La_{0.8}Sr_{0.2}CoO_3$ - thin film electrodes", *J. Electrochem. Soc.*, vol. 160, F931–F942, Jun. 2013.

[82] J. H. Scofield, "Theoretical photoionization cross sections from 1 to 1500 keV.", English, California Univ., Livermore. Lawrence Limvermore Lab., United States, Tech. Rep., 1973.

[83] A. K. Opitz and J. Fleig, "Investigation of O_2 reduction on Pt/YSZ by means of thin film microelectrodes: The geometry dependence of the electrode impedance", *Solid State Ionics*, vol. 181, no. 15, pp. 684–693, 2010. DOI: https : //doi.org/10.1016/j.ssi.2010.03.017.

[84] A. Nenning, A. K. Opitz, T. M. Huber, and J. Fleig, "A novel approach for analyzing electrochemical properties of mixed conducting solid oxide fuel cell anode materials by impedance spectroscopy", *Phys. Chem. Chem. Phys.*, vol. 16, no. 40, pp. 22 321–36, 2014. DOI: 10.1039/c4cp02467b.

[85] H. Wang, K. J. Yakal-Kremski, T. Yeh, *et al.*, "Mechanisms of performance degradation of (La,Sr)(Co,Fe)$O_{3-\delta}$ solid oxide fuel cell cathodes", *J. Electrochem. Soc.*, vol. 163, no. 6, pp. 581–585, 2016. DOI: 10.1149/2.0031607jes.

[86] E. J. Opila, N. S. Jacobson, D. L. Myers, and E. H. Copland, "Predicting oxide stability in high-temperature water vapor", *JOM*, vol. 58, no. 1, pp. 22–28, Jan. 2006.

[87] D. Schlehuber, E. Wessel, L. Singheiser, and T. Markus, "Long-term operation of a $La_{0.58}Sr_{0.4}Co_{0.2}Fe_{0.8}O_{3-\delta}$-membrane for oxygen separation", *J. Membr. Sci.*, vol. 351, no. 1, pp. 16–20, Apr. 2010.

[88] *Nist x-ray photoelectron spectroscopy database, nist standard reference database number 20, national institute of standards and technology*, (retrieved [13.06.2019]), 2012. DOI: 10.18434/T4T88K.

[89] F. Wang, K. Yamaji, D.-H. Cho, *et al.*, "Effect of strontium concentration on sulfur poisoning of LSCF cathodes", *Solid State Ionics*, vol. 225, pp. 157–160, Oct. 2012.

List of Figures

List of symbols and abbreviations

Main symbols

Symbol	Description
e	elementary charge
k	Boltzmann's constant
T	absolute temperature
η	overpotential
p_{O_2}	oxygen partial pressure
μ_{O_2}	oxygen chemical potential vs. oxygen at 1 bar
χ	surface potential
χ_0	equilibrium surface potential
$\Delta\chi$	change of surface potential under current
β	surface potential dependency factor
C_{chem}	chemical capacitance
n_{uc}	concentration of unit cells
j	current density
j^0	exchange current density
R	resistance
R_{pol}	polarization resistance
A	electrode area
f	active surface fraction
C	capacitance
d	film thickness
U_{DC}	DC voltage
I_{DC}	DC current
c	concentration
θ	surface coverage
ν	reaction order
k	rate constant
K	equilibrium constant

Defects and adsorbate species

Symbol	Description
$V_O^{\bullet\bullet}$	oxygen vacancy
$h^{\bullet}$	electron hole
e'	electron
$O_O^{\times}$	lattice oxygen
$Fe_{Fe}^{\times}$	lattice iron
$O_O^{\bullet}$	onefold positively charged oxygen
$O_O^{\bullet\bullet}$	twofold positively charged oxygen
$ad_{(a)}$	free adsorption site for atomic adsorbates
$O_{(ad)}$	neutral atomic adsorbate
$O^{-}{}_{(ad)}$	negatively charged atomic adsorbate
$ad_{(m)}$	free adsorption site for molecular adsorbates
$O_{2(ad)}$	neutral molecular adsorbate
$O_{2(ad)}^{-}$	negatively charged molecular adsorbate

Subscript

Index	Description
WE	regarding the working electrode
CE	regarding the counter electrode
RE	regarding the reference electrode
at	atmosphere
a	regarding the anodic direction
c	regarding the cathodic direction
eq	in equilibrium
D	of defects (generic)
p	of p_{O_2}
V	of oxygen vacancies $V_O^{\bullet\bullet}$
h	of electron holes $h^{\bullet}$
e	of electrons e'
Ox	of lattice oxygen $O_O^{\times}$
Fe	of lattice iron $Fe_{Fe}^{\times}$
Op	of onefold positively charged oxygen $O_O^{\bullet}$
Opp	of twofold positively charged oxygen $O_O^{\bullet\bullet}$
(ad)	adsorbed
at	atomic (adsorbate)
mo	molecular (adsorbate)

Abbreviation	Meaning
SOFC	Solid oxide fuel cell
SOEC	Solid oxide electrolysis cell
MIEC	Mixed ionic electronic conductor
LSM	$La_xSr_{1-x}MnO_{3-\delta}$
LSC	$La_xSr_{1-x}CoO_{3-\delta}$
LSF	$La_xSr_{1-x}FeO_{3-\delta}$
LSCF	$La_xSr_{1-x}Co_yFe_{1-y}O_{3-\delta}$
BSCF	$Ba_xSr_{1-x}Co_yFe_{1-y}O_{3-\delta}$
LSTF	$La_xSr_{1-x}Ti_yFe_{1-y}O_{3-\delta}$
CPH	Combined power and heating
APU	Auxiliary power unit
YSZ	Yttria-stabilized zirconia
DFT	Density functional theory
PLD	Pulsed laser deposition
rms	root mean squared
CPE	Constant phase element
WE	Working electrode
CE	Counter electrode
RE	Reference electrode
XPS	X-ray photoelectron spectroscopy
SIMS	Secondary ion mass spectrometry
LEIS	Low energy ion scattering
IPLD	In-situ pulsed laser deposition
UHV	Ultra high vacuum

Acknowledgements

Lastly, I would like to express my gratitude towards the following people for their valuable contributions to this thesis. First and foremost, to my supervisor Professor Jürgen Fleig for his guidance and support and his great enthusiasm for discussing new results or planning new experiments. To the FWF and the project "Solids4Fun" which provided funding. To Tobias Huber who conceived and built most of the measurement setups used in this work, and who always found time to share his knowledge and experience in engineering with me. To Andreas Nenning who conducted the XPS measurements and whose scientific input often proved invaluable. To my office colleague Harald Summerer who has always lent me his ear and whose opinion on typographic and stylistic matters I have grown to value highly. To all the other members of the research group who have created a very enjoyable, inspiring and productive working environment. To my friends an family who always supported me and especially to my parents who have ever encouraged and fostered my interest for science and technology.

Thank you.